Radiative characterization of heterogeneous media for solar thermochemical applications

A DISSERTATION

SUBMITTED TO THE FACULTY OF THE GRADUATE SCHOOL

OF THE UNIVERSITY OF MINNESOTA

BY

Krithiga Ganesan

IN PARTIAL FULFILLMENT OF THE REQUIREMENTS

FOR THE DEGREE OF

Doctor of Philosophy

ADVISOR: WOJCIECH LIPINSKI

January, 2013

Acknowledgements

The financial support for this work by the Initiative for Renewable Energy and the Environment (grant no. RL-0003-2011), National Science Foundation (grant no. EFRI-1038307) and Advanced Research Projects Agency – Energy is gratefully acknowledged.

I would like to thank my advisor, Wojciech Lipinski for numerous discussions and contributions during the course of this work. In particular, I would like to acknowledge his inputs during the development of the Monte Carlo ray-tracing technique. I would also like to thank the team that developed the Fortran libraries FSL, TSL and CALC. These libraries greatly simplified the development of the Monte Carlo ray-tracing simulations.

I would like to thank the following collaborators:

I would like to acknowledge contributions by visiting researcher, Leonid Dombrovsky from Joint Institute for High Temperatures, Moscow. Leonid's contributions of Modified Two Flux and Mie theory calculations enhanced the scope and content of this dissertation. I also would like to thank Leonid for many suggestions for our joint publications.

I would like to thank visiting researcher, Jaona Randrianalisoa at GRESPI, University of Reims, for contributing one-dimensional discrete ordinate method calculations,

which, although not used in the present dissertation, was used for comparison and validation of the results of the Monte Carlo ray-tracing calculations.

Haile research group at the California Institute of Technology: William Chueh, Yong Hao, Danien Scipio and Taesik Oh for fabricating the sintered ceria discs and thin film samples used in the study.

Stein research group at the Department of Chemistry, University of Minnesota: Stephen Rudisill and Nick Petkovich for fabricating the 3DOM ceria samples used in the study.

At the Department of Mechanical Engineering, University of Minnesota: Zheng Liang, for contributions to the UV-VIS-NIR bi-normal measurements, Jeff Stamp for contributions to the experimental setups for measurement of radiative properties at high temperature; Kyle Johnson for design and assistance with fabrication of the sample holder used for reflectance measurements; Tingting Quan for preparing the 3DOM sample that underwent thermochemical cycling used in the present study.

I am grateful to the technical staff at University of Minnesota's Characterization Facility, and Chris Frethem in particular, for assistance with the SEM images. Characterization Facility receives partial support from NSF through the MRSEC program. I would like to thank the Minnesota Supercomputing Institute for assistance with the computing tasks during the course of this research program.

Abstract

Transport radiative properties of ceria ceramics as a function of wavelength and morphology are presented. Experimental facilities for measuring transmitted and reflected radiant energy were developed. A Monte Carlo ray-tracing technique was developed to infer transport scattering coefficient and absorption coefficient from measured transmittance and reflectance. An experimental setup to measure normal-emittance of materials employed in solar thermochemical applications is also designed. This experimental setup can achieve temperatures on the order of 1500 K and facilitate maintaining an inert, oxidizing or reducing environment to control composition of materials.

Transmittance and reflectance of two types of morphologies were examined. Sintered ceria discs with pores and grains of size a few microns and a random grain and pore structure, and a three-dimensionally ordered macro-porous (3DOM) ceria with nano-structured features were considered. The 3DOM samples were also thermochemically cycled for 60 cycles consisting of high-temperature reduction and low-temperature oxidation. Two porosities were considered for the sintered ceria discs with porosity, p = 0.08 ("dense" samples), and p = 0.72 ("porous" samples) and porosities of the packed bed before and after themochemical cycling were 0.9 and 0.83 respectively. Morphological characterization was performed by Scanning Electron Microscopy (SEM), and porosity was verified by mass and volume measurements of the samples.

Sintered ceria discs had extremely high optical thickness, with low and uncertain values of directional-hemispherical transmittance, and bi-normal transmittance on the order of 0.001 %. The transport radiative properties did not show a strong wavelength dependence after a wavelength of 0.5 μm. The transport scattering coefficient was on

the order of 30 mm^{-1} for the porous ceramics and 15 mm^{-1} for the dense ceramics after a wavelength of 0.5 μm. The absorption coefficient was on the order of 0.005 mm^{-1} for the dense ceramics and 0.03 mm^{-1} for the porous ceramics in the spectral range of weak absorption. Experimental uncertainty resulted in only approximate determination of transport radiative properties, particularly for the dense ceramics.

For the 3DOM packed bed, measured transmittance was of higher accuracy leading to lower uncertainty in measurements and identification procedure. The transport scattering coefficient showed a stronger spectral dependence than that of the sintered ceramics especially after a wavelength of 0.5 μm. Thermochemical cycling resulted in changes in the 3DOM morphology due to sintering of walls of the 3DOM structure. The morphology of 3DOM ceria after thermochemical cycling resembled sintered structures and this change also impacted the predicted radiative properties. The transport scattering coefficient showed strong dependence on morphology, with a drastic increase by a factor of four for 3DOM packed bed after thermochemical cycling. The absorption coefficient was only dependent on porosity, and did not show any change after thermochemical cycling, because the porosity only decreased weakly as a result of thermochemical cycling.

Predicted radiative properties indicate that an approximation applicable in the limits of large optical thickness, such as the Rosseland approximation can be employed to model heat and mass transfer rates in the ceria-based redox thermochemical cycles. Approximate models for optically thick media can greatly reduce computational cost of determination of radiative heat flux in such combined heat transfer problems. Morphological features that promote effective absorption of solar radiation in the visible spectrum and confinement of infrared radiation in the reactor are suggested.

Contents

Acknowledgements **i**

Abstract **iii**

List of Tables **vi**

List of Figures **vii**

Nomenclature **xvi**

1 Introduction **1**

1.1 Motivation 1

1.2 Scope 5

1.3 Research objectives 7

2 Theoretical background **10**

2.1 Radiative transfer equation (RTE) in participating media 10

2.2 Theoretical Predictions of Optical and Radiative Properties 15

2.3 Experimental Methods 19

2.4 Inferring Radiative Properties from Experimental Data 22

2.5 Summary 26

3 Experimental techniques for radiative characterization at ambient temperature 27

3.1 Methodology 27

3.2 Bi-normal transmittance setup 29

3.3 Normal-hemispherical transmittance and reflectance 33

4 Optical and morphological characterization of ceria 36

4.1 Fabrication and morphological characterization 37

4.1.1 Sintered ceria discs 37

4.1.2 3DOM ceria powder 39

4.1.3 Ceria thin film by pulsed laser deposition 45

4.2 Optical characterization of ceria 45

4.2.1 Transmission spectrum of non-scattering ceria sample 46

4.2.2 Optical constants of ceria 49

4.3 Summary 51

5 Experimental characterization at ambient temperature 53

5.1 Bi-normal transmittance 54

5.1.1 Sintered ceria discs 54

5.1.2 3DOM ceria packed bed 56

5.2 Normal-hemispherical transmittance and reflectance 58

5.2.1 Sintered ceria discs 58

5.2.2 3DOM ceria packed bed 64

5.3 Summary of experimental results 69

6 Identification of spectral radiative properties of ceria morphologies 71

6.1 Methodology 71

6.2 Monte Carlo ray-tracing method 76
6.2.1 Background 76
6.2.2 MCRT for sintered ceria discs 77
6.2.3 MCRT for 3DOM packed bed 82
6.3 Approximate solutions 86
6.3.1 Modified two-flux approximation 86
6.3.2 Mie theory for sintered discs 87
6.4 Results 90
6.4.1 Sintered ceria discs 90
6.4.2 3DOM ceria packed bed 96
6.5 Implications for solar thermochemical reactor design 104
6.6 Summary 106

7 Towards high temperature radiative characterization 108
7.1 Physics of interaction of radiation at high temperatures with ceramic materials 109
7.2 Background and challenges 110
7.3 Design specifications 111
7.3.1 Heat sources 111
7.3.2 Collection optics 114
7.3.3 Sample holder 115
7.4 Evaluation of design 118
7.5 Summary 121

8 Conclusions and outlook 123
8.1 Summary 123
8.2 Limitations and future work 125

References **128**

Appendix A. UV-VIS-NIR setup: component specification and calibration **141**

A.1 Specifications of UV-VIS-NIR setup for bi-normal transmittance measurements 141

A.1.1 Xe arc lamp 141

A.1.2 Monochromator 142

A.1.3 Optical filters 145

A.2 Calibration of the bi-normal transmittance setup 148

Appendix B. Approximate identification procedure from bi-normal transmittance **153**

Appendix C. Monte Carlo ray-tracing routine **158**

C.1 Sintered ceria discs 158

C.2 3DOM packed bed 162

Appendix D. Uncertainty analysis for transmittance and reflectance measurements **165**

List of Tables

4.1 Thickness of the cerium dioxide samples 39

6.1 Transmittance and reflectance obtained from MCRT simulations for various values of N_{rays} 85

7.1 Heat transfer losses (W) and power input (W) for sample heating listed for various sample temperatures 120

A.1 Grating specifications 147

A.2 Filter specifications 148

A.3 Filter and grating selection criteria 148

A.4 Spectrum of Hg-Ar lamp measured by Single and Subtractive-Double configuration compared to spectral irradiance (G_λ) data from Reader et al. (Reader et al., 1996). 150

List of Figures

1.1 Ceria-based solar thermochemical reactor: (a) components and (b) design stages . . . 3
2.1 Interaction of radiation with participating media . . . 11
2.2 Methods to determine radiative properties of participating media . . . 16
2.3 A schematic to illustrate bi-normal and normal-hemispherical measurements. . . . 21
2.4 An illustration of the direct and inverse problem. Adopted from (Bohren and Huffman, 1998). . . . 24
3.1 Experimental setup for measurement of binormal transmittance: subtractive-double configuration . . . 31
3.2 Experimental setup for measurement of bi-normal transmittance: single configuration for improved signal-to-noise characteristics . . . 32
3.3 Spectrum of the xenon arc lamp measured by the bi-normal transmittance setup . . . 33
3.4 Experimental setup for measurement of normal-hemispherical transmittance and reflectance . . . 35
4.1 SEM images of the dense sample taken at (a) Normal viewing angle and (b) 45 ° viewing angle. (c) Photograph of dense samples of various thicknesses . . . 40

4.2 SEM images of the porous sample taken at (a) Normal viewing angle and (b) 45 ° viewing angle. (c) Photograph of porous samples of various thicknesses 41
4.3 SEM images of the 3DOM ceria sample (a) before thermochemical cycling (b) after thermochemical cycling (c) photograph of the sample before (left, yellow) after cycling (right, white) 43
4.4 Schematic of the sample holder used for packing 3DOM ceria powder . 44
4.5 Transmittance of ceria thin film deposited on YSZ substrate, and blank YSZ substrate 46
4.6 Optical constants of polycrystalline ceria. Data taken from (Patsalas et al., 2002) 51
5.1 Bi-normal transmittance ($T_{\text{d-d}}$) of sintered ceria discs of porosity 0.08 and different sample thicknesses 56
5.2 Bi-normal transmittance ($T_{\text{d-d}}$) of sintered ceria discs of porosity 0.72 and different sample thicknesses 57
5.3 Bi-normal transmittance ($T_{\text{d-d}}$) of packed bed of 3DOM ceria of porosity 0.9 and different sample thicknesses 59
5.4 A comparison of bi-normal transmittance ($T_{\text{d-d}}$) of packed bed of 3DOM ceria and sintered ceria discs of thickness 0.57 mm 60
5.5 Normal hemispherical reflectance ($R_{\text{d-h}}$) of sintered ceria discs of different thicknesses and porosity 0.08 62
5.6 Normal hemispherical reflectance ($R_{\text{d-h}}$) of sintered ceria discs of different thicknesses and porosity 0.72 63
5.7 Normal hemispherical transmittance ($T_{\text{d-h}}$) of 3DOM ceria packed bed of different thicknesses and porosity 0.72 65

5.8 Normal hemispherical reflectance ($R_{\text{d-h}}$) of 3DOM ceria packed bed of different thicknesses and porosity 0.72 66
5.9 Normal hemispherical transmittance ($T_{\text{d-h}}$) and reflectance ($R_{\text{d-h}}$) of 3DOM ceria packed bed with and without thermochemical cycling of sample thickness 0.57 mm 67
5.10 Normal hemispherical reflectance ($R_{\text{d-h}}$) of 3DOM ceria packed bed with and without thermochemical cycling of sample thickness 0.57 mm, and sintered ceria discs of comparable thickness. 68
5.11 Normal hemispherical transmittance ($T_{\text{d-h}}$) and reflectance ($R_{\text{d-h}}$) of 3DOM ceria packed bed with and without thermochemical cycling 69
6.1 Domain for Monte Carlo ray-tracing of sintered ceria samples 79
6.2 Non-dimensional radiative intensity plotted as a function of solid angle for two different reflection conditions 80
6.3 Domain for Monte Carlo ray-tracing of 3DOM packed bed 83
6.4 Transport scattering albedo of sintered ceria discs obtained from directional-hemispherical transmittance, and eqs. (6.12a) – (6.12e). Calculations were performed by L. Dombrovsky (Dombrovsky et al., 2012). The ceramics were of porosity p_1 = 0.08 (dense) and p_2 = 0.72 (porous). . . 92
6.5 Bi-normal transmittance computed by MCRT simulations, T_{MC} for various values of β and fixed values of ω_{tr} for (a) porous samples (p = 0.72), $\omega_{\text{tr}} = 0.999$ and (b) dense samples (p = 0.08), $\omega_{\text{tr}} = 0.997$ plotted together with measured bi-normal transmittance, $T_{\text{d-d}}$. 93
6.6 Transport scattering coefficient of sintered ceria discs obtained by Mie theory and MCRT simulations. Mie calculations were performed by L. Dombrovsky (Dombrovsky et al., 2012). The ceramics were of porosity p_1 = 0.08 (dense) and p_2 = 0.72 (porous). 94

6.7 Absorption coefficient of sintered ceria discs obtained by Mie theory, and using eq. (6.13). Mie calculations were performed by L. Dombrovsky (Dombrovsky et al., 2012). The ceramics were of porosity p_1 = 0.08 (dense) and p_2 = 0.72 (porous). 95
6.8 Transport scattering coefficient of 3DOM ceria packed bed before thermochemical cycling obtained by MCRT simulations. 97
6.9 Absorption coefficient of 3DOM ceria packed bed before thermochemical cycling obtained by MCRT simulations. 98
6.10 Comparison of experimental data and results of Monte-Carlo ray-tracing simulations (a) directional-hemispherical transmittance and (b) directional-hemispherical reflectance. Experimental data is represented by lines, and Monte Carlo ray-tracing simulations at selected wavelengths are indicated by points. 100
6.11 Transport scattering coefficient of 3DOM packed bed before and after thermochemical cycling. Also shown is the transport scattering coefficient of sintered ceria ceramics of porosity p_1 = 0.08 (dense) and p_2 = 0.72 (porous) 101
6.12 Absorption coefficient of 3DOM packed bed before and after thermochemical cycling. Also shown is the absorption coefficient of sintered ceria ceramics of porosity p_1 = 0.08 (dense) and p_2 = 0.72 (porous) . . . 102
7.1 Schematic of experimental setup for measuring normal emittance of ceramic materials in the spectral range 0.7–10 μm and temperatures up to 1000 K. 112
7.2 A schematic of the sample holder. 117
7.3 Energy balance for the heated sample showing heat loss terms 119

A.1 Irradiance of xenon arc lamp at 0.5 m in the spectral range of 0.2–2.5 μm . . . 142
A.2 Principle of diffraction gratings . . . 143
A.3 Bandpass of a spectroscopic instrument for a given wavelength . . . 145
A.4 Efficiency of gratings used in UV-VIS-NIR setup (a) G1 (b) G2 (c) G3 (d) G4. Data obtained from Newport Corporation. . . . 146
A.5 Filter transmittance for optical filters used in the bi-normal transmittance setup. The filter numbers in the legend correspond to cut-on wavelengths and models listed in table A.2. Data obtained from Newport Corporation. . . . 149
A.6 Transmittance of metallic neutral density filters used in the bi-normal transmittance setup of optical density 1.0, 2.0 and 3.0. Solid curves indicate transmittance measured by silicon detector, and dashed curves indicate transmittance measured by germanium detector. . . . 152
C.1 Flowchart of Monte Carlo ray-tracing for the sintered ceria discs. . . . 160
C.2 Flowchart of Monte Carlo ray-tracing for the 3DOM packed bed. . . . 163
C.3 Flowchart of ray-tracing through a transparent window. . . . 164
D.1 Percentage statistical uncertainty in bi-normal transmittance measurement of the sintered dense ceramics. . . . 166
D.2 Percentage statistical uncertainty in bi-normal transmittance measurement of the sintered porous ceramics. . . . 167
D.3 Percentage statistical uncertainty in bi-normal transmittance measurement of the 3DOM packed bed. . . . 168
D.4 Percentage statistical uncertainty in normal-hemispherical transmittance measurement of the 3DOM ceria packed bed. . . . 169

D.5 Percentage statistical uncertainty in normal-hemispherical transmittance measurement of the 3DOM ceria packed bed. 170

Nomenclature

Alphabets

a	Particle or pore radius (μm)
A	Size-distribution parameter (μm^{-1}) or area (m^2)
A_1–A_6	Boundaries of MCRT computational domain
b	Monochromator bandpass (nm) or fraction of backscattered intensity
B	Size-distribution parameter
B_1–B_4	Fitting constants in eq. (B.9)
c	Specific heat (kJ kg^{-1} K^{-1})
d	Particle or pore diameter
D	Limit of resolution of a monochromator (μm) or Rosseland parameter
$\dot{E}_{\text{storage}}$	Rate of storage of energy (W)
f	Fraction of forward-scattered intensity or fitting function in eq. (B.9)
f_{v}	Particle or pores per unit volume (mm^{-3})
$f(x)$	Frequency function
F	Two-parameter gamma-distribution (μm^{-1})
$F(x)$	Cumulative distribution function
g	Anisotropic scattering parameter or fitting function in eq. (B.9)

$g(x)$	Probability density function
G	Irradiance (W m^{-2} μm^{-1})
h	Heat transfer coefficient (Wm^{-2} K $^{-1}$) or film thickness of ceria thin film(μm)
I_λ	Spectral radiative intensity (W m^{-2}μm^{-1} sr $^{-1}$)
I	Total radiative intensity (W m^{-2} sr $^{-1}$)
k	Index of absorption or thermal conductivity (Wm^{-1} K $^{-1}$)
L	Sample thickness (mm)
m	Diffraction order
$\dot{m}$	Mass flow rate (kg/s)
n	Index of refraction
N	Ray counter in MCRT simulations
$\hat{\mathbf{n}}$	Unit normal vector
p	Porosity
q	Heat flux (W m^{-2})
$\dot{Q}$	Heat transfer rate (W)
$\dot{Q}_{\text{cs}}$	Radiative power from concentrated solar radiation (W)
Q_{abs}	Absorption efficiency
$\dot{Q}_{\text{d}}^{0}$	Signal measured by the detector without the sample (V)
$\dot{Q}_{\text{d}}$	Signal measured by the detector with the sample (V)
Q_{sca}	Scattering efficiency
r	Position (m)
$\mathbf{r}$	Position vector (m)
$\hat{\mathbf{s}}$	Direction of a ray
R	Reflectance or Random number
s	Attenuation path length (mm)
	or monochromator reciprocal linear dispersion (nm/mm)

S	Radiative source function
$\hat{\mathbf{t}}_1, \hat{\mathbf{t}}_2$	Unit vectors
t	time (s)
T	Transmittance or temperature (K)
V	Volume (m^3)
$\dot{W}_{\text{in}}$	Laser power input for sample heating
w	Monochromator slit width
x	Diffraction size parameter or axial direction

Greek symbols

α	Incidence angle (rad)
β	Extinction coefficient (mm^{-1}) or diffraction angle
γ	Coefficient in boundary condition, eq. (6.12a)
Γ	Gamma distribution
δ	Coefficient of non-stoichiometry or phase difference or Dirac delta
ϵ	Emittance or Error
η_{th}	Thermal efficiency
θ	Polar angle (rad)
κ	Absorption coefficient (mm^{-1})
λ	Wavelength (μm)
μ	Directional cosine
ρ	Interface (Fresnel) reflectivity or density (kg m^{-3})
σ	Scattering coefficient (mm^{-1}) or standard deviation
τ	Optical thickness or interface transmissivity
	or period of oscillation in interference pattern

ϕ	Azimuthal angle
Φ	Scattering phase function
χ	Eigen value
ω	Scattering albedo
Ω	Solid angle (sr)

Subscripts

1	Externally irradiated boundary; referring to dense sintered sample
2	Non-irradiated boundary; referring to porous sintered sample
32	Sauter radius
abs	Absorbed or absorption
b	Blackbody
coll	Optical collection
cond	Conduction
conv	Convection
cs	Concentrated solar
cer	Ceria
d	Detector
d-d	Bi-normal
DD	Dirac-delta
d-h	Directional-hemispherical
HG	Henyey-Greenstein
i	Incident direction
in	Input or incident
int	Interface

m	Maximum
mean	Mean
med	Median
MC	Monte Carlo
ox	Oxidized state
out	Exiting the sample
p	Particle or pore
red	Reduced state
refl	Reflected
re-rad	Re-radiated
R	Reflectance or radiative
sca	Scattered or scattering
T	Transmittance
th	Thermal
trans	Transmitted
tr	Transport
w	Window or boundary
λ	Spectral quantity

Superscripts

0	Without the sample
’	Directional or dummy variable
”	Bi-directional
*	Dummy variable
$\cap$	Hemispherical

R	Rosseland-mean

Abbreviations

3DOM	Three-dimensionally ordered macroporous
EM	Electromagnteic theory
FCC	Face-centered cubic
FTIR	Fourier Transform Infrared
HHV	Higher heating value (kJ /kg)
MC	Monte Carlo
MCRT	Monte Carlo ray-tracing
OD	Optical density of neutral-density filters
PLD	Pulsed laser deposition
PMMA	Polymethyl methacrylate
RTE	Radiative transfer equation, eq. (2.1)
SEM	Scanning electron microscope
UV-VIS-NIR	Ultra-violet, visible and near-infrared
YSZ	Yttria stabilized zirconia

Chapter 1

Introduction

1.1 Motivation

Recent investigations on energy technology reveal that even at conservative estimates of solar to thermal energy (and consequently electric power) conversion efficiency, solar energy is capable of meeting a large fraction of energy demands world-wide. It has been suggested that with as little as 0.1% of land use and a 20 % efficiency of collection of solar energy, it is possible to meet the energy needs of the planet (Steinfeld, 2005). However, deployment of solar energy has historically been limited by the intermittent availability of solar energy, and inefficient high cost energy storage technologies to store the available solar energy and transport it to locations that do not receive much sunlight. The use of concentrated solar energy to produce fuels has been envisioned as a possible solution that might mitigate these problems and encourage tapping into an abundantly available renewable energy resource. Solar thermochemical reactors convert sunlight into chemically energetic synthesis gas, which can be used to generate

commercially available fuels such as gasoline, diesel, jet fuel or natural gas. This conversion process utilizes concentrated solar energy to achieve high temperatures in a reactor, which drives a cyclic chemical reaction. Water and carbon dioxide are converted to hydrogen and carbon monoxide in the cyclic chemical reaction, in the presence of a reacting metal oxide which also absorbs and contains concentrated solar energy in the reactor. Besides not requiring infrastructure improvement, this technology effectively recycles carbon dioxide from fuel emissions into synthetic fuel ("syngas", obtained from hydrogen and carbon monoxide) and addresses concerns regarding energy security and global warming. Solar thermochemical fuel production is also a viable alternative to direct water splitting, also known as thermolysis, to produce hydrogen since the latter reaction occurs at prohibitively high temperatures requiring a large concentration ratio of available solar energy on the earth's surface by optical systems capable of providing high concentration ratios such as parabolic dishes. Such high concentration ratios approach the limits of current optical solar energy collection systems due to reradiation losses. Besides, thermolysis has other disadvantages such as slow chemical reaction rates and the need to separate the products of the chemical reaction because they remain in the gaseous phase as opposed to metal oxide based chemical reaction, where the metal oxides retain their solid phase throughout the reaction, requiring only a purge gas to sweep hydrogen or carbon monoxide out of the reactor.

Figure 1.1 illustrates the working principle of a solar thermochemical reactor. Reacting metal oxide media simultaneously serve as solar absorbers and chemical reactants. Recently, porous cerium dioxide (ceria) ceramics have been suggested as a favorable material for such reacting media because of rapid chemical kinetics over other metal-metal oxide cycles such as the zinc-zinc oxide cycle (Chueh et al., 2010). Cerium is one of the seventeen rare-earth elements and is one of the most abundant elements in the earth's crust greater than copper (Min, 2008). Because of its abundance, cerium

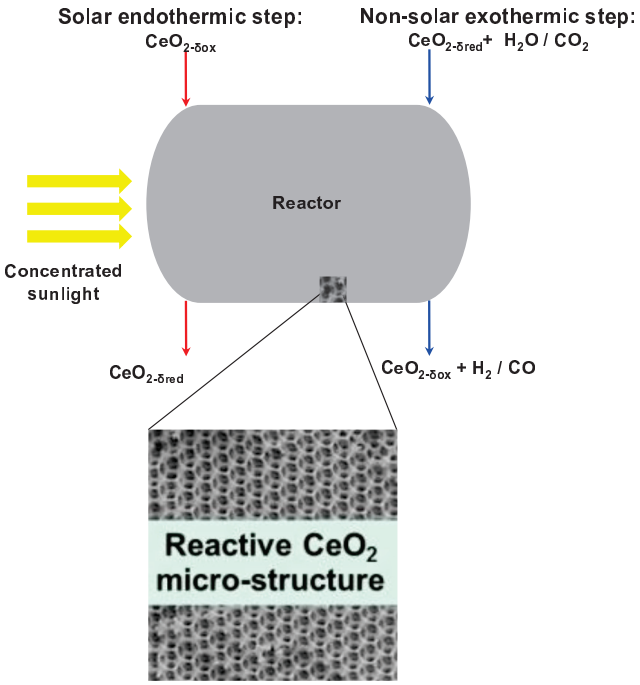

(a)

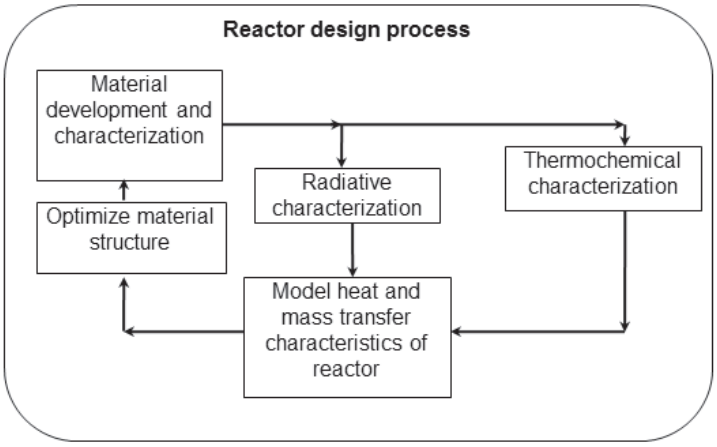

(b)

Figure 1.1: Ceria-based solar thermochemical reactor: (a) components and (b) design stages

oxide has been widely employed in many applications such as three-way catalysis for automotive applications, ceramics, as an electrolyte in fuel cells etc. One of the favorable properties of ceria is its redox capability. Ceria forms oxygen vacancies or defects in its lattice structure in response to changes in physical conditions such as temperature, oxygen partial pressure or doping with other ions. Many different morphologies of ceria have been developed for energy conversion applications, and a review of synthesis techniques and characteristics is available in (Sun et al., 2012).

A two-step partial redox thermochemical cycle with ceria as the reacting medium cycles carbon dioxide or water to produce carbon monoxide or hydrogen as follows (Chueh and Haile, 2009; Abanades and Flamant, 2006):

Solar, endothermic step:

$$\frac{1}{\Delta\delta}\mathrm{CeO}_{2-\delta_{\mathrm{ox}}} \rightarrow \frac{1}{\Delta\delta}\mathrm{CeO}_{2-\delta_{\mathrm{red}}} + \frac{1}{2}\mathrm{O}_2(\mathrm{g}) \tag{1.1}$$

Non-solar, exothermic step:

$$\frac{1}{\Delta\delta}\mathrm{CeO}_{2-\delta_{\mathrm{red}}} + \mathrm{H}_2\mathrm{O}(\mathrm{g}) \rightarrow \frac{1}{\Delta\delta}\mathrm{CeO}_{2-\delta_{\mathrm{ox}}} + \mathrm{H}_2(\mathrm{g}) \tag{1.2}$$

$$\frac{1}{\Delta\delta}\mathrm{CeO}_{2-\delta_{\mathrm{red}}} + \mathrm{CO}_2(\mathrm{g}) \rightarrow \frac{1}{\Delta\delta}\mathrm{CeO}_{2-\delta_{\mathrm{ox}}} + \mathrm{CO}(\mathrm{g}) \tag{1.3}$$

where δ_{red} and δ_{ox} are, respectively, the non-stoichiometry coefficients of the reduced and oxidized forms of cerium dioxide in the redox cycle, and $\Delta\delta = \delta_{\mathrm{red}} - \delta_{\mathrm{ox}}$. In the first, endothermic step, ceria in its oxidized state (typically CeO_2, but other non-stoichiometric compositions can also be used) undergoes reduction, to form ceria in its reduced state ($CeO_{2-\delta_{\mathrm{red}}}$). In the second, exothermic step, ceria in its reduced state recombines with oxygen from either CO_2 or water, to return to its oxidized state. Hydrogen and carbon monoxide are products of the net chemical reaction. The reaction temperatures for the endothermic and exothermic reactions above were reported to be

on the order of 1500 K and 1000 K respectively (Chueh and Haile, 2010), which are far below the melting point of ceria (2800 K).

Thermal efficiency for the production of components of the synthesis gas in the thermochemical cycle is defined as:

$$\eta_{\text{th}} = \frac{\dot{m}\text{HHV}}{\dot{Q}_{\text{cs}}} \tag{1.4}$$

Here, $\dot{m}$ is the mass flow rate of H_2 or CO, HHV is the higher heating value of H_2 or CO, and $\dot{Q}_{\text{cs}}$ is the radiative power from concentrated solar radiation. Thermal efficiency of up to 10% is obtainable from the two-step partial redox ceria cycle if the porous ceria structures have a suitable morphology with desirable thermal transport characteristics, especially if heat recuperation is employed to heat ceria and sweep gas (Lapp et al., 2011). Here, morphology of the ceria structures refers to quantities such as porosity, pore spacing, arrangement pores and other structural and geometrical features. In order to study the effect of morphology of ceria structures on the thermal transport phenomena in the solar thermochemical reactor, heat and mass transfer rates are modeled. The model typically solves equations that govern transport phenomena in porous media, namely mass, momentum and energy conservation equations, as well chemical reaction equations for species transport. Radiative properties of ceria are crucial at this modeling step, since they appear in heat transfer equations that are solved in the model. Knowledge of radiative properties also guides material scientists in developing suitable morphological structures that are capable of achieving optimal solar absorption in the visible solar spectrum, and effective confinement of re-emitted radiation in the infrared in order to reach the temperatures required for driving the chemical reaction.

1.2 Scope

The present work is as a result of on-going research projects funded by the National Science Foundation (NSF), Initiative for Renewable Energy and the Environment (IREE), and Advanced Research Projects - Energy (ARPA-E) to develop thermochemical reactors for solar-driven fuel production using novel ceria structures. The scope of the present work is to obtain radiative properties of these ceria structures to aid solar thermochemical reactor design and thermal transport modeling. Radiative properties of reacting (participating) media such as cerium dioxide are functions of morphology of the medium, chemical composition, radiation wavelength and temperature. The characteristics of the reacting medium, which can be tailored by modifying medium morphology and the medium composition, should allow for (i) efficient absorption of incident concentrated solar radiation, (ii) rapid heat transfer between the absorption and reaction sites, (iii) confinement of the emitted thermal radiation in the close vicinity of the reaction site, (iv) minimum heat losses from the reacting medium by conduction and convection, and (v) rapid chemical reaction. High specific surface area and porosity as well as varying levels of semi-transparency in the visible and infrared spectral ranges are a desired combination of morphological and optical characteristics to satisfy the above criteria for optimizing reacting media for solar thermochemical applications. Radiative characterization of reacting media is crucial to transport modeling and optiminzing the reacting media for solar thermochemical applications.

Collaborators on the project include material development and characterization performed by the Department of Materials Science at the California Institute of Technology, and Department of Chemistry at the University of Minnesota. As of December 2012, thermal transport modeling is being performed by researchers at the Department

of Mechanical Engineering, University of Minnesota. Thermochemical characterization of the ceria structures were conducted both by Department of Materials Science, California Institute of Technology and Department of Mechanical Engineering at the University of Minnesota. Novel ceria structures were developed as a part of this project by the materials development team at the Department of Materials Science, California Institute of Technology and Department of Chemistry at the University of Minnesota. A number of studies on ceria for thermochemical cycling have since then appeared in the literature on areas such as material development (Petkovich et al., 2011), thermochemical characterization (Chueh et al., 2010; Venstrom et al., 2012), and thermal transport modeling (Lapp et al., 2011).

Ceria samples used in the present study were provided by Prof. Sossina Haile's research group at the California Institute of Technology, and Prof. Andreas Stein's research group at the Department of Chemistry, University of Minnesota. Morphological, optical and radiative characterization were performed by the author of the present work. Visiting researcher Leonid Dombrovsky, Joint Institute of High Temperatures, Moscow provided inputs that enabled the identification of radiative properties of the sintered ceria discs, described in section 6.3. The present work also includes inputs from students at the University of Minnesota, Tingting Quan who performed thermochemical cycling of the samples used in the present study, Zheng Liang, who assisted in development of the subtractive double setup shown in Fig. 3.1, and Jeff Stamp who developed collection optics described in section 7.3.2.

1.3 Research objectives

Approximately 90 % of the emissive power of solar radiation is contained in the spectral range 0.3–2 μm and 5 % in the spectral range 2–10 μm. Emission spectra of

blackbodies indicates that for a blackbody at a temperature of 1800 K, approximately 40 % of the spectral emissive power is between wavelengths of 0.3–2 μm and 57 % in the spectral range 2–10 μm. For a blackbody at 1000 K, nearly 84 % of the spectral emissive power is in the wavelength range is in the spectral range 2–10 μm and only 6 % in the wavelength range 0.3–2 μm. From the preceding analysis, it becomes evident that from the perspective of characterizing the absorption of incident solar radiation, the UV-VIS-NIR spectrum between 0.3–2 μm is significant. This holds well for characterizing re-emission from the reacting media (such as porous ceria structures) at high temperatures of 1800 K also. More thorough radiative characterization of re-emission must include the longer wave portion of the spectrum, between 2–10 μm. Encompassing a wide spectral range of radiative characterization is achieved by radiative transfer measurements of absorbed, emitted, transmitted or reflected radiant energy over a wide spectral range, which in turn requires development of experimental facilities for the two different spectral ranges, i.e. between 0.3–2 μm and 2–10 μm. This is because materials and optical elements such as spectrometers, radiation detectors and sources of radiation that can be used for measurement of radiative transfer quantities in one spectral range are typically not sensitive in another spectral range.

The present study focuses on investigation of absorption and scattering characteristics of ceria in the most significant part of the spectrum for solar thermochemical reactions, between 0.3–2 μm. Radiative properties are also a function of temperature, and traditional approaches involve measuring emittance of a material as a function of temperature in order to infer its radiative characteristics at high temperatures. The present work also involves the development of a methodology to measure normal-emittance of ceria as a function of wavelength and temperature. Emittance in the spectral range 0.7–10 μm and temperatures up to 1000 K can be measured using this facility to infer radiative properties of materials at high temperatures.

The research goals of the present work are:

1) Development of methods for performing spectrally resolved radiative characterization of heterogeneous media for solar thermochemical applications at ambient temperature.

The first objective is achieved by developing experimental facilities that are capable of measuring transmitted and reflected radiant energy from a material in the spectral range 0.3–2 μm and at ambient temperature. A numerical procedure involving approximate models in combination with Monte Carlo ray-tracing techniques is used to infer radiative properties in the spectral range of interest. Chapter 2 presents a review of some experimental and numerical techniques frequently employed to infer radiative properties of participating semitransparent materials. Chapter 3 is a description of two experimental setups developed as a part of the present work.

2) Radiative characterization of ceria as a function of wavelength and morphology at ambient temperature.

Radiative properties of ceria with different morphological features such as pore-size, pore arrangement and geometry are determined. Chapter 4 presents descriptions, fabrication, morphological and optical characterization of different types of ceria samples used in the present study. Chapter 5 presents results of the experiments conducted at ambient temperature for different samples, together with qualitative conclusions that can be inferred from the experimental data. Chapter 6 describes the Monte Carlo ray-tracing method along with the radiative properties predicted by approximate methods and theoretical predictions.

3) Towards development of methods for radiative characterization at high temperature.

An experimental setup that facilitates radiative characterization at elevated temperatures is designed to measure normal emittance of materials up to temperatures of 1500 K in the wavelength range 2–10 μm. Chapter 7 describes the design methodology of

this experimental setup.

Chapter 2

Theoretical background

2.1 Radiative transfer equation (RTE) in participating media

The physical principle governing radiative transfer in a medium that is "radiatively participating" is the interaction of electromagnetic waves with matter. A medium can hence absorb, re-emit or scatter (re-direct) incident radiation leading to augmentation or attenuation of incident radiation in the medium as shown in Fig. 2.1. Such a medium is referred to as a participating medium. The equation of radiative energy transfer in a participating medium, then, can be written for a non-polarizing medium under radiative equilibrium and quasi-steady conditions in the continuum limit as (Modest, 2003):

$$\hat{\mathrm{s}} \cdot \nabla I_\lambda = -\kappa_\lambda I_\lambda(\hat{\mathrm{s}}, s) - \sigma_\lambda I_\lambda(\hat{\mathrm{s}}, s) + \kappa_\lambda I_{\mathrm{b}\lambda} + \frac{\sigma_\lambda}{4\pi} \int_{4\pi} I_\lambda(\hat{\mathrm{s}}_\mathrm{i}) \Phi_\lambda(\hat{\mathrm{s}}_i, \hat{\mathrm{s}}) \mathrm{d}\Omega_\mathrm{i} \qquad (2.1)$$

The above equation is frequently abbreviated as RTE. Here, the intensity in a given direction $\hat{\mathrm{s}}$ and at a given position s is given by I_λ. The subscript λ is used to indicate spectral quantity and the subscript b indicates blackbody. Equation (2.1) can be interpreted as the change of radiative intensity in a participating medium as radiation passes

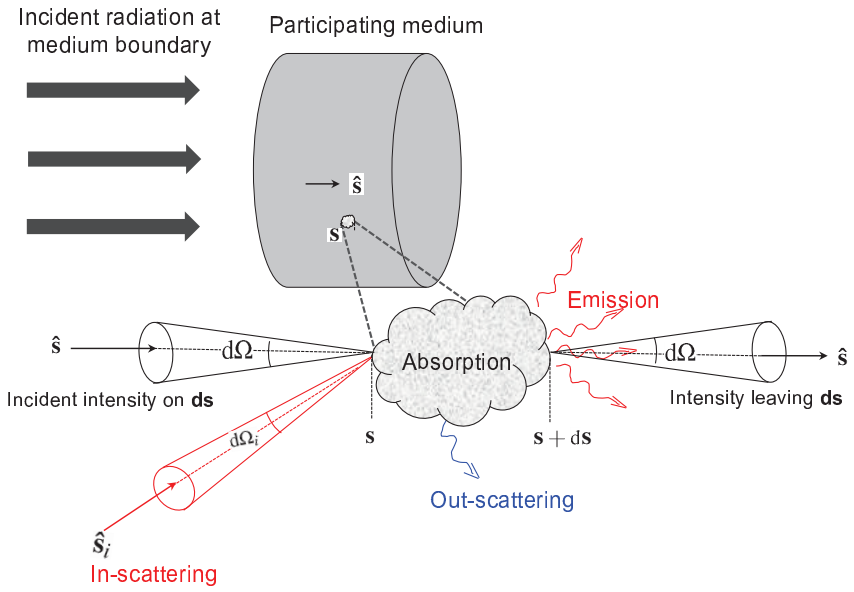

Figure 2.1: Interaction of radiation with participating media

through a differential element, equals the difference between augmentation and attenuation of intensity in the medium. The first term on the right hand side is attenuation by absorption at the location s; the second term is attenuation by (out) scattering away from the direction $\hat{s}$; the third term is augmentation by emission into the direction $\hat{s}$ and the last term is augmentation by in-scattering from direction $\hat{s}_i$ into the direction $\hat{s}$.

The properties of the medium that characterize augmentation or attenuation of radiative intensity are: absorption coefficient (κ_λ), scattering coefficient (σ_λ) and the scattering phase function (Φ_λ). Absorption and scattering coefficients carry units of inverse of length, and one way to interpret these coefficients is as the inverse of the mean free path of a photon in a participating medium before it is absorbed or redirected (scattered) from its original direction. The scattering phase function (Φ_λ) is unity if the medium scatters isotropically. Hence, the scattering phase function can be interpreted

as a weighting function that dictates the fraction of radiation scattered into a given direction. In general, Φ_λ is dependent on incident direction (of incoming scattering), $\hat{\mathrm{s}}_\mathrm{i}$, in addition to $\hat{\mathrm{s}}$, the direction along which the change in intensity is given by the RTE. However, if the medium is insensitive to incidence direction, the scattering phase function is no longer a function of $\hat{\mathrm{s}}_\mathrm{i}$. Such a medium may, however, scatter anisotropically and the scattered radiation is not distributed uniformly. This type of medium is referred to as anisotropically-scattering isotropic medium and the scattering phase function for such a medium is cast as a function of "scattering angle", θ. The scattering angle gives the angle between the incident and redirected electromagnetic wave for anisotropically scattering but isotropic medium.

Frequently, the RTE is recast in optical co-ordinates by introducing three new quantities, namely, extinction coefficient (β_λ), optical thickness (τ_λ), and single scattering albedo (ω_λ), defined as:

$$\beta_\lambda = \sigma_\lambda + \kappa_\lambda \tag{2.2a}$$

$$\tau_\lambda = \int_0^s \beta_\lambda(s')\mathrm{d}s' \tag{2.2b}$$

$$\omega_\lambda = \frac{\sigma_\lambda}{\beta_\lambda} \tag{2.2c}$$

This allows the RTE, eq. (2.1) to be rewritten as:

$$\frac{\mathrm{d}I_\lambda}{\mathrm{d}\tau_\lambda} + I_\lambda = (1-\omega_\lambda)\, I_{b\lambda} + \frac{\omega_\lambda}{4\pi}\int_{4\pi} I_\lambda(\hat{\mathrm{s}}_\mathrm{i})\Phi_\lambda(\theta)\mathrm{d}\Omega_i \tag{2.3}$$

This form enables solution to RTE to be cast as function of optical thickness, and for the simple case of non-scattering, cold media, $\omega_\lambda, I_{\mathrm{b}\lambda} = 0$, and the extinction coefficient equals the absorption coefficient. The solution to the RTE results in intensity decaying exponentially with optical thickness, known as Bouguer's law:

$$\begin{aligned} \beta_\lambda &= \kappa_\lambda \\ I_\lambda(\tau_\lambda) &= I_\lambda(0)\exp[-\tau_\lambda] \end{aligned} \tag{2.4}$$

If the extinction coefficient of the medium is constant (independent of position in the medium), substitution of eq. (2.2b) into eq. (2.4) results in:

$$I_\lambda\left(\mathrm{s}\right) = I_\lambda\left(0\right)\exp\left[-\beta_\lambda s\right] \tag{2.5}$$

Estimation of radiative properties for the case of non-scattering media then becomes relatively simple. If the intensity of radiation could be measured by a detector prior to passing through the medium and after passing through the medium, the extinction coefficient is extracted by fitting an exponent to the measured intensity through the medium.

For highly scattering media, simplification of RTE to determine radiative properties requires additional considerations because the last term in eqs. (2.1) and (2.3) representing augmentation in intensity due to incoming scattering makes the RTE an integro-differential equation which is difficult to solve. For highly scattering media, the last term in the RTE, eq. (2.1) is simplified by assuming an approximate form of the phase function. A review of approximate phase functions and the resultant simplifications to the RTE is available in (Modest, 2003; Dombrovsky and Baillis, 2010). The simplest approximate phase function is an isotropic phase function, $\Phi_\lambda = 1$. However, this assumption may not be physically true. Many participating media, such as packed beds, clouds of particles, and bubbles dispersed in a medium may scatter strongly in the forward direction. Many approximate phase functions have been employed with success for this purpose such as the Dirac-delta phase function:

$$\Phi_{\lambda,\mathrm{DD}} = 2f\delta\left(1-\cos\Theta\right) + 2b\delta\left(1+\cos\Theta\right) + (1-f-b)\Phi^*_\lambda(\Theta) \tag{2.6a}$$

where Φ^*_λ may be expanded as a Legnedre Polynomial. f and b are the fractions of radiation scattered in the forward and backward direction and Θ is the scattering angle. A popular approach is known as the "transport approximation", where b is assumed to

be zero, $\Phi^*_\lambda = 1$ and f is defined equal to the asymmetry factor, g:

$$g = \overline{\cos(\Theta)} \tag{2.6b}$$

$$= \frac{1}{4\pi}\int_{4\pi} \Phi(\Theta)\cos(\Theta)\, d\Omega \tag{2.6c}$$

If the value of g lies in the interval 0 and 1, scattering is dominant in the forward direction, and if it lies between -1 and 0, the incident wave is redirected backwards. Under transport approximation, the RTE becomes:

$$\hat{\mathbf{s}}.\nabla I_\lambda = -\kappa_\lambda I_\lambda(\hat{\mathbf{s}}, s) - \sigma_\lambda(1-g)I_\lambda(\hat{\mathbf{s}}, s) + \kappa_\lambda I_{b\lambda} + \frac{\sigma_\lambda(1-g)}{4\pi}\int_{4\pi} I_\lambda(\hat{\mathbf{s}}_i)\mathrm{d}\Omega_i \tag{2.7}$$

This enables the definition of "transport" radiative properties:

$$\begin{aligned}
\sigma_{\lambda,\mathrm{tr}} &= \sigma_\lambda(1-g) \\
\omega_{\lambda,\mathrm{tr}} &= \frac{\sigma_{\lambda,\mathrm{tr}}}{\beta_{\lambda,\mathrm{tr}}} \\
\beta_{\lambda,\mathrm{tr}} &= \sigma_{\lambda,\mathrm{tr}} + \kappa_\lambda
\end{aligned} \tag{2.8}$$

Hence, only two unknown coefficients, namely, σ^*_λ and κ_λ have to be determined in the transport RTE, instead of three unknowns in the original RTE, eq. (2.1). Another common approximate phase function encountered in the literature is the Henyey-Greenstein function:

$$\Phi_{\lambda,\mathrm{HG}} = \frac{1-g^2}{1+g^2-2g\cos\Theta} \tag{2.9}$$

The "transport" RTE, eq. (2.7) could be solved if the intensity could be integrated over the entire solid angle. The distribution of intensity with solid angle is required, and is typically assumed to be a combination of a diffuse component and a directional component (Dombrovsky and Baillis, 2010). Further, the domain is assumed to be one-dimensional, which facilitate obtaining simplified solutions to transport RTE . These techniques will be discussed in section 2.4

2.2 Theoretical Predictions of Optical and Radiative Properties

Study of electromagnetic wave propagation in complex media has been motivated historically by several applications, namely, propagation of radio waves through the atmosphere, optical phenomena in the earth's atmosphere, light scattering by particulate suspensions, and more recently, biomedical imaging in tissues. Scattering and absorption of electromagnetic waves by these media because of their complex structural and optical properties is an important phenomenon that describes the propagation of electromagnetic waves. Several approaches have been employed in this regard to either obtain the macroscopic radiative properties of the material from the knowledge of a medium's optical constants, namely index of refraction and absorption (or indirectly from dielectric functions), or, to describe the resulting electromagnetic field due to the presence of a medium. These approaches are outlined in Fig. 2.2. Keller (Keller, 1962) classifies these approaches into "honest" and "dishonest" approaches, which has been discussed in some detail by in a recent review paper (Mishchenko et al., 2011). The "honest" approaches refer to exact, closed form analytical solution to Maxwell's equations at a macroscopic scale, or the application of Quantum Electrodynamics at a microscopic scale to predict the propagation of the field through complex media. Frequently, a highly accurate direct Maxwell's equation solver is employed to arrive at a numerically accurate solution to Maxwell's equations. The "dishonest" approaches refer to phenomenological routes and approximations to Maxwell's equations.

If the medium is geometrically simple, such as an array of spheres sufficiently far away from each other, and small or comparable in size to the wavelength, then classical solutions to Maxwell's equation such as Mie theory becomes applicable. Theoretical prediction of radiative properties requires knowledge of the medium's refractive index

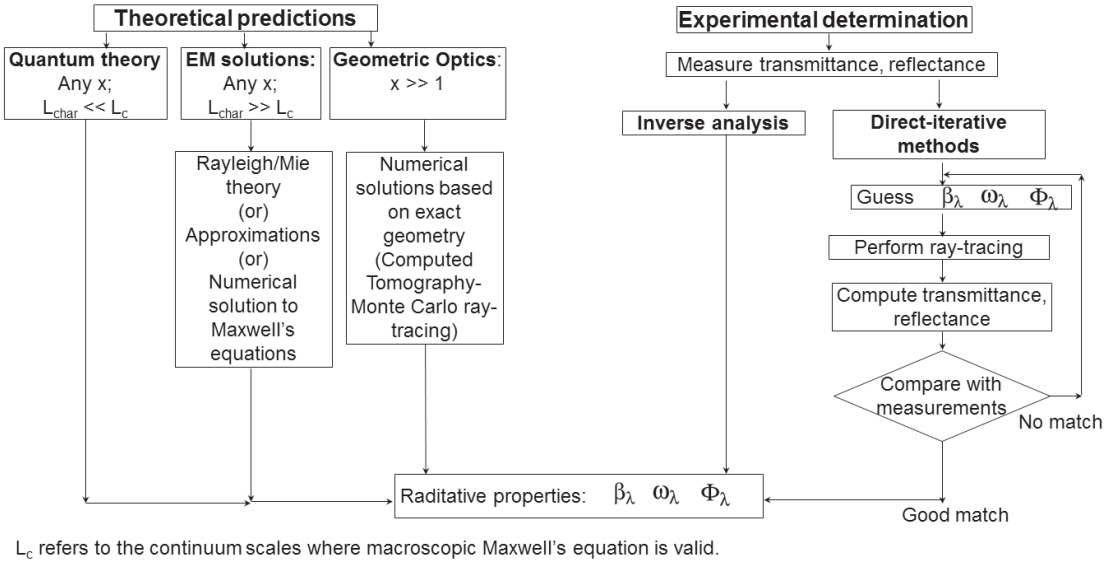

Figure 2.2: Methods to determine radiative properties of participating media

(or dielectric functions) and structural features such as characteristic size of sphere for an array of spheres, and the spacing between the spheres. A dimensionless size parameter of a spherical particle is defined:

$$x = \frac{2\pi a_{\mathrm{p}}}{\lambda} \tag{2.10}$$

where a_p is the radius of the sphere and λ is the wavelength of the electromagnetic wave. Based on the characteristic size, the solution techniques can be classified into quantum theory (x $\ll$ 1), solution to Maxwell's equation (valid when the particle size is larger than nano-scale) such as Rayleigh theory (x $<$ 1) or Mie theory (x $\approx$ 1) collectively referred to as "EM solutions", or geometric optics (x $\gg$ 1).

An important, but inherent assumption in the EM solutions typically applied to a system of particles is that scattering phenomenon corresponds to a domain referred to "independent scattering", or, the presence of adjacent particles does not influence

scattering from a single particle. This effect, known as the far-field approximation is an important assumption of the micro-physical approach to radiative transfer (Kahnert, 2003; Mishchenko, 2006). When each particle in a disperse system is in the far-field of other particles, each particle absorbs and scatters radiation as though other particles did not exist, and there is no systematic phase relation between the scattered waves of different particles. In other words, scattering is from individual particles, and theoretical predictions for individual particles can be extended to predict radiative properties of a disperse system of particles (Dombrovsky and Baillis, 2010).

For regular structures, such as spherical particles of equal or different sizes, radiative properties are determined by extending Rayleigh or Mie scattering and are documented in the books on radiative transfer (Modest, 2003; Siegel and Howell, 2003; Bohren and Huffman, 1998; van de Hulst, 1981). Besides simple and regular geometries, EM theory has also been successfully implemented in the prediction of radiative properties for irregular geometries and particle mixtures such as particle beds, clouds of spherical particles, suspensions etc. The size parameter x, and particle volume fraction f_v determine whether scattering is independent in a medium. One would expect that when the volume fraction of the particles is large (densely packed particles) or when the particle size parameter is large, the scattering behavior of the particles departs from independent scattering. When scattering cannot be treated as independent, the predicted radiative properties from EM theory deviate from actual radiative properties. In such cases, the independent scattering results from EM theory must be appropriately corrected to account for dependent scattering effects. Additionally, in a disperse system, particles can either be uniformly sized, also referred to as monodisperse particles, or have a size-distribution, referred to as polydisperse particles. In the latter case, the size-distribution should be known a priori to prediction of radiative properties by EM solutions.

Examples of using EM solution to predict radiative properties either in the dependent or the independent scattering regime for particles of size corresponding to Mie regime can be found in (Agarwal and Mengüç, 1991; Singh and Kaviany, 1992; Manickavasagam and Mengüç, 1993; Mengüç et al., 1994; Dombrovsky et al., 2005; Bahador and Sundn, 2008). Additionally, Mie solutions to radiative properties of infinite and finite cylinders are available in (Barabás, 1987; Kai and D'lessio, 1995; Uzunoglu et al., 1978; Waterman and Pedersen, 1998). For smaller spherical particles, the Rayleigh scattering limit simplifies the solution to Maxwell's equation. Rayleigh scattering theory has been applied to obtain the radiative properties of aerosols (Penndorf, 1962) and soot particles (Köylü and Faeth, 1993). For non-spherical small particles in the Rayleigh limit, analytical solutions of absorption and scattering are available in (Bohren and Huffman, 1998; van de Hulst, 1981).

In the limit of $x \gg 1$ geometric optics, an approximation to the EM solution becomes applicable, where the propagation of electromagnetic radiation through matter can be obtained by treating the radiation as rays, and employing laws of geometry. Radiative properties in the limit of geometric optics are predicted by tracking the path of a large number of rays through the medium. Radiative properties have been determined by geometric optics for clouds (Twomey and Bohren, 1980; Yang et al., 2001; Zhang et al., 2004), large bubbles (Kokhanovsky, 2003; Wu et al., 2007), and for large particles (Randrianalisoa and Baillis, 2010; Kamiuto, 1988; Yang and Liou, 2009). A statistical method such as the Monte-Carlo (MC) method (to be introduced in a later section) is employed, and it requires an accurate mathematical representation of the medium's geometry so that path of the rays are followed through the medium. This geometric representation is provided by techniques such as x-ray or computer tomography. Examples of MC technique applied to media that are geometrically represented either by tomography or by other techniques can be found in (Tancrez and Taine, 2004; Rousseau et al.,

2007; Petrasch et al., 2007; Coquard and Baillis, 2006; Haussener et al., 2009). This technique is commonly employed for obtaining radiative properties of packed beds, reticulate ceramics and metallic foams.

2.3 Experimental Methods

In situations where solutions to Maxwell's equation are computationally challenging to implement or when it may not be physically representative, such as when dependent scattering dominates, experimental techniques in combination with numerical procedures to identify radiative properties from experimental data are employed. Most engineering materials fall into this category. Experimental techniques involve measurement of wavelength, temperature and angular direction dependent radiative fluxes, usually cast into transmittance, reflectance and emittance. Simplified solutions to the RTE are compared to experimental data in order to identify the radiative properties.

Experimental techniques pertinent to the measurement of radiation are known as radiometry. Techniques employed for resolving spectral content of radiation are known as spectroscopic radiometry. For participating media, this usually involves irradiating the media by a source of radiation, such as arc lamps or lasers. The radiative power transmitted through, reflected or emitted by the medium is measured using a detector. Spectral information of transmitted, reflected or emitted radiation is recovered by irradiating the medium with a tunable monochromatic source such as tunable lasers, or more commonly, a monochromator or a spectrometer. The monochromator disperses the incident beam into narrow bands of monochromatic radiation using diffraction gratings. Because monochromatic radiation is achieved by dispersion, this type of system is referred to as "dispersive" spectroscopy system. In dispersive spectroscopy setups employed for transmittance measurements, it is important to modulate the incoming

radiation to prevent ambient radiation, stray light from reflection at optical surfaces, and in the case of transmittance and reflectance measurements, radiation emitted by the participating medium from entering the detector. This is because the measurement setup is used to measure only the fraction of incident radiation that passes through or is reflected by the participating medium. Modulation is accomplished by means of an optical chopper which consists of blades mounted on a rotating wheel that chop the beam from the source at the frequency of rotation of the wheel, known as "modulation frequency". Signal acquisition devices in radiometric systems process the acquired signal so that the signal acquired when the beam is being chopped is subtracted from that when the beam irradiates the sample. Hence, the resultant output from the signal acquisition device indicates the true fraction of radiation passing through the medium. A complementary measurement technique to the dispersive spectroscopy system involves Fourier Transform Infrared (FTIR) spectroscopy systems. The FTIR system constructs an interference pattern from a source of radiation using a beam splitter. Interference is created as a result of the incident beam being split by the beam splitter into two beams with a phase difference. The interference pattern is scanned by the FTIR detector, and the spectral intensity of the source is extracted from the interference pattern by the Fast Fourier Transform algorithm. Modulation is typically not employed in FTIR spectrometers, because the contribution of stray signal to the interference pattern is small. Further, FTIR spectrometers are typically employed for measurements only in the infrared spectral ranges.

Two types of measurements are frequently carried out in radiometry. Because the radiative flux is dependent on direction, in addition to wavelength and temperature, radiative energy leaving a surface can be measured along a direction, or integrated over a hemisphere. If energy leaving the surface of the medium is integrated by an integrating sphere, which is a diffusely reflecting surface, directional dependence of intensity is

not preserved. This is due to the multiple diffuse reflections at the surface of the integrating sphere, which entirely erases any directional information from the measured signal. This type of measurement is called hemispherical measurement and can either be normal-hemispherical transmittance or reflectance, as shown in Fig. 2.3. Measurements carried out without the integrating sphere preserves directional information in the measured signal, and is known as directional measurement. The incidence beam is usually normal to the surface of the measurement sample, and the term "normal" is prefixed to the hemispherical or directional measurements. The direction of radiative energy measured can be changed by using a goniometer, which consists of a rotating arm on which focusing optics and radiation detection systems can be placed and rotated at any angle in the forward direction. Measurement of directional intensity in the backward direction is very difficult to accomplish, because the detector must be positioned adjacent to the optical systems used for directing the incident beam.

Radiant energy leaving a medium is not only dependent on wavelength and direction, but also on its temperature. Materials processing, plasma spray coating, and other ceramic applications typically require radiative characterization of materials at high temperatures, typically on the order of 1500–2000 K. In the present work, ceria cycles in a solar thermochemical reaction between temperatures of 1500 K during the reduction stage of the cycle and 1000 K during the oxidation stage. Hence, radiative characterization of ceria must account not only for wavelength and morphology dependence, but also temperature dependence of the material's optical properties. Studies documenting measurement of temperature dependent radiative properties for opaque or semitransparent media at elevated temperatures can be found in (Sarou-Kanian et al., 2005; Manara et al., 2009; S. Jeon and Lee, 2010). Transmittance, reflectance (Beder et al., 1971; Cabannes and Billard, 1987) or emittance (Moore et al., 2011a,b; del Campo et al., 2011; Markham et al., 1990, 1993; Rozenbaum et al., 1999) are typically

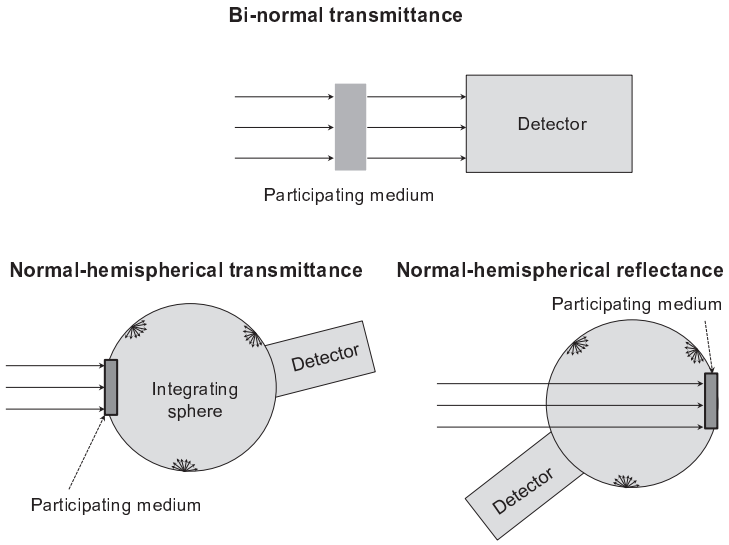

Figure 2.3: A schematic to illustrate bi-normal and normal-hemispherical measurements.

measured as functions of wavelength and temperature and a suitable computational technique (Dombrovsky et al., 2011) is used for identification of scattering and absorption characteristics. Heating is either accomplished by a furnace, or more commonly by a laser source. Temperature measurement is by thermocouple, or by using the Christiansen wavenumber method in the case of emittance measurement. The Christiansen wavenumber refers to the wavelength at which the emittance of the material is unity. The material then behaves like a blackbody at that wavelength, and blackbody functions that relate wavelength, direction, temperature and intensity can be employed for recovering the temperature. A review of measurement methods to overcome some of the inherent difficulties in measurement of radiative properties at elevated temperature can be found in ref. (Rozenbaum et al., 1999).

2.4 Inferring Radiative Properties from Experimental Data

In radiative transfer problems, the measurable quantities are emitted, transmitted or reflected radiant energy as a function of wavelength, temperature, morphology and direction. The quantities that are used for engineering heat transfer analysis are the radiative properties that feature in the RTE, namely, extinction coefficient, scattering albedo and scattering phase function. Further, in most engineering problems, because the radiant energy integrated over a hemisphere is more useful for determination of heat flux or rate of heat transfer due to radiation, it is sufficient to invoke the transport approximation eq.(2.6b), and obtain the transport scattering coefficient and the absorption coefficient. The process of obtaining radiative properties from experimental data is referred to as inverse analysis by some authors. Figure 2.4 is a schematic adopted from ref. (Bohren and Huffman, 1998) that illustrates the difference between direct and inverse analysis. In the direct problem, the radiative properties of the participating medium are known and the intensity distribution is sought by solving the RTE with suitable boundary conditions. In the inverse problem, the solution to the RTE is known via experiments, namely bi-directional and directional-hemispherical measurement of transmittance and reflectance or normal emittance. The radiative transfer equation is solved after simplifications using approximate solution methods, and the solution is inverted to obtain the radiative properties.

Identification techniques to infer radiative properties from experimental data are summarized in the review papers (Baillis and Sacadura, 2000; Sacadura, 2011). One class of solution techniques does not solve the RTE explicitly, but assumes a mathematical function of the solution, such as the source term on the RTE. A guess value is

assumed for the radiative properties and the solution to RTE, and consequently transmittance and reflectance are fit as functions of the properties by empirical curve fits. The analytical and experimental transmittance and reflectance are compared, and the sum-of-squares error is computed to examine if the error is acceptable. If the error is large, a new guess for the radiative properties is made, and the procedure is repeated until the error is minimized. Examples of this technique can be found in (Nicolau et al., 1994; Baillis et al., 2002; Loretz et al., 2008; Lipiński et al., 2008; Liang et al., 2011). Other techniques have a stronger physical basis, and invoke approximations such as the transport approximation to simplify the RTE, assuming suitable boundary conditions. Some common approaches are the P_1 approximation, the Spherical Harmonics method and the Schuster and Schwartzchild method, also known as two-flux approximation (Modest, 2003). For further simplification, the medium is assumed to be one-dimensional. Such numerical techniques were employed recently to study radiative characteristics of disperse systems, foams, ceramics and bubbles (Hendricks and Howell, 1996; Manara et al., 1999; Dombrovsky et al., 2007, 2006; Eldridge and Spuckler, 2008; Dombrovsky et al., 2010; Mengüç et al., 1994; Agarwal and Mengüç, 1991; Singh and Kaviany, 1992). From accuracy considerations, transport radiative properties sufficiently capture the radiative transfer characteristics in combined heat transfer problems (Dombrovsky, 2012b).

Given the nature of radiative transfer in participating media (the form of the RTE), any deterministic solution to the RTE, except exact solutions from electromagnetic theory, relies on a certain degree of approximation allowing the simplification of the governing equations. Further, exact solutions to Maxwell's equations are applicable to only highly idealized media. One class of statistical techniques known as the Monte

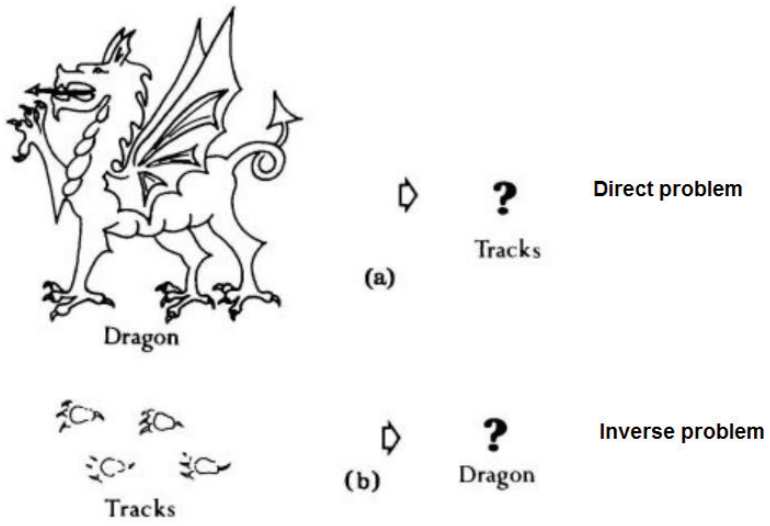

Figure 2.4: An illustration of the direct and inverse problem. Adopted from (Bohren and Huffman, 1998).

Carlo (MC) method has been employed to solve radiative transfer equation statistically. The origin of the Monte Carlo method dates back to the prediction of individual neutron behavior during the Manhattan project. Since then, techniques based on the MC method have been widely adopted to predict mean behavior in many physical phenomena. Howell makes the case for MC- based techniques to solve problems in radiative transfer (Howell, 1998). MC-based techniques applied to radiative transfer rely on statistics for prediction of average behavior of photon bundles in a participating medium. Tracing the history of rays is known as "ray-tracing", and prediction of radiative properties in a participating medium consists of the following steps:

1. Radiative properties of the medium are assumed. Estimates of radiative properties may be obtained from an approximate solution method (such as solutions for optically thick media), by inverse analysis, or by EM solution. Note that only an estimate is required at this stage and a rigorous implementation of any of the

methods is unnecessary.

2. An MC technique, such as ray-tracing is performed by launching a large number of rays (often on the order of 10^7 in modern computations, but sufficiently large to compute statistics accurately) through the medium and following their trajectories. The trajectories are related to the medium properties and follow probability distributions.

3. Quantities such as transmittance and reflectance are computed and are compared to experimental data or scaling the predictions of electromagnetic theory for a single particle.

4. The procedure is repeated until a good match between the experimental data or scaled up EM predictions and MC results is obtained.

Recent examples of MC based techniques to obtain radiative properties of participating media can be found in (Subramaniam and Mengüç, 1991; Hendricks and Howell, 1996; Argento and Bouvard, 1996; Coquard and Baillis, 2004; Jäger et al., 2009; Coray et al., 2010). The Monte-Carlo method is a statistical technique, and requires a large number of rays to be launched through the medium for accurate computations[1] . However, alternate hybrid MC techniques may allow coupling of an approximate solution method and a Monte-Carlo based method, resulting in the reduction of number of rays required for accurate computations (Farmer and Howell, 1994).

[1] Recall that precision error in a statistical distribution scales inversely with the number of samples in the distribution. Hence, the error associated with the ray-tracing solution decreases when the number of rays launched is large.

2.5 Summary

Radiative characterization of materials has gained importance in many applications. The present work focuses on solar thermochemical applications, but ceramics processing, combined heat transfer modeling in metal or ceramic foams, thermal barrier coatings, combustion and soot formation, scattering and absorption of radiation by atmospheric aerosols and clouds are some engineering applications where determination of radiative properties is significant. Many different approaches have been attempted with varying degrees of success to identify extinction coefficient, scattering albedo and scattering phase function. For most engineering materials, a successful approach involves measurement of transmittance and reflectance, coupled with approximate solutions to the radiative transfer equation to identify radiative properties with good accuracy for heat transfer calculations. One of the challenges that several of the studies cited in this chapter encounter is the determination of scattering phase function for complex materials with irregular geometries, where idealizations such as Mie or Rayleigh theory are not applicable. Several researchers employed the transport approximation with approximate phase functions when possible, and were able to retrieve partial directional scattering characteristics. However, from accuracy considerations for engineering analyses, transport radiative properties have been found to sufficiently capture the physics of radiative transfer in combined heat transfer processes.

Chapter 3

Experimental techniques for radiative characterization at ambient temperature

3.1 Methodology

Thermal transport analysis of solar thermochemical cycles with novel ceria structures requires its transport radiative properties, namely transport scattering coefficient and absorption coefficient, as a function of wavelength and temperature. Traditional approaches to obtaining radiative properties at ambient temperature for engineering materials involve measuring transmittance and reflectance as a function of wavelength and employing a suitable inverse procedure to obtain radiative properties. For obtaining transport radiative properties, the simplest approach employs measurement of directional-hemispherical transmittance and reflectance. Many commercially available bench-top UV-VIS-NIR spectrometers equipped with integrating spheres can measure directional-hemispherical transmittance and reflectance. One of the short-comings of

the commercial spectrometers is the limited dynamic range of measurements. Thus, bench-top spectrometers become unsuitable for measuring directional-hemispherical transmittance of optically thick materials, typically of optical thickness 50. Even samples of thickness less than 1 mm have extremely low transmittance, typically on the order of 1 %. Another limitation of the normal-hemispherical measurements is the unsuitability of the measurements for inferring direction-dependent radiative intensity, and consequently, the scattering phase function.

An in-house experimental setup was developed to overcome the limitation of poor accuracy of measurements of transmittance, and this setup is capable of measuring bi-normal transmittance up to 0.001 % corresponding to five orders of attenuation of the incident beam by a material. While this setup still does not provide quantitative information on the directional-scattering characteristics of the material, intensity in the near-normal direction can be obtained from this setup, which may provide incomplete but partial information on directional-scattering characteristics, especially when combined with the normal-hemispherical measurements.

In the present study, two experimental setups are employed. The in-house spectroscopy setup is modified to improve spectral accuracy as well as linearity for measuring bi-normal transmittance, especially in the spectral range 0.9–1.7 μm and an off-the-shelf spectrometer equipped with an integrating sphere that is capable of measuring directional-hemispherical transmittance and reflectance in the spectral range 0.3–2 μm. These two experimental setups facilitate measurement of bi-normal transmittance, and normal-hemispherical transmittance and reflectance of most common engineering ceramics in the UV-VIS-NIR spectrum. The setups are calibrated to ensure accuracy and linearity of measurements. Based on the experimental data, qualitative conclusions on radiative characteristics of the material can be drawn.

3.2 Bi-normal transmittance setup

A schematic of the bi-normal transmittance setup is shown in Fig. 3.1. It consists of a 300 W short-arc ozone-free xenon lamp (#1) which serves as the source of radiation. Two Newport MS257 monochromators (#4) incorporating four diffraction gratings and motorized slits were used as a tunable source of nearly monochromatic radiation in the range 0.3 to 1.7 μm. The monochromators consist of gratings which disperse an incident beam into monochromatic bands based on the principle of diffraction. Description and characterization of gratings used in the bi-normal transmittance setup is available in Appendix A. In order to eliminate higher-order diffraction peaks, cut-on optical filters mounted on a filter wheel were used. Transmittance of the optical filters along with their cut-on wavelengths are documented in Appendix A. An optical chopper (#3) made of rotating blades was employed to modulate the beam so that stray light and emitted radiation from the sample and surroundings do not reach the detector. Translatory-rotary lens holders (#5a) and (#5b) of modular design were used to mount lenses of different type, such as plano-convex, biconvex, etc. of different focal lengths can be interchangeably held in the assembly for collimating or focusing the beam and to adjust the axial position of the lens in the lens holder for optimal focusing. In the experimental results reported in Chapter 5, two plano-convex lenses of focal length 50 mm and 75 mm were used to collimate the incident beam (#5a) and focus the transmitted beam (#5b), respectively.

Calibrated silicon and germanium photo-detectors with an active detection surface of 5 mm diameter convert incident radiation on the detection surface into a voltage signal. The wavelength range of these measurements is constrained primarily by the response of the silicon and germanium detectors; the response of the silicon detector is linear in the spectral range 0.3–1.0 μm and the response of the germanium detector is

linear in the spectral range 0.9–1.7 μm, effectively constraining the spectral range of the bi-normal transmittance between 0.3–1.7 μm. An integrated phase-sensitive digital lock-in amplifier and chopper driver (#10) was used to acquire and amplify the voltage signal from the detector. Spectral interval and sampling rate of measurement was specified using a PC equipped with Newport TRACQ software for data acquisition and control. Bi-normal (narrow cone) transmittance of the samples, $T_{\text{d-d}}$ is defined as the ratio of signal in volts reaching the detector with the sample, $\dot{Q}_{\text{d}}$ to that without the sample $\dot{Q}^0_{\text{d}}$:

$$T_{\text{d-d}} \stackrel{\text{def}}{=} \frac{\dot{Q}_{\text{d}}}{\dot{Q}^0_{\text{d}}} \tag{3.1}$$

The monochromators can be operated in two configurations, namely, subtractive-double (Fig. 3.1) and single (Fig. 3.2) configuration. In the single configuration, only one of the two monochromators is used to produce a narrow beam of monochromatic radiation. In the subtractive-double configuration, the exit slit of the first monochromator (referred to as "master") is attached to the entrance slit of the second monochromator (referred to as "slave"). The subtractive-double configuration typically results in improved spectral accuracy at the cost of signal-to-noise ratio at the exit of the monochromators. The signal-to-noise ratio is drastically reduced in the subtractive-double configuration because of the presence of additional mirrors in the slave monochromator, and optical losses due to imperfect reflection at the surfaces of the additional mirrors.

The single and the double monochromators were calibrated using an Oriel instruments Hg-Ar 6035 "pencil ray" lamp, capable of producing narrow spectral lines by excitation. Metallic neutral density filters of known optical density were used to calibrate the apparatus. Optical density of the neutral density filter is given by:

$$\text{OD} = -\log_{10} T \tag{3.2}$$

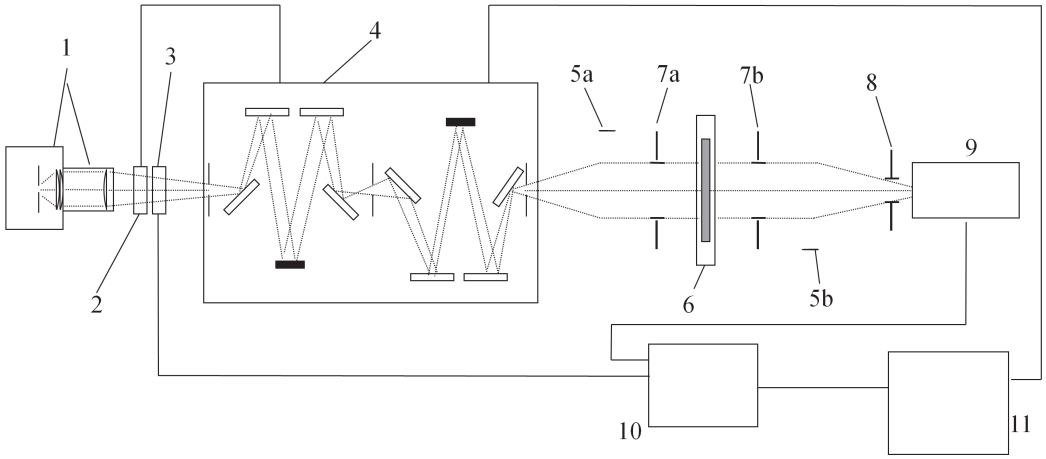

Figure 3.1: Experimental setup for measurement of binormal transmittance: subtractive-double configuration

For instance, an OD 1.0 filter has an optical density equal to unity over a wide spectral range, typically 0.3–1.0 μm. Consequently, transmittance of the neutral density filter is known in this spectral range. The UV-VIS-NIR setup is calibrated by measuring this known value of transmittance. This procedure also verifies that the dynamic range, i.e. the ability of measurement system to measure low values of transmittance anticipated in the experiments. OD 3.0, corresponding to three orders of magnitude attenuation of the incoming radiation was measured. Calibration data of the experimental setup for the pencil-ray calibration and the neutral density filters are provided in Appendix A (Table A.4 and Fig. A.6, respectively). Measured transmittance for various optical densities over the 0.4–1.1 μm spectral range agree well with the known transmittance of the neutral density filters over the entire spectral range. Further, both single and subtractive-double configurations were found to be of adequate spectral resolution.

The spectrum of Xe arc lamp measured by the bi-normal transmittance setup is

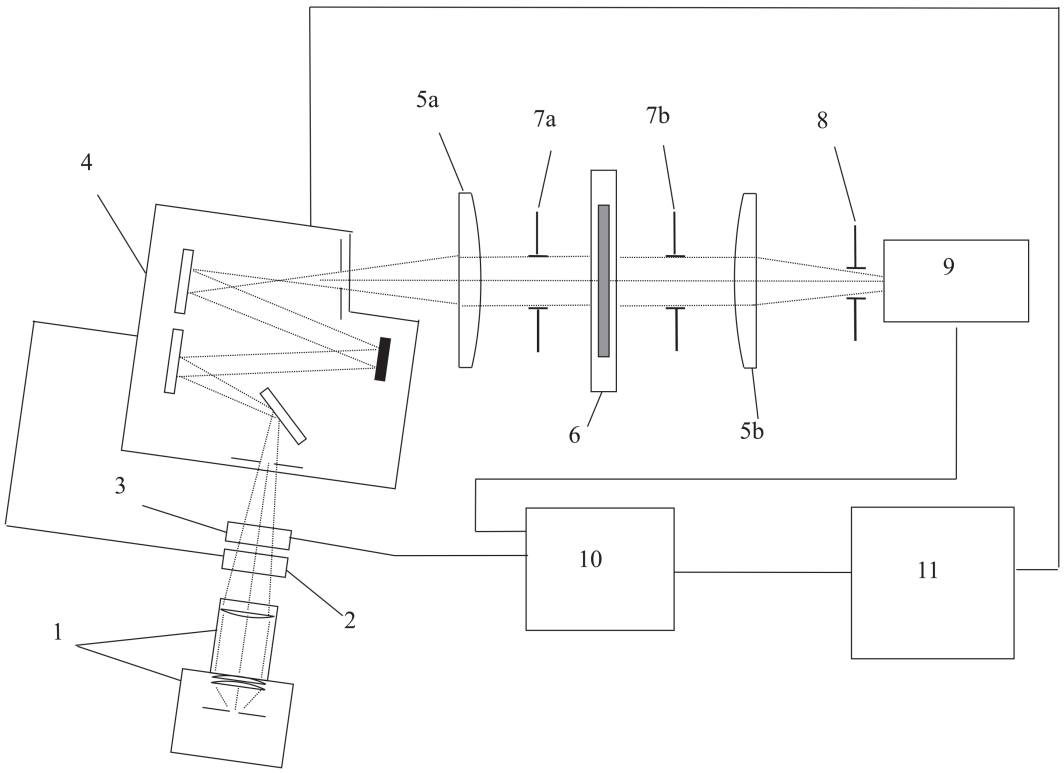

Figure 3.2: Experimental setup for measurement of bi-normal transmittance: single configuration for improved signal-to-noise characteristics

shown in Fig. 3.3. Because the detectors typically measure an integrated quantity of radiative energy over a small surface area over a narrow cone angle of collection (rather than at a single direction), this quantity is treated as "radiative power" rather than intensity. Sharp lines of excitation can be observed in the lamp spectrum, and are characteristic of the xenon arc lamps. Comparing the radiative power obtained by the bi-normal transmittance setup to the irradiance of the lamp measured by the lamp manufacturer (provided in Appendix A, Fig. A.1), it can be seen that the bi-normal transmittance setup is capable of measuring narrow spectral lines (measured at a spectral interval of

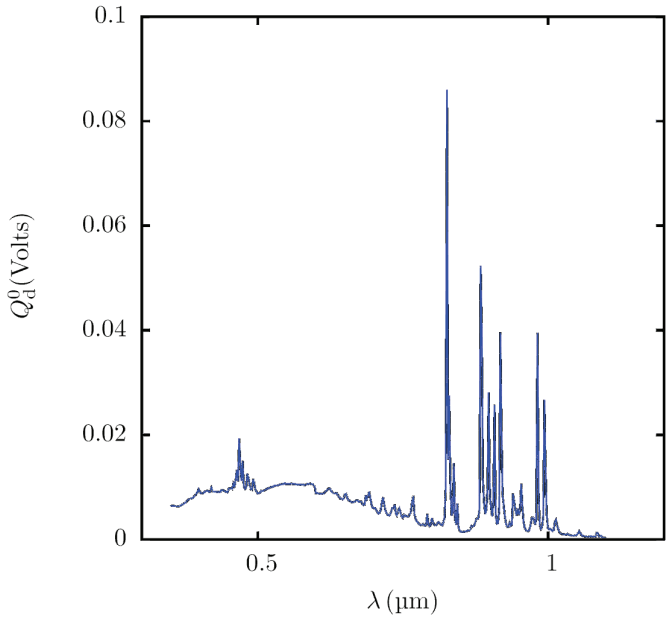

Figure 3.3: Spectrum of the xenon arc lamp measured by the bi-normal transmittance setup

0.002 µm) with good repeatability. The measured lamp spectrum also shows good qualitative agreement with the irradiance measured by the lamp manufacturer.

3.3 Normal-hemispherical transmittance and reflectance

Figure 3.4 shows a schematic of the experimental setup used to measure directional-hemispherical reflectance in the spectral range of 0.35–2 µm. It consists of a Perkin-Elmer Lambda 1050 spectrophotometer equipped with a Labsphere 150 mm integrating sphere diffusely coated with Spectralon coating. The Lambda 1050 spectrophotometer consists of two lamps that are sources of radiation: a deuterium lamp for measurements in the spectral range 0.25–0.865 µm and a tungsten-halogen lamp in the spectral range

0.865–2.5 μm. The beam from the source lamp passes through a chopper, which alternately provides a sample beam (SB) for irradiating the sample during measurements and a reference beam (RB) for comparison. Consequently, two separate beams enter the measurement chamber, with the reference beam irradiating the reference port (RF) of the integrating sphere after getting reflected by mirrors M3, M4 and M5 and the sample beam irradiating the transmittance port (T) or the reflectance port (R) after getting reflected by mirrors M1 and M2. The integrating sphere is coated with Spectralon, with surface reflectivity of 99 % in the spectral range 0.25 to 2.5 μm. A removable baffle attachment, S ensures that for highly specular surfaces, both diffuse and specular reflectance can be measured. The diffuse component is measured by removing the baffle, which causes the specular component to be reflected away by mirrors, thus preventing it from reaching the detectors. Two detectors with thermoelectric cooling collect the signal from the integrating sphere: PbS detector operating linearly in the spectral range 0.9–2.2 μm, and a photomultiplier tube operating linearly in the spectral range 0.3–0.87 μm. The linearity of the detectors limit measurements in the 0.85–0.93 μm and so for the normal-hemispherical measurements, this narrow range is omitted.

Normal- hemispherical transmittance is obtained by mounting the sample holder on to the transmittance port (T) of the integrating sphere. Normal-hemispherical reflectance is obtained by mounting the sample holder on to the reflectance port (R) of the integrating sphere. The baffle attachment is removed, and normal-hemispherical transmittance or reflectance is then defined as the ratio of the signal acquired by the detector from the sample beam to that from the reference beam.

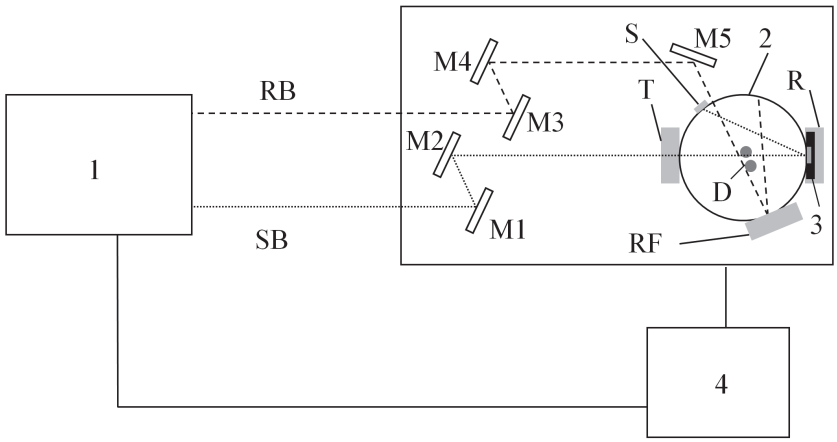

Figure 3.4: Experimental setup for measurement of normal-hemispherical transmittance and reflectance

Chapter 4

Optical and morphological characterization of ceria

Materials for solar-thermochemical reactors typically consist of a heterogeneous reacting media contained in a reactor. Several different types of reactor geometries have been designed (Steinfeld, 2005). From a radiative transfer and chemistry standpoint, morphological features of the porous medium are crucial to determining the reaction rates and temperature of the reactor. A reacting medium with high specific surface area and porosity, and optical characteristics such as strong absorption of incident solar energy in the ultra-violent and visible spectral range, as well as weak transparency in the near-infrared is highly desirable because these characteristics facilitate higher reaction rates and the ability to reach the required temperature in the reactor for driving the cyclic chemical reaction. Morphological and optical characterization of ceria structures is performed in the present chapter. Fabrication techniques employed by collaborators are also briefly presented.

4.1 Fabrication and morphological characterization

As a part of the present work, collaborators from California Institute of Technology and the Department of Chemistry at the University of Minnesota developed and optimized a few different pore geometries and morphologies for the ceria-based solar thermochemical reactor. Samples of macroporous structure with two different porosities were fabricated using sintering techniques by the materials research group at the California Institute of Technology. Nano-structured three dimensionally ordered macroporous ceria inverse opal powder was prepared by a colloidal-crystal templating technique by the materials research group at the Department of Chemistry, University of Minnesota. These two materials are the focus of radiative characterization of the present work. The samples were chosen in order to facilitate meaningful comparison of radiative properties as a function of pore morphology and porosity. Additionally, to characterize optical properties of bulk crystalline ceria, a sample of ceria thin film deposited on a Yttria Stabilized Zirconia (YSZ) substrate was provided by California Institute of Technology. This thin film was a non-scattering sample of absorbing, reflecting and refracting ceria which was used to infer its absorption characteristics and aid in obtaining its optical constants (index of refraction and absorption).

4.1.1 Sintered ceria discs

Two types of samples of porous ceria ceramics were fabricated from cerium (IV) oxide (Alfa Aesar 11328) powder by the materials group at California Institute of Technology for radiative characterization (Liang et al., 2011):

1. Dense pellets with porosity $p_1 = 0.08 \pm 0.02$:

The dense discs were prepared by first mixing the ceria powder with 1 wt. % polyvinylpyrrolidone binder dissolved in isopropanol. The dried powder was uniaxially pressed

into 13 mm cylindrical discs at 5 metric tons for 2 min. The discs were fired in stagnant air at 600°C for 2 h and 1,500°C for 10 h. The pellets were then fractured, then cross-section polished to 3 μm roughness and thermally-etched by annealing at 1,400°C for 2 h. The 95% confidence intervals for the sample thickness were estimated to be $\pm$ 0.1 mm and the porosity p_1 was obtained based on a pictometric density measurement. Resulting sample diameter was 12 $\pm$ 0.2 mm. Table 4.1 lists the thickness of the samples that were used in the present work. The porosity p_1 was measured using Archimedes method.

2. Porous samples with porosity p_2 = 0.72 $\pm$ 0.05:

The porous discs were prepared by first ball-milling the ceria powder in anhydrous ethanol with graphite (Alfa Aesar 14735, 100 mesh) and starch (Mallinckrodt 4006-04), which served as fugitive pore-forming agents, in a 10:45:45% vol.% ratio. The dried powder was uniaxially pressed into a 15 mm cylindrical disc at 1 metric ton for 3 s, and fired in flowing air at 1,000°C for 2 hours and 1,500°C for 5 hours. The 95% confidence intervals for the sample thickness were estimated to be $\pm$ 0.25 mm. The diameter of the samples was 12 $\pm$ 0.2 mm, and table 4.1 lists the thickness of the samples that were used in the present work. The porosity p_2 was measured by measuring mass and volume of the samples and employing bulk density of ceria. Archimedes method typically results in large errors for higher porosity, and thus this method was employed for the porous samples. Scanning Electron microscope images were obtained using a Hitachi S4700 scanning electron microscope at the Characterization Facility, University of Minnesota. The samples were coated with 10 nm gold-palladium coating using a sputter coater because of the dielectric behavior of ceria. Figures 4.1(a) and 4.2(a) shows scanning electron microscope (SEM) images of the dense and porous ceria ceramics obtained at the normal viewing angles and figures 4.1(b) and 4.2(b) at 45° viewing angle respectively. Images obtained at 45° viewing angle indicate that the

Table 4.1: Thickness of the cerium dioxide samples

Sample type	L (mm)				
1 (dense)	0.76	1.22	1.40	1.88	
2 (porous)	0.61	0.71	1.02	1.47	1.92

pores of the dense ceramics are spherical whereas the grains and pores of the porous ceramics are irregularly shaped. Orientation of grains and pores of the porous ceramics is random. Both types of ceramics are characterized as isotropic and homogeneous because of the absence of anisotropic features such as elongated cracks or filaments.

4.1.2 3DOM ceria powder

Three dimensionally ordered macroporous solids (3DOM) also known as inverse opals are prepared with a template of colloidal monodisperse spheres assembled to form a crystalline array structure periodic in three dimensions. A sol-gel precursor then fills the gap between the spheres and is solidified, and the template spheres are removed by techniques such as calcination, dissolving using a solvent, etc. The resulting material is an "inverse opal" with face-centered cubic (fcc) structure for macropores. The macropores are typically a few hundred nanometers in diameter, and the surrounding skeletal nodes that form the fcc arrangement are of tens of nanometers. Because of its high porosity and specific surface area, 3DOM structure of materials such as silica, zinc oxide, alumina have gained popularity in many different industrial applications such as electrochemical processing in fuel cells, batteries, in micro-channel reactors etc. A review of the synthesis and properties of 3DOM material is available in (Stein et al., 2007).

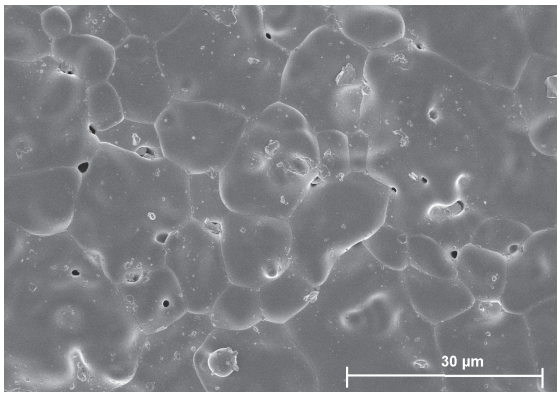

(a)

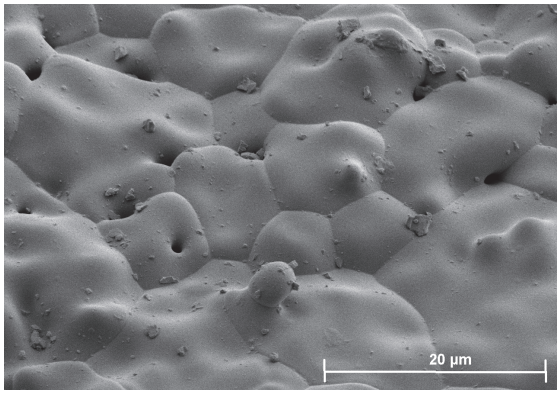

(b)

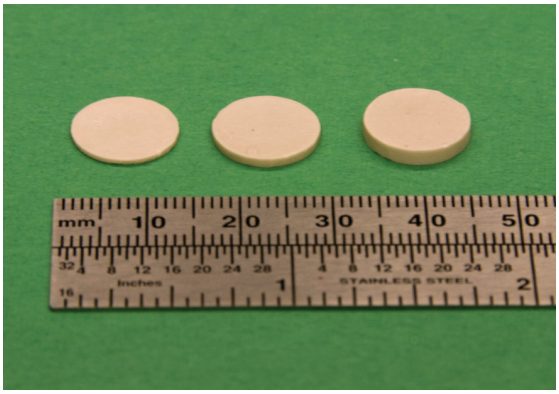

(c)

Figure 4.1: SEM images of the dense sample taken at (a) Normal viewing angle and (b) 45 ° viewing angle. (c) Photograph of dense samples of various thicknesses

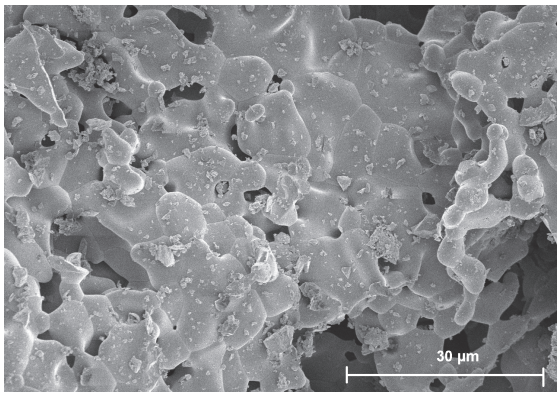

(a)

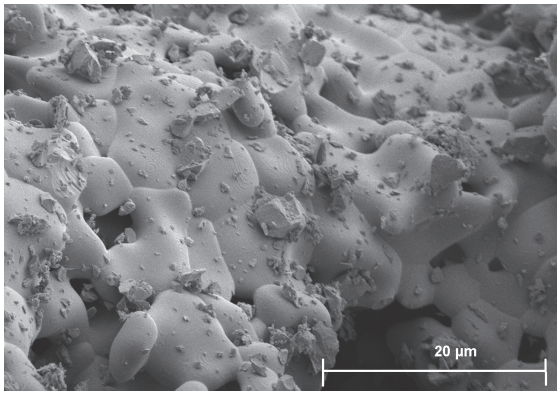

(b)

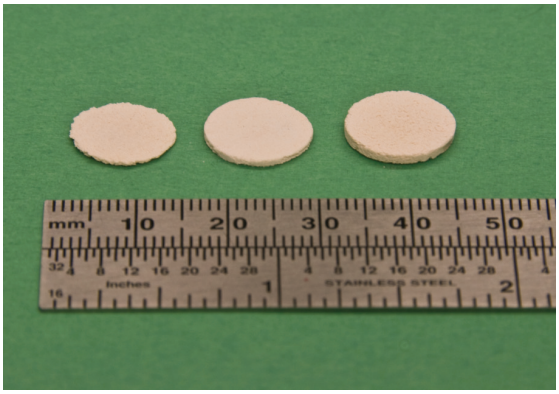

(c)

Figure 4.2: SEM images of the porous sample taken at (a) Normal viewing angle and (b) 45 ° viewing angle. (c) Photograph of porous samples of various thicknesses

3DOM ceria samples were synthesized in powder form using a technique summarized in (Venstrom et al., 2012). The colloidal crystal template was made of monodisperse polymethyl methacrylate (PMMA) spheres, which was infiltrated by a solution made from 2 g of Ce $Cl_3.7H_2O$ in 2.5 g of methanol. After 4 h of infiltration, the sphere and the solidified mixture were dried in air at room temperature for 24 h, and calcined by heating from room temperature to 583 K. It was held at 583 K for 2 h and heated to 723 K and held at the temperature for another 2 h. After the heat treatment, the polymer spheres were removed and the inverse opal ceria structure was formed. The resulting nano-porous ceria was ground to a powder and crushed to fine sizes. SEM images of 3DOM sample before and after thermochemical cycling were taken using Hitachi S4700 Scanning Electron Microscope. The powder was placed on a rectangular piece of carbon tape and coated with 10 nm Gold-Palladium coating using a sputter coater. Images were obtained at several magnifications. SEM images of ceria nano-structures are shown in Fig. 4.1.2.

Resulting ceria structures had a macropore diameter of 485 $\pm$ 20 nm. The characteristic size of the interconnecting window was 14 nm. Once the ceria powder was synthesized, it was packed in a sample holder. The geometry and dimensions of the sample holder are shown in Fig. 4.4. The sample holder was made of removable metal plates that were painted with Krylon-flat black spray paint in order to minimize reflections from the metal holder. The plates were sandwiched between two-transparent UV-fused silica windows and taped with black carbon tape. Any number of plates can be added or removed to the sandwich to allow for measurements with different "sample" thicknesses. Figure 4.4 shows the dimensions of the sample holder when one plate is sandwiched between the windows. The powder was packed in the sample holder in a dense packing. The mass of the ceria powder was measured prior to measurement, and based on the volume of the sample, and density of bulk ceria, the porosity of the

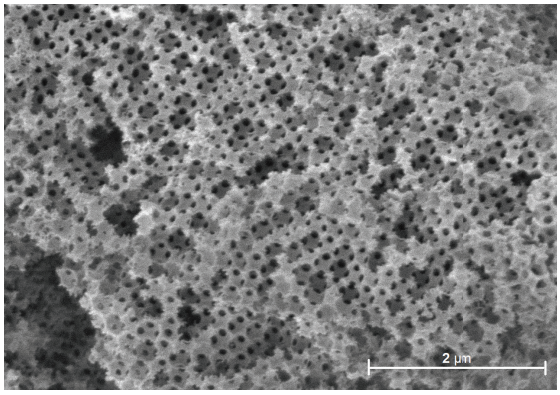

(a)

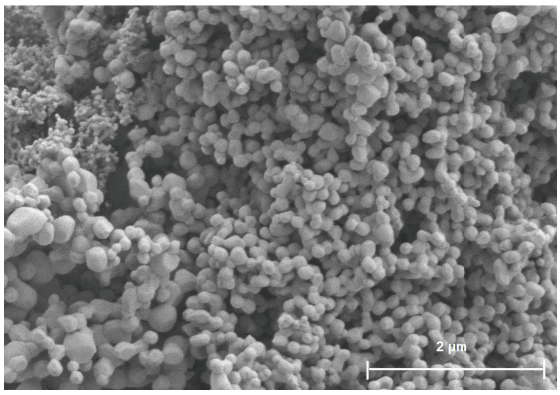

(b)

(c)

Figure 4.3: SEM images of the 3DOM ceria sample (a) before thermochemical cycling (b) after thermochemical cycling (c) photograph of the sample before (left, yellow) after cycling (right, white)

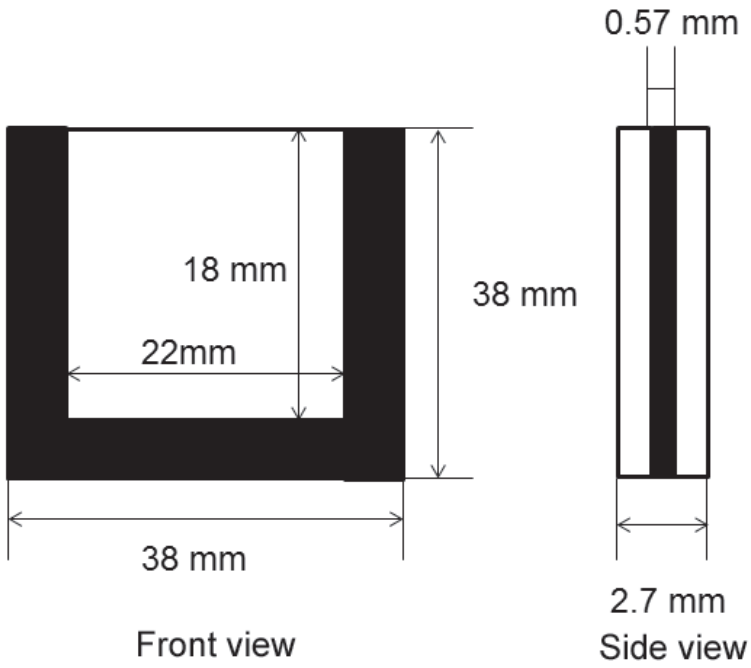

Figure 4.4: Schematic of the sample holder used for packing 3DOM ceria powder

packed bed was determined. Resulting bed porosity was 0.9 $\pm$ 0.05. High porosity of the packed bed despite a dense packing of the powder was as a result of the high porosity of the 3DOM structure, of 0.72 $\pm$ 0.02, estimated from geometry of the 3DOM structure. The resulting geometry for radiative transfer measurements was 22 mm x 18 mm rectangular cross-section and thickness of the samples 0.57 mm, 1.19 mm and 1.81 mm.

3DOM ceria prepared using the method described above was also cycled in a thermochemical reactor. 0.5 g of ceria underwent 60 thermochemical cycles between a temperature of 1100 °C for 1 minute, and 800 °C for 2 minutes. After the material underwent cycling, it was sieved using meshes resulting in a powder size between 180 μm and 800 μm. An SEM image of ceria that underwent thermochemical cycling is shown

in Fig. 4.3(b). It was then packed in a sample holder resulting in sample thickness of 0.57 mm with a cross-section of 22 mm x 18 mm, and a bed porosity of 0.83 ± 0.04.

4.1.3 Ceria thin film by pulsed laser deposition

Optical characterization of non-scattering crystalline ceria of 0 % porosity was performed. A ceria thin film fabricated by California Institute of Technology was employed. The thin film was deposited on a Yttria Stabilized Zirconia ($Yr_{0.16}Z_{0.84}O_{1.92}$, YSZ) substrate by pulsed laser deposition (PLD). A coherent KrF 248 nm excimer laser was used at a deposition frequency of 20Hz and power density of 2 J/cm^2. Ceria (Sigma Aldrich 202975, 99.995 % pure) was deposited on the substrate maintained at a temperature of 650 °C. Background pressure of oxygen was 5 mTorr and the resulting film porosity was close to 0 %. Post-annealing occured at oxygen pressure of 100 Torr for 20 min and the film was polished on both sides. The cross-section of the sample was of 1 cm $\times$ 1 cm. The thickness of the substrate was 0.5 mm and thickness of the film was 2 μm.

4.2 Optical characterization of ceria

Optical characterization of materials typically involve measurement of the transmission spectrum of a thin, non-scattering, absorbing, reflecting and refracting film with film thickness much smaller than the width and length of the film. Other approaches include ellipsometric measurements of real and imaginary part of the dielectric function of the material. The goal of optical characterization is to obtain qualitative information about absorption bands in the material, i.e. wavelengths at which incident radiation is completely absorbed, and to infer the complex refractive index of the material.

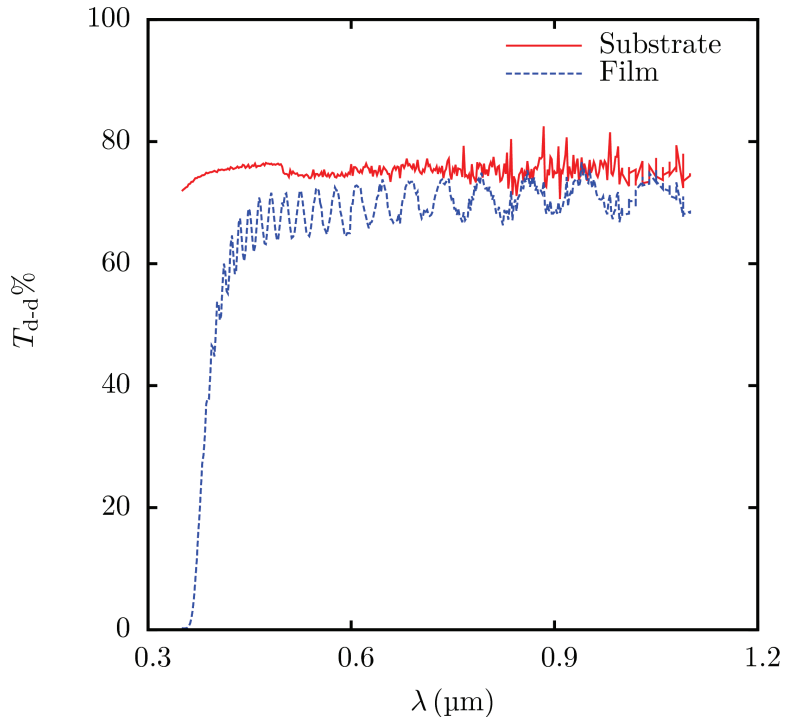

Figure 4.5: Transmittance of ceria thin film deposited on YSZ substrate, and blank YSZ substrate

4.2.1 Transmission spectrum of non-scattering ceria sample

Transmittance of the ceria thin film deposited on a YSZ substrate was measured by using the bi-normal transmittance setup (Fig. 3.2) at 0.002 μm intervals. The spectral scan interval was controlled by adjusting the slits of the monochromators. A smaller slit width of 320 μm facilitated higher spectral resolution. Measurements were repeated for ten trials, and transmittance was averaged over the experimental trials. Measured transmittance is shown in Fig. 4.4 for the blank substrate (without any ceria film deposited) and thin film of ceria of thickness 2 μm deposited on the substrate.

The transmittance spectrum for the ceria thin film indicates an absorption band

present below a wavelength of 0.5 μm where incident radiation is strongly absorbed and transmittance approaches zero. Recall that the thin film is a non-scattering sample, and attenuation of the incident radiation within the film is by absorption. Between wavelengths of 0.4 – 0.5 μm, transmittance shows a gradual increase, reaching an almost constant mean value after about 0.5 μm. After a wavelength of 0.5 μm, periodic oscillations in the transmission spectrum occur. Oscillations of this nature are characteristic when thickness of the film is comparable to the radiation wavelength (Born and Wolf, 1999). The oscillations are as a result of interference. For a wave incident normally and traveling through the film with thickness h and refractive index n, the phase difference for a period of oscillation corresponding to 2π is given by:

$$\frac{\delta}{2\pi} = \frac{2nh}{\lambda} \tag{4.1}$$

where, δ is the phase difference. When this phase difference is equal to an integer, intensity maxima occur, as seen by the crests of oscillations in the transmittance spectrum. When the phase difference is equal to half-integer values, such as 1/2, 3/2, 5/2, etc., intensity minima occur. The period of oscillation τ can be related to the index of refraction, film thickness and radiation wavelength according to the following relation (Dombrovsky, 2012a):

$$\tau = \frac{\lambda^2}{2nh} \tag{4.2}$$

From the above equation, it can be seen that the oscillation period increases with wavelength for constant index of refraction, and this trend can be witnessed in the measured transmittance spectrum of the thin film as well. Fine oscillations are also present in the measured transmittance of the blank substrate. These oscillations are non-periodic and random in nature, and are attributable to measurement noise. The root-mean square value of the amplitude of the oscillation is about 5 % the mean value of transmittance. Ripple effect is a phenomenon that occurs in semi-transparent materials in the spectral

range corresponding to weak absorption and is often attributed to oscillations in absorption spectrum. However, there is no evidence that ripple effect is indeed responsible for the oscillation of the substrate (Bohren and Huffman, 1998).

One classic approach to describe the optical behavior of materials involves quantifying effects of electromagnetic wave propagation in materials, using the knowledge of material's electrical characteristics, specifically electrical permittivity and electrical conductivity. Absorption of energy from an electromagnetic wave in the thermal radiation spectrum by free and bound electrons occurs such that electrons are excited to another band. This phenomenon is particularly noticeable in non-conductors of electricity since, unlike metals (conductors) they do not have overlapping bands. Since non-conductors of electricity (such as ionic solids and crystals) typically have a large band gap between two adjacent bands, absorption of electromagnetic radiation occurs only when the incident radiation is of a frequency that is equal to or greater than the band gap. Studies indicate that ceria has a band gap of 3–4 eV, suggesting that electronic absorption occurs at electromagnetic radiation wavelengths up to 0.45 $\mu\mathrm{m}$ (Özer, 2001; Fangxin et al., 1997).

One of the outcomes from the transmittance spectra and eqs. (4.1) and (4.2) is that the index of refraction, n of semi-transparent thin films can be inferred by analyzing the period of oscillations and by casting the index of refraction as a Taylor series with the period of oscillation as the dependent variable. This results in a differential equation for n which can be solved to obtain spectral dependence of n (Dombrovsky, 2012a), or by using a fitting function (Oh et al., 2012). Many ionic solids such as metal oxides and ceramics fall in the range of semi-transparency in the UV-VIS-NIR spectrum, as they are characterized by optical band gaps 2–5 eV (Di Quarto et al., 1997).

4.2.2 Optical constants of ceria

Several studies have used UV-VIS-NIR spectroscopy or spectroscopic ellipsometry to infer index of refraction of ceria. Among notable articles are those that have reported optical constants of single crystal ceria by applying Kramers-Kronig relations [1] (Marabelli and Wachter, 1987) and that of polycrystalline ceria prepared by a variety of techniques such as chemical vapor deposition, electron/ion beam deposition (Patsalas et al., 2002; Barreca et al., 2003; Kanakaraju et al., 1997), pulsed laser deposition (Balakrishnan et al., 2011) and sol-gel deposition (Özer, 2001). Ab-initio calculations were also performed to obtain optical constants of ceria (Sun et al., 2010). As one would expect, there is considerable spread of data in the index of refraction and index of absorption due to changes in deposition condition, substrate temperature, method of deposition and structural characteristics.

Accurate determination of the index of absorption remains a challenge, because of the behavior of index of absorption with wavelength. All studies cited here report a consistently decreasing index of absorption after a wavelength of approximately 0.45 $\mu\mathrm{m}$. In the spectral range of weak absorption, because of low values of k, it cannot be reliably retrieved from fitting functions applied to transmittance or reflectance spectra. Further, transmittance cannot be used to retrieve index of absorption corresponding to the spectral range of strong absorption (i.e. the UV and the short-wave part of the visible spectrum, below a wavelength of 0.45 $\mu\mathrm{m}$). This is not surprising, because the optical constants are typically obtained by measuring transmittance and reflectance of a non-scattering crystalline sample such as the thin film of ceria shown in fig. 4.4, and by using theoretical relations, such as Kramers-Kronig analysis or by interferometry

[1] Kramers-Kronig relations can be applied to any complex function to retrieve the real part of a complex from imaginary part or vice-versa.

applied to transmittance spectra or Kubelka-Munk function applied to reflectance spectra. If one were to observe the transmittance spectrum of non-scattering ceria, it can be seen due to strong absorption (indicating large value of index of absorption) attenuation of the incident radiation is strong, and transmittance is extremely low, corresponding to noise levels in the measurement. In the spectral band where absorption is weak, transmittance is indeed high, but accurate determination of the low index of absorption is challenging, because values of index of absorption may approach values as low as 10^{-3}. Identifying the small but non-zero index of absorption, and consequently, absorption coefficient is also important to estimate the heating rates of re-emitted infrared radiation, and it is inaccurate to assume that the material is non-absorbing in the spectral range of weak absorption. Thus, significant difficulties in identifying radiative properties of ceria ceramics are anticipated because of low value of directional-hemispherical transmittance of optically thick media and unknown index of absorption in the spectral range 0.5–2 μm.

For the samples used in the present work, index of refraction and absorption of polycrystalline ceria from Patsalas et al. (Patsalas et al., 2002) deposited at a substrate temperature of 950 °C were found to be representative (Oh, 2010). Optical constants of ceria obtained by Patsalas et al. are shown in Fig. 4.6. Refractive index of ceria remains a constant in the spectral range $\lambda > 0.5$ μm and this trend is consistent with the data reported in the literature cited in this section. Index of absorption reaches small values, close to zero after a wavelength of about $\lambda > 0.45$ μm, providing physical basis to the transmittance of the ceria thin film shown in Fig. 4.5. Because of the uncertainty in determination of index of absorption, some challenges in identification of radiative properties of sintered ceria ceramics are anticipated. Powders are typically considered non-reflecting or refracting media and the identification of radiative properties of 3DOM ceria may not be affected by the unknown index of absorption.

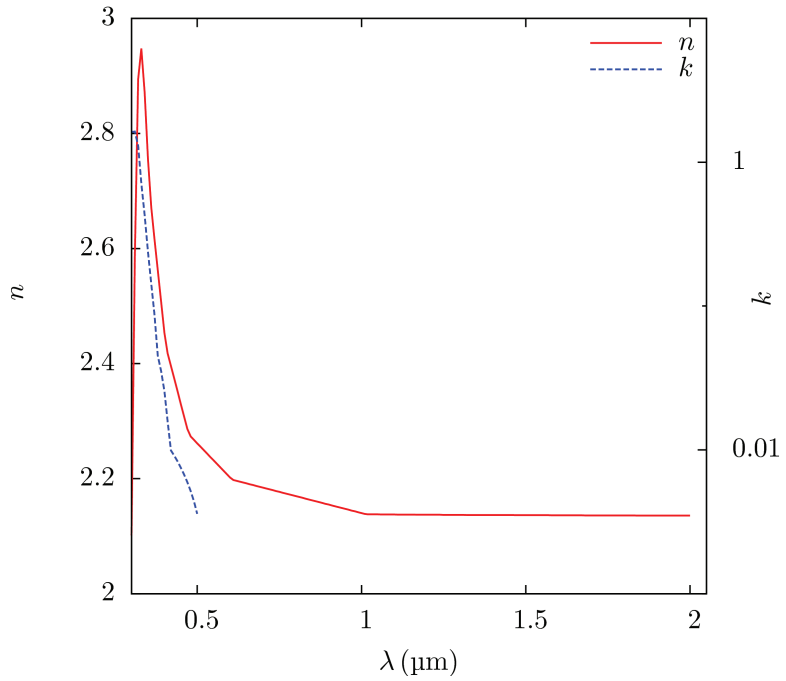

Figure 4.6: Optical constants of polycrystalline ceria. Data taken from (Patsalas et al., 2002)

4.3 Summary

This chapter presents morphological and optical characterization of ceria, and a short discussion on fabrication techniques employed to synthesize the samples used in the present work. A review of studies reporting optical constants of ceria is also presented. Establishing the dependence of radiative properties on morphology is one of the goals of the present work. Thus, samples of selected morphologies were chosen to facilitate meaningful comparison between samples of differing pore-structure, pore and grain size and porosity, while bearing in mind that samples that are only representative of those that will be used in actual solar-thermochemical reactors are studied. SEM characterization was used to investigate morphological features of the samples. Optical

properties of ceria as reported in the literature were reviewed and were found to depend on structure, preparation technique, substrate temperature etc. Representative values of optical constants of ceria were selected for inverse analysis to determine radiative properties of the selected morphologies. Index of absorption is unknown in the spectral range, 0.5–2 μm.

Chapter 5

Experimental characterization at ambient temperature

This chapter presents experimental radiative characterization of ceria ceramics in the UV-VIS-NIR spectral range. While complete radiative characterization of any material typically involves determination of spectral radiative properties as a function of wavelength, temperature and morphology, the objective of the present chapter is to draw qualitative conclusions about the scattering and absorption characteristics of the material based on experimental data, and observe trends in experimental data, namely, measured bi-normal transmittance, normal-hemispherical transmittance and reflectance as functions of wavelength and morphology. Statistical uncertainty in measurements is documented in Appendix D. In Chapters 5 and 6, the spectral subscript λ is omitted from symbols for brevity.

5.1 Bi-normal transmittance

5.1.1 Sintered ceria discs

Figure 5.1 shows the bi-normal transmittance $T_{\text{d-d}}$, of dense ceria samples of porosity $p_1 = 0.08$, and sample thickness $L = 0.76, 1.22, 1.40$ and 1.88 mm in the spectral range 0.3–1.7 μm measured at a spectral scan interval of 0.01 μm. Figure 5.2 shows the bi-normal transmittance of porous ceria samples of porosity $p_2 = 0.72$, and sample thickness $L = 0.61, 0.71, 1.02, 1.47$ and 1.92 mm in the same spectral range. Measurements were averaged over 25 experimental trials for each wavelength and sample thickness, and the average transmittance is shown in these figures. Statistical uncertainty in bi-normal transmittance is on the order of 5 % in the spectral range 0.5–1.7 μm. Each data point was integrated over a time of 0.3 s to ensure stable (non-transient) signals. Details of uncertainty estimation are available in Appendix D. Other sources of experimental error that are more difficult to quantify also exist in the measurements, and these include variability due to positioning of the sample, micro-structural defects in the sample such as fractured grains clogging the pores etc. As a result, the error in bi-normal transmittance is conservatively estimated to be 10 % for the dense samples and 15 % for the porous samples.

For both the dense and porous samples, as expected, the transmittance increases with decreasing thickness, and this trend is more pronounced for the dense samples. The transmittance of the dense samples increases on average with wavelength in the spectral range $0.5 \leq \lambda \leq 1.7$ μm, while the transmittance of the porous samples remains approximately constant. Recall that the dense sample measurements are more representative of the bulk material because of the lower porosity (close to 0 %) of the dense samples. If one were to recall from Figure 4.1.1, the transmittance spectra of thin film of (crystalline) bulk ceria, the index of absorption decreases in this spectral

range [(Patsalas et al., 2002; Sun et al., 2010)]. Thus, the increasing transmittance of both types of samples is attributable to decreasing index of absorption in this range. It can also be seen from Fig. 5.1 and 5.2 that the porous samples attenuate the incoming radiation stronger than the dense samples for comparable sample thicknesses in the spectral range 0.6–1.7 μm. Absorption due to bulk material does not contribute strongly to attenuation of incoming radiation in this spectral range. Thus, it is hypothesized that this effect is as a result of intense scattering that occurs in the porous samples. Weaker scattering in the dense ceramics at radiation wavelengths approaching the pore size of the dense ceramics is one possible physical cause for the increase in transmittance at higher wavelengths[1] .

Localized fluctuations of transmittance are observed at the same wavelengths for both sample types. Additional measurements with different time constants were performed to ensure the experimental results were converged, i.e. the localized fluctuations were repeatable and were not a result of instrumentation artifacts. Interference and ripple structure that occur at large wavelengths and when absorption is weak may also introduce such fluctuations in the transmittance spectra [as discussed in (Bohren and Huffman, 1998)]. The transmittance spectra of dense samples also show a sharp peak at about 0.9 μm. Additional measurements were performed to ensure that the peak in transmittance was repeatable. At about 1.0 μm the monochromator switches to a grating that is sensitive in the spectral range 1.0–1.4 μm. It is hypothesized that when radiation wavelengths approach the limit of sensitivity a grating radiative power in the normal direction is weak, especially for the signal measured without the sample, $\dot{Q}_{\mathrm{d}}^{0}$. For the signal measured with the sample, $\dot{Q}_{\mathrm{d}}$, multiple scattering events result in more uniform radiative intensity in all directions. As bi-normal transmittance is defined as

[1] Note that in the Rayleigh limit, scattering efficiency decreases inversely with wavelength, according to the relation $Q_{\mathrm{sca}} \sim \lambda^{-4}$.

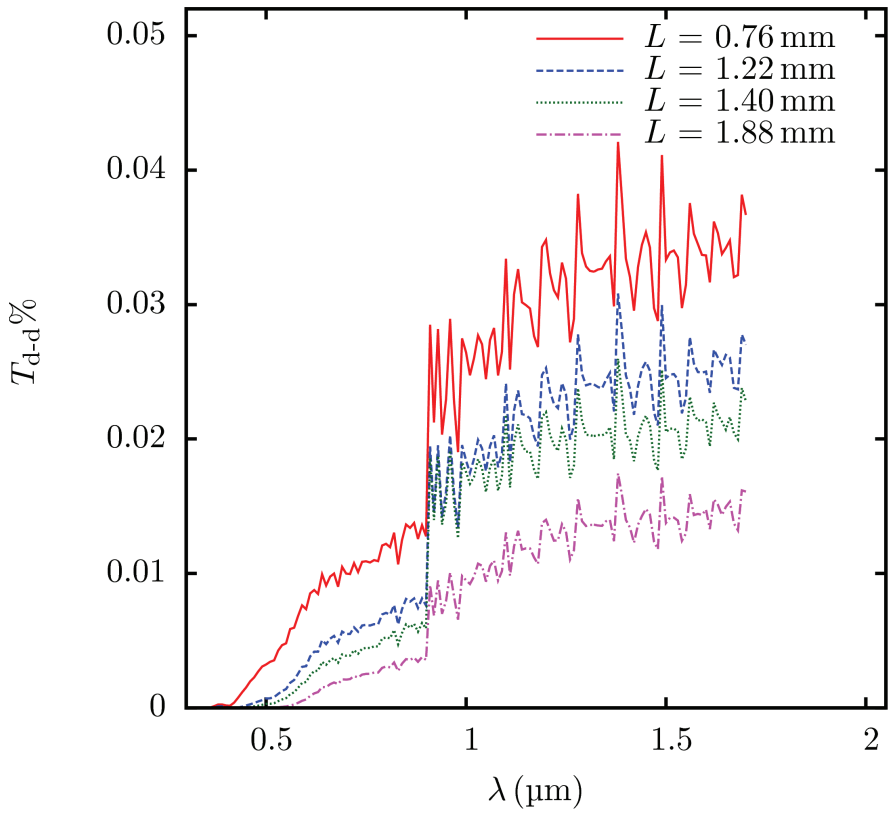

Figure 5.1: Bi-normal transmittance ($T_{\text{d-d}}$) of sintered ceria discs of porosity 0.08 and different sample thicknesses

the ratio of signal measured with the sample to one without, a step change in transmittance is observed when grating change occurs. The sharp increase in transmittance is not observed in the transmittance spectra of porous ceramics, also suggesting that the porous ceramics may scatter the incoming radiation strongly, especially in the forward direction, leading to nearly constant bi-normal transmittance.

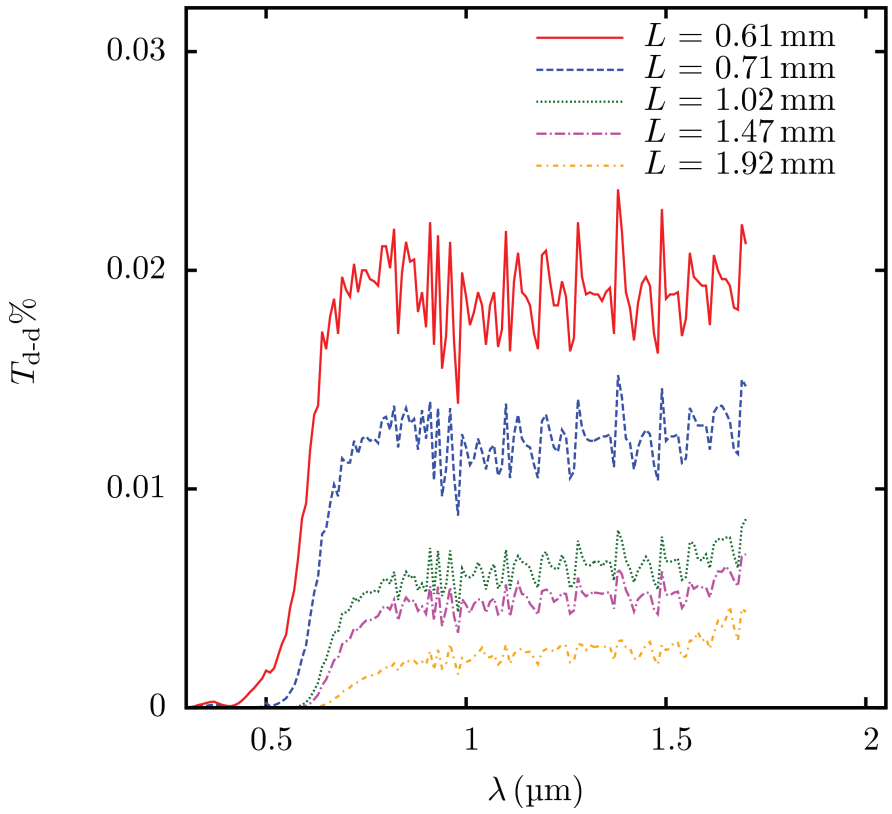

Figure 5.2: Bi-normal transmittance ($T_{\text{d-d}}$) of sintered ceria discs of porosity 0.72 and different sample thicknesses

5.1.2 3DOM ceria packed bed

Bi-normal transmittance of 3DOM ceria packed bed was measured using the in-house UV-VIS-NIR spectroscopy setup. 3DOM ceria in powder form was packed into a packed bed arrangement in a rectangular sample holder, which essentially consists of two transparent fused-UV silica windows enclosing U-shaped metal plates filled with the ceria powder. The mass of the packed bed was measured prior to transmittance measurements, and based on the mass of the samples and their volume, and the density of bulk ceria, the porosity of the packed bed was measured. The porosity of the packed bed was 0.9 ± 0.05. This overall porosity of the packed bed is due to the high porosity of the nano-pore structure of the 3DOM powder, of about 0.72. The packed bed was stirred to ensure that the packing was random, and measurement area was representative of the entire sample.

Figure 5.3 shows the bi-normal transmittance $T_{\text{d-d}}$, of 3DOM ceria samples of thickness $L = 0.57, 1.19$ and 1.81 mm in the spectral range 0.3–1.1 μm measured at a spectral scan interval of 0.01 μm. The uncertainty in the measurements is estimated to be 10 % in the spectral range 0.6–1.1 μm. Figure 5.4 shows a comparison of bi-normal transmittance of packed bed of 3DOM ceria and sintered ceria discs of comparable thickness. The magnitude of bi-normal transmittance is nearly two orders of magnitude above those of the sintered discs in the spectral range $\lambda \geq 0.6\ \mu\text{m}$. It must be noted that absorption by bulk ceria is extremely small in this region, and attenuation is primarily by scattering. Increased transmittance of the 3DOM ceria packed bed indicates weaker scattering by the packed bed than the sintered ceria discs in this spectral range.

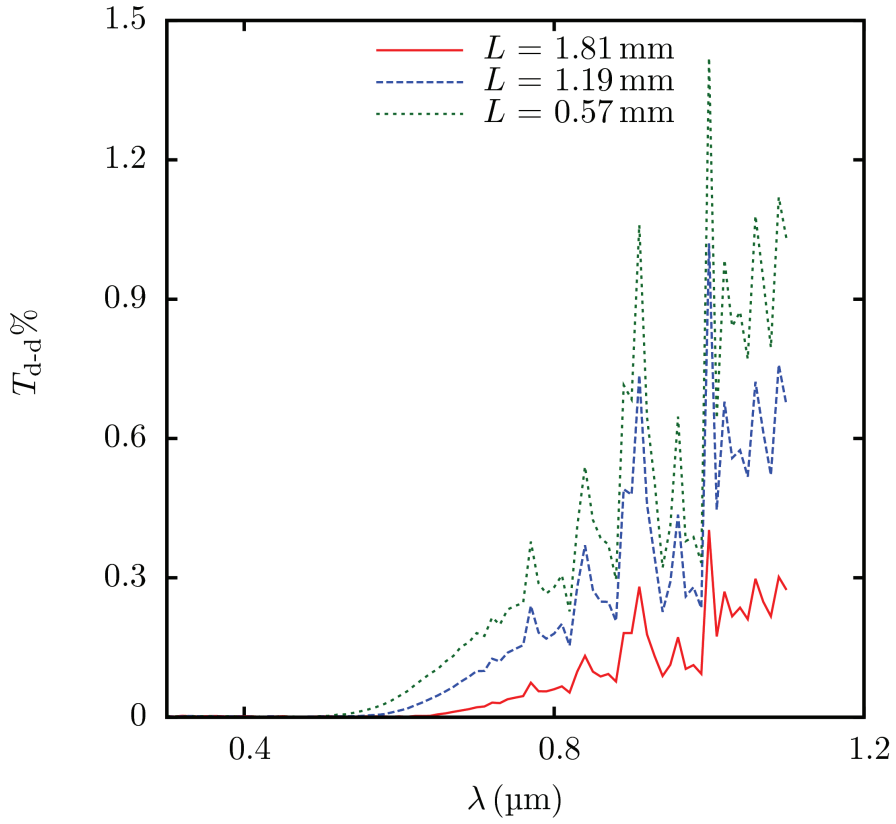

Figure 5.3: Bi-normal transmittance ($T_{\text{d-d}}$) of packed bed of 3DOM ceria of porosity 0.9 and different sample thicknesses

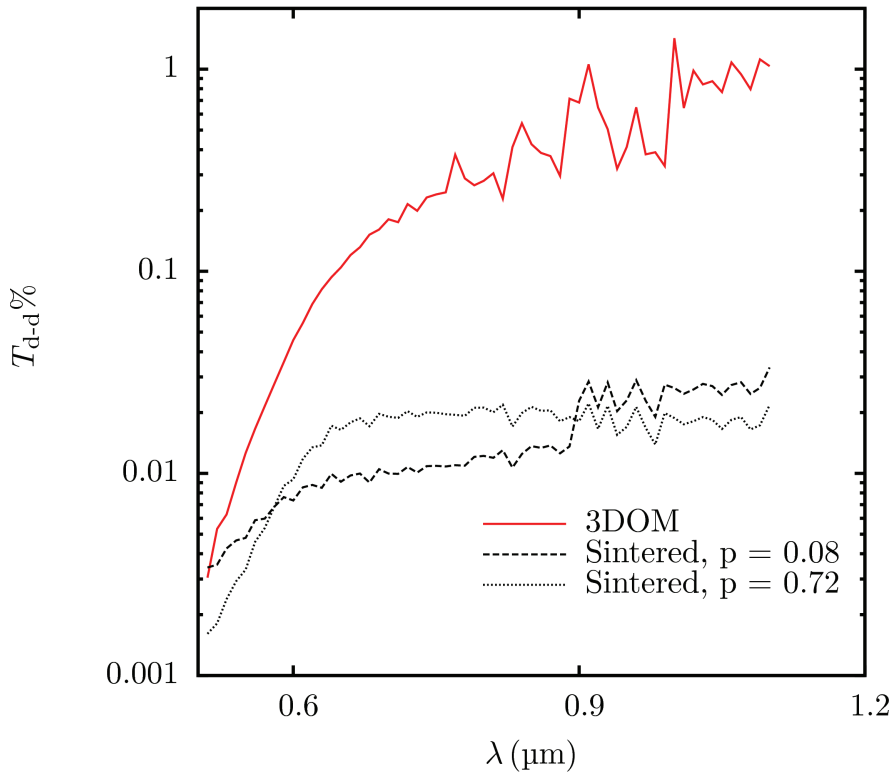

Figure 5.4: A comparison of bi-normal transmittance ($T_{\text{d-d}}$) of packed bed of 3DOM ceria and sintered ceria discs of thickness 0.57 mm

5.2 Normal-hemispherical transmittance and reflectance

5.2.1 Sintered ceria discs

Figure 5.5 shows normal-hemispherical reflectance of sintered ceria ceramics measured in the wavelength range 0.35–2 μm for dense samples of thickness $L = 0.76, 1.22$ and 1.88 mm. The error in reflectance measurements is $\pm$ 4 % at all wavelengths. The spectral scan interval for the reflectance measurements was 0.005 μm. The reflectance at each wavelength was averaged over 5 data points and integrated over 2 s interval. Experimental error in normal-hemispherical reflectance is very high over a narrow spectral range, 0.83–0.95 μm because of grating and detector changes in the spectrophotometer. As a result, data-points in this narrow spectrum are omitted in Figs. 5.5 and 5.6. As anticipated, in the spectral range 0.9–2 μm, normal-hemispherical reflectance is very high due to intense scattering. Reflectance is also only weakly dependent on the wavelength in this spectral range and remains nearly constant. Figure 5.6 shows the normal-hemispherical reflectance of sintered ceria discs measured in the wavelength range 0.35–2 μm for porous samples of thickness $L = 0.71, 1.12$ and 1.92 mm. It can be seen from these two figures that the reflectance of the porous samples is of the same order as that of the dense samples at a given wavelength, and for comparable thicknesses, indicating a weak effect of porosity in reflectance.

Normal-hemispherical reflectance is indicative of volumetric scattering of the material, in addition to the interface reflectivity. To illustrate this idea, one can imagine the material to be made of many scatterers dispersed in a host medium. The scatterers can be pores of the dense ceramics dispersed in bulk ceria, or grains of the porous ceramics dispersed in air. When a ray is incident on the medium and encounters a scatterer, it is either absorbed or scattered, based on the material's optical characteristics. If the

scattering albedo of the material is high, rays incident on the scatterers are mostly scattered. Additionally, if a medium were to have large optical thickness, or large extinction coefficient, rays only enter and interact few short distances in the medium before getting attenuated. To illustrate this idea even further, one can consider a medium that is isotropically scattering, so that half the scattered intensity is in the backward direction, and half is in the forward direction after the first scattering event. Of the fraction that is scattered in the forward direction, half of the fraction will be in the forward and the remaining half in the backward direction at the second scattering event and so on. Ultimately, the rays only interact a short distance within the medium because of its large optical thickness, are reflected back into the surroundings, and only a small fraction is transmitted. Based on high values of normal-hemispherical reflectance, as well as the small values of transmittance, it is expected that scattering is dominant and the value of scattering albedo is close to unity for the sintered ceria discs samples.

5.2.2 3DOM ceria packed bed

Normal-hemispherical transmittance and reflectance were measured in the spectral range 0.35–2.2 μm at a spectral scan interval of 0.005 μm for the packed bed of 3DOM ceria samples of thickness $L = 0.57, 1.19$ and 1.81 mm. These are shown respectively, in Fig. 5.7 and 5.8. The statistical uncertainty in normal-hemispherical transmittance in the spectral range 0.6–2.2 μm is estimated to be 5 % for the samples of thickness 0.57 mm and 1.19 mm, and 10 % for the thickest sample. The statistical uncertainty in normal-hemispherical reflectance is estimated to be 1 % for all samples in the spectral range 0.35–2.2 μm. The spectral trend of normal-hemispherical reflectance is comparable to that of the sintered ceria discs till a wavelength of 0.5 μm. This is because in this spectral range, attenuation is primarily by absorption and the index of absorption decreases with wavelength. After a wavelength of 0.6 μm, the samples are more

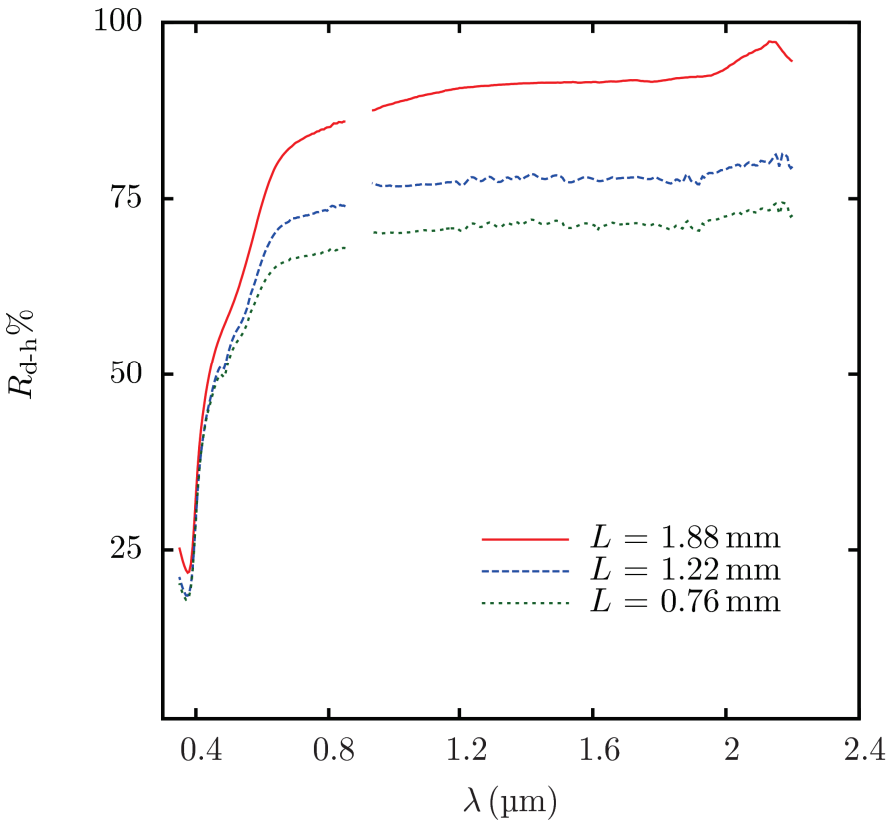

Figure 5.5: Normal hemispherical reflectance ($R_{\text{d-h}}$) of sintered ceria discs of different thicknesses and porosity 0.08

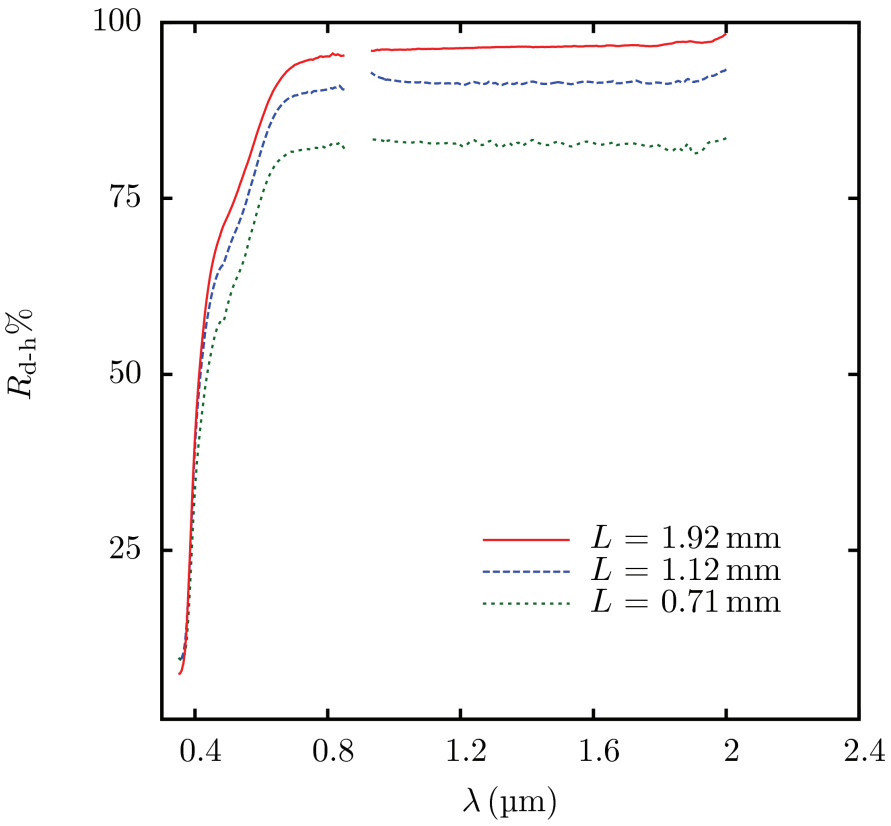

Figure 5.6: Normal hemispherical reflectance ($R_{\text{d-h}}$) of sintered ceria discs of different thicknesses and porosity 0.72

transparent to incident radiation due to weaker absorption in this spectral range as witnessed by the higher values of normal-hemispherical transmittance. However, normal-hemispherical reflectance decreases with wavelength in the spectral range $1 \leq \lambda \leq 2.2$ μm , indicating that the 3DOM ceria packed bed does not attenuate the incoming radiation by scattering as strongly as the sintered ceria discs. Both normal-hemispherical transmittance and reflectance show a local minimum at a wavelength of about 1.4 μm, and 2 μm. Both these minima are directly as a result of strong absorption of incident radiation by the transparent windows made of UV-fused silica. Additionally, water vapor in the pores of the sample may contribute to absorption of incident radiation at a wavelength of 2 μm.

In addition to pure 3DOM ceria, normal-hemispherical transmittance and reflectance of 3DOM ceria, cycled in a thermochemical reactor were measured to observe the effects of morphology on radiative properties. Normal-hemispherical transmittance and reflectance of 3DOM ceria packed bed with and without thermochemical cycling are shown in Fig. 5.10. A comparison of normal-hemispherical reflectance of 3DOM ceria packed bed of 0.57 mm with and without thermochemical cycling, and sintered ceria ceramics of sample thickness 0.76 mm and 0.61 mm for the dense and porous sample is shown in Fig. 5.11. The normal-hemispherical reflectance of the sample that underwent thermochemical cycling is higher than that of the sample that did not undergo thermochemical cycling in the spectral range $0.8 \leq \lambda \leq 2.2$ μm. A higher value of normal-hemispherical reflectance implies stronger scattering, hinting that the 3DOM ceria sample that underwent thermochemical cycling scatters the incoming radiation more strongly than the sample that did not undergo thermochemical cycling. The spectral trend of normal-hemispherical reflectance of the sample that underwent thermochemical cycling resembles that of the sintered ceria discs. Normal-hemispherical transmittance reaches low values on the order of 5 %. Comparing the SEM images

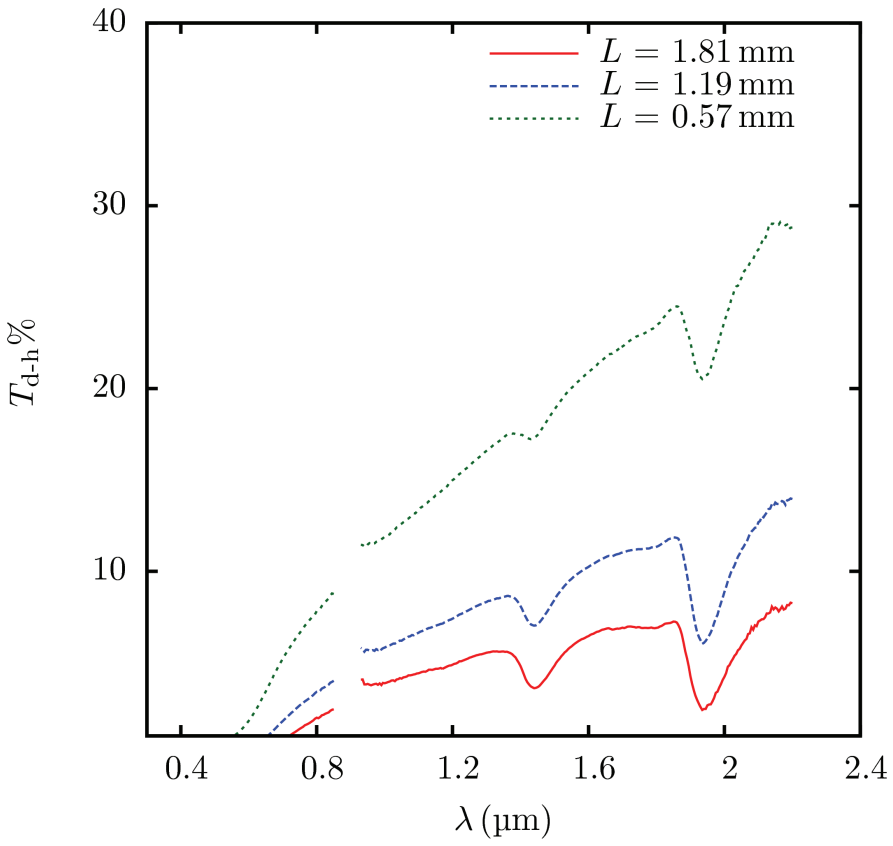

Figure 5.7: Normal hemispherical transmittance ($T_{\text{d-h}}$) of 3DOM ceria packed bed of different thicknesses and porosity 0.72

of the 3DOM ceria sample without and with thermochemical cycling, Figs. 4.3(a) and 4.3(c), and that of sintered discs of ceria of porosity, $p_1 = 0.08$, Fig. 4.1(a) and 0.72, Fig. 4.2(a), it is evident that sintering occurs in the walls of the 3DOM structure that underwent thermochemical cycling, which completely altered its scattering characteristics in the spectral range $0.8 \leq \lambda \leq 2.2\ \mu\text{m}$.

From a physical standpoint, one would expect the absorption characteristics of the material to only depend on the mass of the material, or the amount of bulk material

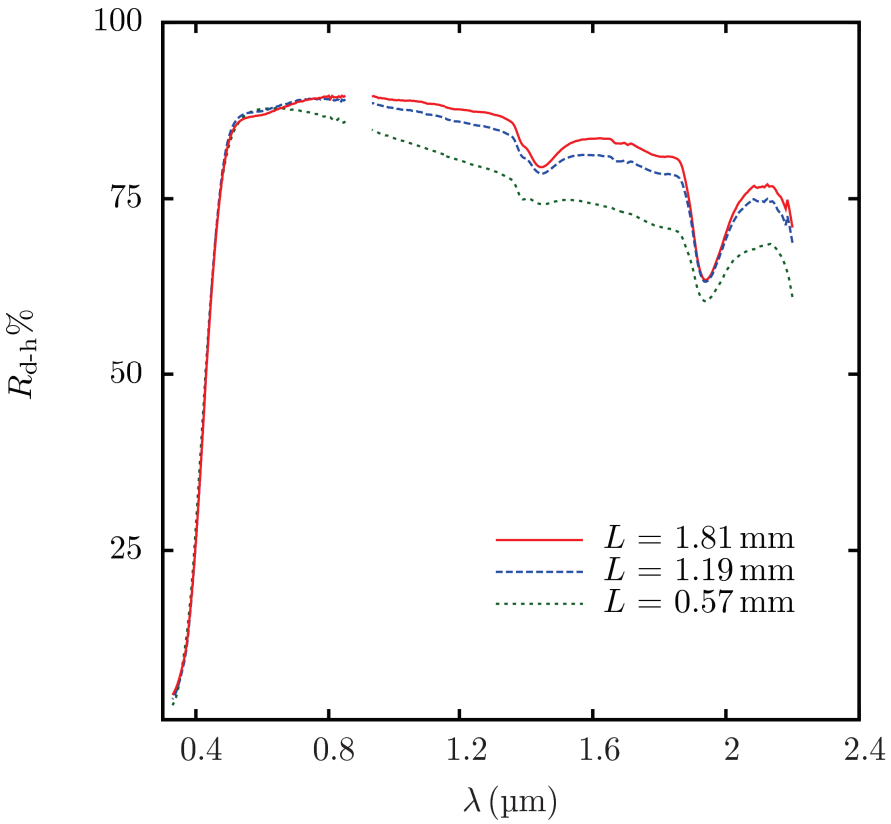

Figure 5.8: Normal hemispherical reflectance ($R_{\text{d-h}}$) of 3DOM ceria packed bed of different thicknesses and porosity 0.72

per unit volume available in the sample. Scattering characteristics, by contrast, depend on the morphological features of the material, such as pore size, pore distribution and arrangement etc. Comparing the normal-hemispherical measurements of two different structures of ceria ceramics, one can indeed verify these physical arguments experimentally. In the spectral range corresponding to strong absorption, $0.35 \leq \lambda \leq 0.5$ μm, measured radiative quantities, namely, transmittance and reflectance of two types of ceria structures, namely, sintered ceria discs of porosity 0.08 and 0.72, and 3DOM ceria packed bed of ceria of porosity 0.9, are independent of structure and morphology.

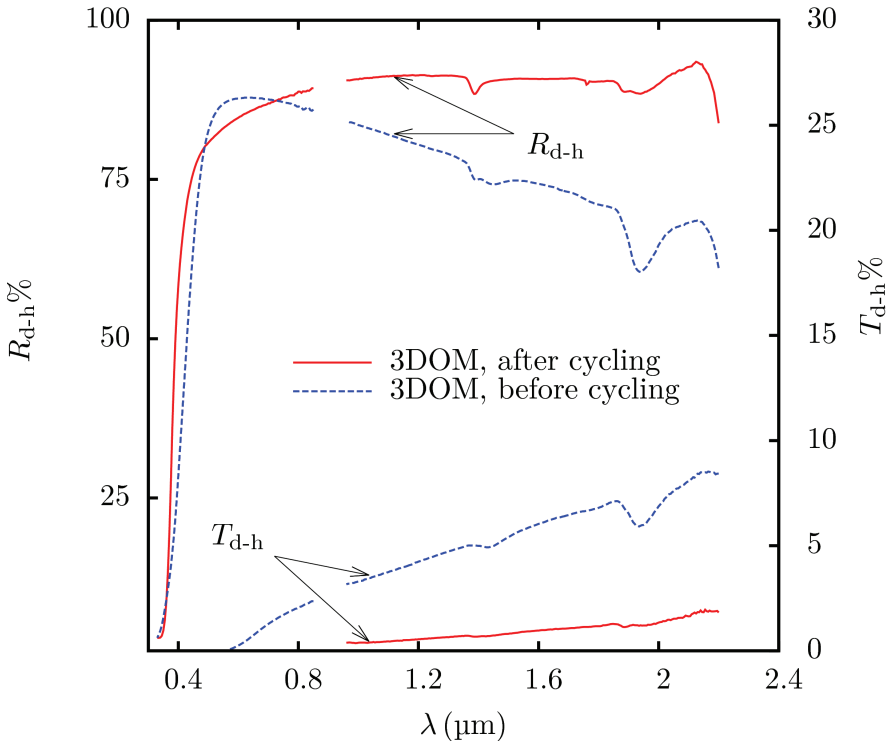

Figure 5.9: Normal hemispherical transmittance ($T_{\text{d-h}}$) and reflectance ($R_{\text{d-h}}$) of 3DOM ceria packed bed with and without thermochemical cycling of sample thickness 0.57 mm

This is particularly noticeable in figs. 5.10 and 5.11. In the spectral range of weak-absorption, where attenuation is primarily by scattering, transmittance and reflectance are strongly dependent on morphology and only weakly dependent on porosity (or the mass of the bulk material).

5.3 Summary of experimental results

Qualitative insights on the absorption and scattering characteristics of ceria and the effects of wavelength and morphology can be gained from experimental findings reported

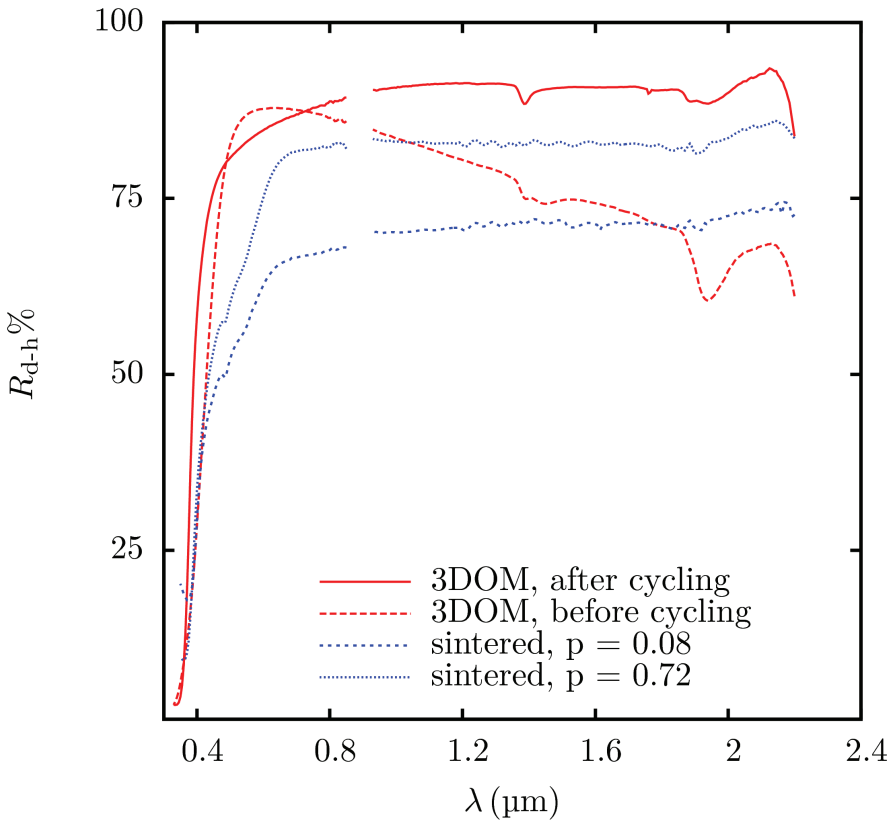

Figure 5.10: Normal hemispherical reflectance ($R_{\text{d-h}}$) of 3DOM ceria packed bed with and without thermochemical cycling of sample thickness 0.57 mm, and sintered ceria discs of comparable thickness.

in this chapter:

1) Ceria absorbs strongly in the short-wave portion of the spectrum, up to a wavelength of $\lambda = 0.5\,\mu\text{m}$. After this wavelength, ceria is more transparent to incident radiation, and transmittance is higher in the longer-wave and NIR wavelength, up to a wavelength of about $\lambda = 2.0\,\mu\text{m}$.

2) Absorption characteristics are dependent only on the mass of the bulk material present per unit volume, i.e. the porosity of the material. However, even a material

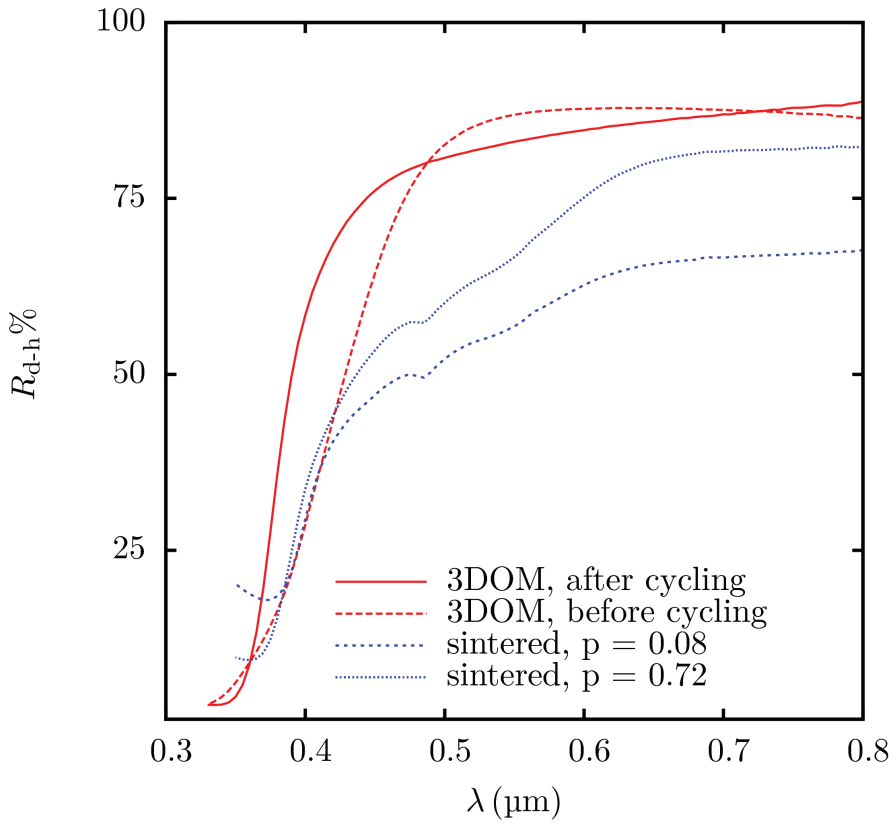

Figure 5.11: Normal hemispherical transmittance ($T_{\text{d-h}}$) and reflectance ($R_{\text{d-h}}$) of 3DOM ceria packed bed with and without thermochemical cycling

with 0.72 porosity shows strong absorption resulting in extremely low values of transmittance.

3) Scattering is very strong in the range of weak absorption, $0.5 \leq \lambda \leq 2$ µm for the sintered discs of ceria. Scattering characteristics, as quantified by normal-hemispherical reflectance is weakly dependent on wavelength and porosity in this spectral range.

4) Scattering is strongly dependent on pore structure and geometry, as well arrangement of pores. Normal-hemispherical reflectance for 3DOM packed bed and sintered

discs were sharply different in the spectral range where absorption is weak and scattering is strong.

5) Thermochemical cycling altered the structural characteristics of 3DOM ceria, causing grain growth and making the structure resemble sintered discs. This effect altered the scattering characteristics of ceria causing the normal-hemispherical reflectance to resemble that sintered discs of similar porosity. Classical electromagnetic theory predicts that scattering increases with the size of the particle, and the higher normal-hemispherical reflectance from samples that underwent thermochemical cycling and concomitant grain growth is consistent with the theoretical predictions.

Quantitative characterization of radiative properties involve a combination of inverse analysis and theoretical models to infer absorption and scattering coefficient, which is the focus of the next chapter.

Chapter 6

Identification of spectral radiative properties of ceria morphologies

6.1 Methodology

Determination of the complete set of radiative properties, namely, absorption and scattering coefficients and scattering phase function requires measurement of bi-directional intensity measurements with good angular resolution. While measurement of radiative intensity at angles near the forward direction are easier to achieve with a goniometry system, radiative intensity at angles near the backward direction are difficult to achieve due to experimental limitations such as being able to position the detector at an angle closer to the angle of the incident beam, as well as losses in optical collection systems. Further, many disperse materials in the Mie scattering regime scatter strongly in the forward direction, as a result of which, the intensity in the backward direction is low. Even if such angle-resolved radiative intensity were to be measured, using an appropriate numerical technique to obtain full set of radiative properties is only possible for idealized materials such as a regular array of spheres because of the computational cost involved

in inverting experimental data at every direction. Hence, identification of scattering phase function for engineering ceramics remains a challenge. A few researchers have been able to obtain approximate phase function based on bi-directional measurements at selected angles (Nicolau et al., 1994; Baillis et al., 2002; Hespel et al., 2003; Baillis et al., 2004; Lipiński et al., 2008; Coray et al., 2010). For engineering ceramics, it has been suggested that application of transport approximation to identify "transport" radiative properties is computationally more efficient than the full set of radiative properties. Transport scattering coefficient and absorption coefficient are typically identified from directional-hemispherical transmittance and reflectance (Eldridge and Spuckler, 2008; Lallich et al., 2009; Dombrovsky and Baillis, 2010; Sacadura, 2011). One approach uses the modified two-flux approximation (Dombrovsky et al., 2005, 2006, 2007, 2010, 2011), and has been applied successfully to identify transport scattering coefficient and absorption coefficient of ceramics for engineering applications. Identified transport radiative properties have been shown to be suitable for engineering heat transfer analysis, such as those encountered in solar thermochemical reactors particularly because the radiative intensity is integrated over a hemisphere, which then serves as the radiative heat flux term for the overall conservation of energy in combined heat and mass transfer processes. From the perspective of design of solar thermochemical reactors, it is then sufficient to obtain only the transport radiative properties (Dombrovsky, 2012b).

Traditional methods employed in the literature for identification of optical properties of dispersed media often rely on: (1) accurate values of directional-hemispherical transmittance and reflectance, and (2) knowledge of complex index of refraction over the entire spectral range of identification. The findings of experimental study from the previous chapter hints that sintered ceria ceramics are weakly absorbing in wavelength range 0.5–2 μm. It is also anticipated that these ceramics are highly scattering in the near-infrared as seen from the low values of bi-normal and normal-hemispherical

transmittance as well as high value of normal-hemispherical reflectance. The use of commercial spectrometers to measure directional-hemispherical transmittance is challenging, due to their lack of adequate signal-to-noise characteristics to measure such low values of transmittance. It is also challenging to fabricate sintered discs that are extremely thin to decrease the optical thickness of the sample and consequently increase radiant energy transmitted by the sample and reaching the detector. Deposition of sample on a substrate facilitates the fabrication of extremely thin samples that are mechanically stable, but in order to analyze measured experimental data and to obtain macroscopic radiative properties, the sample length scale must be larger than that of the wavelength to apply geometrical optics analysis and neglect wave interference effects. Further, one of the goals of the present work is to provide radiative properties of ceria ceramics that will ultimately be used in the solar thermochemical reactor, and it is critical that the structure and morphology of the samples used for measurement resemble those of the materials that will be actually employed.

Additionally, analysis of experimental data to infer radiative properties requires knowledge of complex index of refraction over the entire spectral range of identification. While the index of refraction of ceria has been documented independently by several researchers, studies documenting the index of absorption do not show good agreement with each other, as reviewed in section 4.2.2.

To overcome these limitations, a methodology is developed to infer radiative properties of sintered ceramics from measurements. In the first step, an analytical solution based on the modified two-flux approximation and the Monte Carlo ray-tracing (MCRT) technique is used to identify transport radiative properties of ceria ceramics. In the first step, directional-hemispherical reflectance of optically thick samples of ceria is used in combination with a solution to the one-dimensional radiative transfer problem, applicable in the limits of large optical thickness. This step is employed to retrieve

transport scattering albedo from the measured directional-hemispherical reflectance. In the second step, bi-normal transmittance of ceria samples with different values of optical thickness is used to infer transport extinction coefficient. Recall that the in-house setup for measuring bi-normal transmittance was developed specifically to facilitate measurement of transmittance of highly attenuating media, in situations where commercial spectrometers do not have adequate dynamic range. Bi-normal transmittance is an inherently two-dimensional measurement technique because the samples are irradiated over a small spot and radiant energy leaving the sample is collected over a narrow cone angle from a small area of the sample. As a consequence, solutions applicable to one-dimensional radiative transfer problem cannot be applied to retrieve transport extinction coefficient from bi-normal transmittance measurement. The MCRT technique is employed to retrieve the transport scattering coefficient. The MCRT technique incurs high computational cost for optically thick and highly scattering media. Hence, simulations are not performed for a wider spectral range and the medium is assumed to be gray. Independent scattering is assumed and Mie scattering theory is applied to polydisperse pores and grains to extend the spectral range of identification. Mie scattering theory applied to polydisperse pores and grains requires size size distributions of pores and grains in the sample. However, for a sintered material, obtaining size distribution cannot be achieved using a particle size counter (similar to a powder), or image-based techniques, such as SEM or TEM, because of the three-dimensionality of the sample. Hence, size distribution of the pores and grains is estimated by matching the transport extinction coefficient identified by MCRT to that obtained using Mie theory in the spectral range for pores and grains of various size distributions. Average sizes of pores and grains predicted by the Mie theory analysis of the transport scattering coefficient are compared with available data for morphology of the samples of ceria ceramics to verify the applicability of Mie theory and independent scattering hypothesis to the

present problem. This approach was used for the sintered ceria discs. The methodology is applicable in situations where traditional identification procedure cannot be employed due to low and uncertain values of directional-hemispherical transmittance. The methodology is suitable for estimating radiative properties approximately, with accuracy that is acceptable for combined heat transfer problems such as modeling heat and mass transfer in solar thermochemical reactors.

For the samples where normal-hemispherical transmittance could be reliably measured, the identification process is fairly straightforward. An inverse technique, in this case, Monte Carlo ray-tracing is used, and transport scattering albedo and transport extinction coefficient are guessed until the transmittance and reflectance from MCRT matches experimental data. This approach was used for the 3DOM ceria powder. One of the limitations of Monte Carlo ray tracing technique is that in the spectral ranges where absorption of incident radiation by the material is strong, MCRT technique cannot be applied because of strong attenuation of incident radiation at distances comparable to radiation wavelengths. For ceria this typically occurs in the wavelength interval $0.3 – 0.5 \ \mu\mathrm{m}$.

Experimental data from the previous chapter were used for the identification of transport radiative properties. The Monte Carlo ray-tracing technique was developed by the author of this thesis. Both the analytical solution based on Modified two-flux approximation, and Mie theory calculations were performed by visiting researcher Leonid Dombrovsky.

6.2 Monte Carlo ray-tracing method

6.2.1 Background

Monte Carlo methods were developed to solve mathematical problems by statistical sampling and first used in the 1940s to model neutron diffusion in the Manhattan Project. Development of Monte Carlo methods to statistically solve a physical problem involves describing the physical system by a number of variables and cumulative distribution of the variables. Random numbers are generated and cumulative frequency distribution is employed to compute the probability that an event or a physical phenomenon can occur.

The frequency function of any phenomenon denoted by $f(x)$ has probability density function $g(x)$ given by:

$$g(x) = \frac{f(x)}{\int_{x_{min}}^{x_{max}} f(x)\mathrm{d}x} \tag{6.1a}$$

The probability density function gives the probability that any variable X belongs to $\mathrm{d}x$ around x:

$$\mathrm{d}P(x \leq X < x + \mathrm{d}x) = g(x)\mathrm{d}x \tag{6.1b}$$

The cumulative distribution function is given by:

$$F(x) = P(X < x) = \int_{x_{min}}^{x} g(x^*)\mathrm{d}x^* \tag{6.1c}$$

In Monte Carlo methods, the cumulative distribution function is set equal to a pseudo-random number, R.

$$F(x) = R \tag{6.1d}$$

$$x = F^{-1}(R) \tag{6.1e}$$

The method applied to solve radiative transfer problems typically involves selecting position, direction, wavelength as well as emission, reflection and scattering characteristics according to probability distributions and assuming radiative variables such as wavelength, polar and azimuthal angle, co-ordinates for position are independent of each other so that:

$$F_\theta(\theta) = R_\theta \tag{6.2a}$$

$$F_\phi(\phi) = R_\phi \tag{6.2b}$$

and so on. From the above relations, θ, ϕ and other variables can be determined, based on random numbers R_θ, R_ϕ etc. and if the cumulative distribution function is known. For example, for diffuse emission or reflection from a point, it can be shown that (Modest, 2003):

$$F_\theta(\theta) = \sin^2\theta \tag{6.2c}$$

For emission or reflection independent of azimuthal angle ϕ:

$$F_\phi(\phi) = \frac{1}{2\pi}\phi \tag{6.2d}$$

Thus, θ and ϕ for diffuse emission or reflection from a surface and for emission or reflection independent of azimuthal angle:

$$\theta = \sin^{-1}(R_\theta) \tag{6.2e}$$

$$\phi = 2\pi R_\phi \tag{6.2f}$$

Similarly, other radiative variables such as wavelength, position, attenuation path length (i.e. the distance traveled by a ray before it first encounters attenuation) and so on can be determined based on cumulative distribution functions, as described in (Modest, 2003).

6.2.2 MCRT for sintered ceria discs

An iterative collision-based MCRT method was developed to predict radiative properties of the medium. The geometry corresponds to that of the sintered ceria ceramics, and rays are traced in a cylindrical domain as shown in Fig. 6.1. A flowchart that describes the program flow is shown in Appendix D (Fig. C.1) together with random number relations and cumulative distribution functions. Initially, the transport extinction coefficient β_{tr} is set to a guess value. The transport scattering albedo ω_{tr} is set to a value obtained using an approximate analytical solution to the one-dimensional radiative transfer equation, described in section 6.3.1 (Dombrovsky and Baillis, 2010). In a single iteration, a large number of rays ($N_{\text{rays}} = 10^8$) are launched at the externally irradiated boundary A_1 of the medium from an aperture of diameter 2 mm. While the effect of interface reflection is weaker in comparison to reflection due to volumetric scattering for both dense and porous ceramics, the effect of interface reflection is included for the dense ceramics because of its lower porosity. For the dense ceramics, two types of boundary conditions were initially examined:

Case (1) Specularly reflecting boundaries:

For this case, the boundaries of dense samples were assumed to be specularly reflecting with interface reflectivity obtained from Fresnel equations for an interface between a perfect dielectric and a weakly absorbing medium:

$$\rho_{\parallel} = \frac{(p - n_1 \sin\theta_1 \tan\theta_1)^2 + q^2}{(p + n_1 \sin\theta_1 \tan\theta_1)^2 + q^2} \rho_{\perp} \tag{6.3a}$$

$$\rho_{\perp} = \frac{(n_1 \cos\theta_1 - p)^2 + q^2}{(n_1 \cos\theta_1 + p)^2 + q^2} \tag{6.3b}$$

$$\rho'^{\cap} = \frac{\rho_{\parallel} + \rho_{\perp}}{2} \tag{6.3c}$$

where θ_1 is the incidence angle, n_1 is the index of refraction of the surroundings and for the present case is set to unity, and $\rho'^{\cap}$ is the directional-hemispherical reflectivity

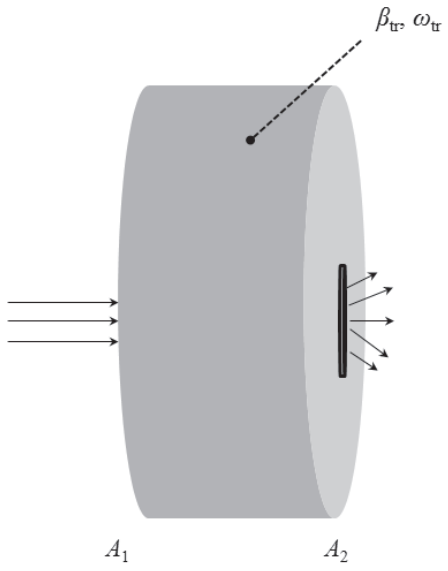

Figure 6.1: Domain for Monte Carlo ray-tracing of sintered ceria samples

of the interface between the surroundings denoted by the subscript 1 and the medium denoted by the subscript 2. p and q are given by:

$$p^2 = \frac{1}{2}\left[(\sqrt{n_2^2 - k_2^2 - n_1^2\sin^2\theta_1)^2 + 4n_2^2k_2^2} + (n_2^2 - k_2^2 - n_1^2\sin^2\theta_1)\right] \tag{6.4a}$$

$$q^2 = \frac{1}{2}\left[(\sqrt{n_2^2 - k_2^2 - n_1^2\sin^2\theta_1)^2 + 4n_2^2k_2^2} - (n_2^2 - k_2^2 - n_1^2\sin^2\theta_1)\right] \tag{6.4b}$$

When a ray encounters a boundary, a random number R_ρ is generated, and compared to the interface reflectivity obtained according to eq. (6.3c) for a given angle of incidence of the ray with the boundary. If $R_\rho \leq \rho'^{\cap}$ then rays are specularly reflected at the boundary with the angle of reflection equal to angle of incidence.

Refraction for this case is predicted by Generalized Snell's law:

$$p\tan\theta_2 = n_1\sin\theta_1 \tag{6.5}$$

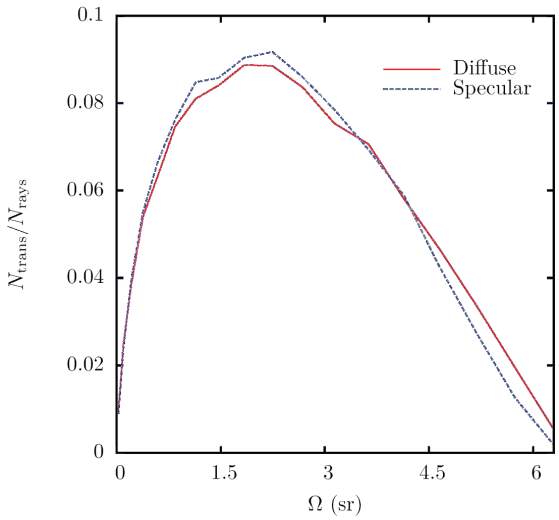

Figure 6.2: Non-dimensional radiative intensity plotted as a function of solid angle for two different reflection conditions

Case (2) Diffusely reflecting boundaries:

Reflectivity for diffusely reflecting boundaries is obtained by integrating the directional-hemispherical reflectivity given by Fresnel equation, eq. 6.3c over a hemisphere and assuming diffuse irradiation at incidence (Modest, 2003):

$$\rho = \frac{1}{\pi} \int_{2\pi} \rho^{'\cap} \cos\theta_i \mathrm{d}\Omega_i \tag{6.6}$$

A comparison of angular distribution of transmitted rays for the two boundary conditions is shown in Fig. 6.2 for highly scattering optically thick media (which is physically representative of the problem at hand). Figure 6.2 is a plot of non-dimensional radiative intensity plotted against the solid angle. This confirms that for highly-scattering optically thick materials, the angular distribution of transmitted rays is identical for both specular and diffuse reflection conditions at the boundary. Hence, the boundaries of dense ceramics are assumed to be diffusely reflecting. For the porous ceramics, boundaries are assumed to be non-reflecting and non-refracting because the effect of

reflection at the interface is weak as estimated by Fresnel equations, eq. (6.1), for a weakly absorbing medium with n $\approx$ 2.2 for media with high porosity.

The attenuation path length in the medium is calculated as:

$$s = \frac{-1}{\beta} \ln(R_\beta) \tag{6.7}$$

where R_β is a random number from a uniform distribution in the interval (0,1). At the location of the collision, another random number, R_ω, is generated and compared to ω_{tr} to determine the type of attenuation. If $R_\omega > \omega_{\text{tr}}$ absorption occurs and the ray history is terminated. Otherwise, the ray is scattered, and the direction of the scattered ray is determined. While any of the approximate phase functions, such as Henyey-Greenstein phase function can be used at this point to determine the direction of the scattered ray, for the present work, transport scattering phase function is assumed according to eq. 2.8 resulting in the direction of the scattered ray given by:

$$\phi = 2\pi R_\phi \tag{6.8a}$$

$$\theta = \cos^{-1}(1 - 2R_\theta) \tag{6.8b}$$

$$\hat{\mathbf{s}} = \sin\theta\cos\phi\hat{\mathbf{t}}_\mathbf{1} + \sin\theta\sin\phi\hat{\mathbf{t}}_\mathbf{2} + \cos\theta\hat{\mathbf{n}} \tag{6.8c}$$

R_ϕ and R_θ are random numbers generated for each scattering event to determine the direction of the scattered ray, and $\hat{\mathbf{t}}_\mathbf{1}$, $\hat{\mathbf{t}}_\mathbf{2}$ and $\hat{\mathbf{n}}$ are mutually perpendicular unit vectors that form a right-handed system. Another attenuation path length is generated at the location of scattering (eq.6.7) and ray-tracing is repeated.

When a ray reaches a boundary, for the porous samples, if the ray lies within the aperture at boundary A_2, the number of transmitted rays is incremented by one. For the dense samples, a random number, R_ρ is generated to examine total internal reflection. If $R_\rho < \rho$, where ρ is the interface reflectivity, given by eq. 6.6, then rays suffer total internal reflection at the boundaries of the medium. The direction of the reflected ray

for diffuse reflection is given by:

$$\phi = 2\pi R_\phi \tag{6.9a}$$

$$\theta = \sin^{-1}\left(\sqrt{R_\theta}\right) \tag{6.9b}$$

$$\hat{\mathbf{s}} = \sin\theta\cos\phi\hat{\mathbf{t}}_\mathbf{1} + \sin\theta\sin\phi\hat{\mathbf{t}}_\mathbf{2} + \cos\theta\hat{\mathbf{n}} \tag{6.9c}$$

As described previously, R_ϕ and R_θ are random numbers generated for each reflection event to determine the direction of the reflected ray, and $\hat{\mathbf{t}}_\mathbf{1}$, $\hat{\mathbf{t}}_\mathbf{2}$ and $\hat{\mathbf{n}}$ are mutually perpendicular unit vectors that form a right-handed system. If the ray lies within the aperture at boundary A_2, the number of transmitted rays is incremented by one. Bi-normal transmittance is calculated using the number of rays exiting the medium through the aperture on the non-irradiated boundary A_2 within a narrow cone angle, corresponding to the acceptance angle of the experimental setup shown in Fig. 3.2. The aperture diameter for the simulations was 4 mm and the cone angle was 6°. Iterations are repeated by adjusting the transport extinction coefficient until the computed transmittance shows agreement with that obtained experimentally for samples of different thickness. Measured transmittance shown in Figs. 5.1 and 5.2 were averaged over a narrow spectral range of 0.9 – 1.4 μm to eliminate the high computational cost associated with iterations at several wavelengths, especially for optically thick media.

6.2.3 MCRT for 3DOM packed bed

Monte Carlo ray-tracing procedure for 3DOM packed bed of ceria powder is similar to that of the sintered discs of porous ceria with the exception that the computational domain for the simulation corresponds to the geometry of the sample holder, shown in Fig. 4.4 and the experimental setup representing normal-hemispherical reflectance. The computational domain for ray-tracing is shown in Fig. 6.3. In a single iteration, large number of rays are launched outside the transparent window of the sample holder

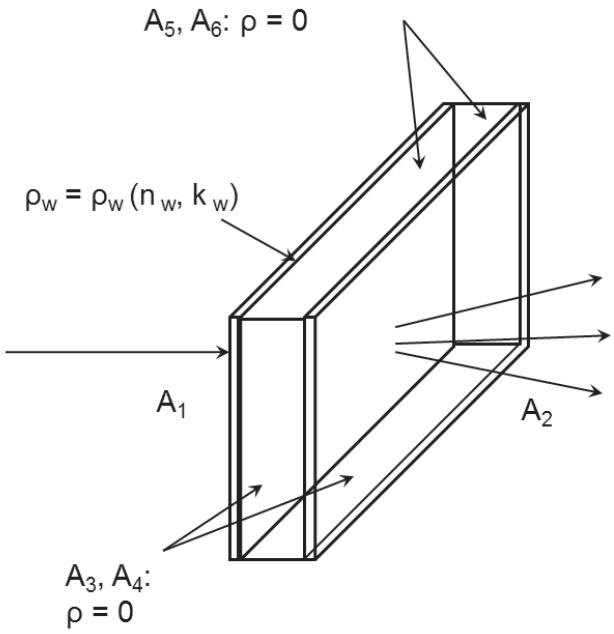

Figure 6.3: Domain for Monte Carlo ray-tracing of 3DOM packed bed

on the left boundary, A_1. The reflectivity of the windows are determined according to Fresnel equation for normal incidence of rays, eqs. (6.3a) – (6.3c). A sub-program that performs ray-tracing through the window is called. Ray-tracing through the windows is detailed in Appendix C (Fig. C.3). When a ray transmitted by the window, it encounters the packed bed of ceria powder. Transport radiative properties, namely extinction coefficient and scattering albedo are assumed. Attenuation path length is generated according to eq. (6.7). The direction of the scattered ray is given by eqs. (6.9a) – (6.9c), similar to ray-tracing for the sintered ceria discs.

When a ray encounters one of the two transparent windows of the sandwich during

the iteration, the sub-program that performs ray-tracing in the windows is called to determine if the ray exits the medium or internally reflected back into the powder. If a ray encounters the left (irradiated) boundary, A_1 and is transmitted, a counter for reflected rays is incremented by one if it lies within a circular area equal to the area of the reflectance port of the spectrophotometer. If the ray encounters the right (non-irradiated) boundary, A_2 and is transmitted, a counter for transmitted rays is incremented by one if it lies within a circular area equal to the area of the transmittance port of the spectrophotometer. If a ray lies outside the area on these boundaries, or if it encounters other boundaries, A_3 – A_6 the ray is treated as a "lost" ray. This is because these boundaries represent metal plates in the sample holder assembly and were painted black, thus absorbing the ray. The top boundary was open to surroundings.

Reflectance and transmittance from Monte Carlo simulations are computed as follows:

$$T_{\text{MC}} = \frac{N_{\text{trans}}}{N_{\text{rays}}} \tag{6.10a}$$

$$R_{\text{MC}} = \frac{N_{\text{refl}}}{N_{\text{rays}}} \tag{6.10b}$$

Here, N_{trans} and N_{refl} refer to the number of rays transmitted or reflected, and N_{rays} refers to the total number of rays launched. Transmittance and reflectance obtained from MCRT simulations are compared to the measured directional-hemispherical transmittance and reflectance. Normalized error in the MCRT simulations is defined as:

$$\epsilon_{\text{T}} = \frac{|T_{MC} - T_{\text{d-h}}|}{T_{\text{d-h}}} \tag{6.11a}$$

$$\epsilon_{\text{R}} = \frac{|R_{MC} - R_{\text{d-h}}|}{R_{\text{d-h}}} \tag{6.11b}$$

Iterations are repeated by adjusting the transport scattering albedo and transport extinction coefficient, till ϵ_{T} and ϵ_{R} reach a value less than 0.015, corresponding to less than

Table 6.1: Transmittance and reflectance obtained from MCRT simulations for various values of N_{rays}

β_{tr} (mm^{-1})	ω_{tr}	N_{rays}	$T_{\text{MC}}\%$	R_{MC} %
5	0.995	10^4	37.619	59.760
		10^5	37.939	59.243
		10^6	37.798	59.358
		10^7	37.766	59.396
		10^8	37.785	59.378
65	0.998	10^4	1.379	87.940
		10^5	1.350	87.904
		10^6	1.334	87.910
		10^7	1.332	87.881
		10^8	1.335	87.864

1.5% difference in computed transmittance and reflectance and measured transmittance and reflectance.

To ensure that sufficiently large number of rays were used to obtain converged statistical distribution, convergence tests were conducted for β_{tr} = 5 mm^{-1} and ω_{tr} = 0.995, and β_{tr} = 65 mm^{-1} and ω_{tr} = 0.998. Chosen extinction coefficient and scattering albedo for the convergence study are anticipated as representative radiative properties of the material based on the measured directional-hemispherical transmittance and reflectance (Dombrovsky and Baillis, 2010). Table 6.1 lists the computed transmittance reflectance from the MCRT simulations for N_{rays} = 10^4, 10^5, 10^6, 10^7 and 10^8. Based on the convergence study, 10^6 rays were chosen for the MCRT simulations for the 3DOM packed bed.

6.3 Approximate solutions

Two approximate solutions were employed to predict radiative properties of sintered ceria discs. Both calculations were performed by visiting researcher at the solar energy laboratory, L. A. Dombrovsky (Dombrovsky et al., 2012). This section justifies the use of these solutions and describes the contributions of these solutions to radiative property prediction. As mentioned earlier in the methodology, one of the short-comings of the radiative transfer measurements of sintered ceria discs is its high-optical thickness, resulting in noisy directional-hemispherical transmittance, as well as long simulation times of Monte Carlo ray-tracing procedure. In order to reduce the computational cost with the iterative Monte-Carlo technique, an approximate hybrid computational technique was employed for the sintered ceria discs. One must note that inferred radiative properties of sintered ceria samples have a higher uncertainty than the packed bed of 3DOM samples because of this approximate hybrid procedure.

6.3.1 Modified two-flux approximation

The modified two-flux approximation is applied to obtain an approximate solution to the one-dimensional radiative transfer problem, in order to identify transport scattering albedo. The approximate solution gives the following relation for directional-hemispherical reflectance of optically thick samples (Dombrovsky et al., 2006):

$$R_{\text{d-h}} = R_1 + (1 - R_1)\frac{\gamma}{2n^2}\frac{\omega_{\text{tr}}}{1 - \omega_{\text{tr}}}\frac{\chi^2}{(1+\chi)(2\gamma/(1+\mu_{\text{c}}+\chi)} \tag{6.12a}$$

$$\chi^2 = \frac{4}{(1+\mu_c)^2}\frac{1-\omega_{tr}}{\omega_{tr}\mu_c} \tag{6.12b}$$

$$\gamma = \frac{1-R_1}{1+R_1} \tag{6.12c}$$

$$\mu_c = \sqrt{1-1/n^2} \tag{6.12d}$$

$$R_1 = \frac{1}{2} + \frac{(3n+1)(n-1)}{6(n+1)^2} + \frac{n^2(n^2-1)^2}{(n^2+1)^3}\ln\left(\frac{n-1}{n+1}\right) - \frac{2n^3(n^2-2n+1)}{(n^2+1)(n^4-1)} + \frac{8n^4(n^4+1)}{(n^2+1)(n^4-1)^2}\ln n \tag{6.12e}$$

Eq. (6.12a)–(6.12e) relate the transport scattering albedo to measured directional-hemispherical reflectivity, and the index of refraction of ceria, *n*.

6.3.2 Mie theory for sintered discs

In order to extend the spectral range of identification of transport radiative properties, and to examine if theoretical predictions based on Mie scattering theory and independently scattering spherical pores and grains could be employed to describe radiative transfer phenomenon in the sintered discs, Mie theory calculations were employed.

The computation treats the sintered discs to be made of scatterers dispersed in a host medium. For dense ceria samples, the scatterers are pores dispersed in ceria, as the volume fraction of pores are small (0.08). For porous ceria ceramics, the scatterers are grains of ceria dispersed in air because of high porosity of 0.72. The pores and grains are assumed to be independently scattering, i.e. the presence of adjacent particles or pores do not influence scattering from a single particle or pores. As seen from the SEM images of the sintered ceria discs (Fig. 4.1.1), the pores of the dense sample are spherical, whereas grains of the porous ceramics randomly shaped. However, both pores and grains are treated as spherical scatterers.

The SEM images of sintered ceria discs indicate that the pores and grains are polydisperse, are not of constant size. Ceria powder employed for preparing the sintered discs were analyzed by a particle size counter by Alfa Aesar. The particle size distribution of the powder indicated that sintering the powder may cause the resultant sintered discs to have pores and grains of a similar, though not identical size distribution. Size distribution of the grains and pores after sintering cannot be reliably determined by image analysis of SEM images. Thus, the size distribution of pores and grains were assumed to be a two-parameter gamma distribution.

The two-parameter gamma distribution has been successfully employed to predict radiative properties of many disperse systems (Dombrovsky and Baillis, 2010), and is as follows:

$$F(a) = \frac{A^{B+1}}{\Gamma(B+1)} a^B e^{-Aa} \tag{6.12a}$$

$$\int_0^\infty F(a)da = 1 \tag{6.12b}$$

Here $F(a)$ refers to the frequency and a refers to the radius of the particle or pore, and A and B are constants of the size distribution. $F(a)$ has a maximum at a_{m} = B/A. The maximum of size distribution a_m is representative of the radius of most particles or pores in the distribution.

If the size distribution of particles and pores are known, scattering and absorption coefficients based on Mie theory can be obtained by the following relations:

$$\sigma = f_{\mathrm{v}} \int_0^\infty Q_{\mathrm{sca}} F(a) \pi a^2 da \tag{6.12c}$$

$$\kappa = f_{\mathrm{v}} \int_0^\infty Q_{\mathrm{abs}} F(a) \pi a^2 da \tag{6.12d}$$

The quantities Q_{sca} and Q_{abs} are the scattering and absorption efficiencies of a single sphere (pore or grain) and can be obtained from Mie scattering theory using the freely-available computer code, *bhmie* (Bohren and Huffman, 1998). Mie theory for spherical

grains of porous ceria is applicable even in the spectral range of strong bulk absorption, $0.3 < \lambda < 0.5$ μm. This is because of weaker absorption of incident radiation by the porous samples than the dense samples due to higher volume fraction of bulk ceria in the latter. For dense samples because of the higher volume fraction of the bulk material, absorption is expected to be stronger. Hence, only the spectral range of weak absorption, $\lambda > 0.5$ μm is considered because of limited applicability of both the radiation transfer theory and far-field Mie solution in the case of strong absorption of the incident radiation in the material at distances comparable to both pore size and wavelength.

Identification of absorption coefficient requires knowledge of index of absorption in the entire spectral range of identification. Absorption coefficient of the porous ceramics can be obtained in the short-wave part of the spectrum, $\lambda < 0.5$ μm, by directly employing Mie theory and using known index of absorption for this spectral range, shown in Fig. 4.6. For $\lambda > 0.5$ μm, however, the index of absorption is unknown due to uncertainties in determination of low values of index of absorption. Thus, absorption coefficient for both ceramics for $\lambda > 0.5$ μm can be obtained by combining transport scattering coefficient obtained by Mie calculations with the data for transport scattering albedo obtained from eqs. (6.12a) – (6.12e):

$$\kappa = \frac{1 - \omega_{\text{tr}}}{\omega_{\text{tr}}} \sigma_{\text{tr}} \tag{6.13}$$

For the present problem, the size distribution is unknown, and hence, and indirect approach is employed. In this approach, the scattering coefficient from MCRT simulations is compared to that from Mie theory for a given value of a_{32}. The radius for which scattering coefficient from Mie theory matches that from MCRT is then used to compute the size distribution parameters, while fixing the value of B = 2.5. Based on the analysis shown in (Dombrovsky and Baillis, 2010), Mie calculations are insensitive to particular combinations of A and B, for a fixed value of a_{32}. Sauter radii of pores of the dense ceramics and grains of the porous ceramics obtained by best fits of this procedure were

found to be equal to 2.9 μm and 7.5 μm respectively. The identified Sauter radii lead to the radii at the maximum of the distribution $a_{\mathrm{m}} \approx 1.3$ μm for the pores of dense ceramics and $a_{\mathrm{m}} \approx 3.4$ μm for the grains of porous ceramics, which are representative of the radius of maximum number of pores or grains in the distribution. Comparing the estimated sizes of pores and grains to SEM images of the sintered discs shown in Fig. 4.1.1, it can be seen that the estimated size distribution is representative of the pores and grains of the sintered discs.

From the computed size distribution, the median diameter for grains of the porous ceramics is calculated to be $d_{\mathrm{med}} \approx 8.6$ μm, which shows reasonable agreement with the mass-median diameter of the powders, 5 μm used for preparing the porous samples, and measured by the vendor using a particle size analyzer. Further, from the two-parameter gamma distribution, arithmetic mean diameter of grains of the porous ceramics is 9.6 μm for grains of the porous ceramics, which is comparable to the mean diameter of the powder of 6.6 μm. Higher mean and median diameter of the grains than those of the powders is possibly as a result of sintering ceria powder at 1000 °C for 2 h and 1500 °C for 5 h. Despite these differences, the two-parameter gamma distribution shows reasonable agreement with the cumulative frequency distribution of ceria powder, providing the estimated pore and grain sizes some physical basis. The estimated particle size distributions are then used in Mie calculations for a wider spectral range.

6.4 Results

6.4.1 Sintered ceria discs

Directional-hemispherical reflectance of optically thick sintered discs of thickness L = 1.88 mm for the dense sample and L = 1.92 mm for the porous sample, shown in

Figs. 5.5 and 5.6 is used to identify transport scattering albedo, using eqs. (6.12a) – (6.12e). Identified transport scattering albedo for dense and porous ceria sintered discs is shown in Fig. 6.4. Transport scattering albedo does not show any wavelength dependence after a wavelength of 0.5 μm and approaches values close to unity. Recall that transport scattering albedo is a fraction whose value indicates the probability that attenuation occurs by scattering. Transport scattering albedo close to unity indicates that attenuation is predominantly by scattering after 0.5 μm.

Identified transport scattering albedo was used in the Monte Carlo ray-tracing simulations as a guess value, and transport extinction coefficient was adjusted until a reasonable match was obtained between measured bi-normal transmittance, $T_{\text{d-d}}$ and bi-normal transmittance computed by MCRT simulations, T_{MC}. A comparison of these two quantities for dense and porous samples is shown in Fig. 6.4.1. From the MCRT iterations, transport extinction coefficient of dense and porous ceria in the spectral range 0.9 – 1.4 μm were found to be 16 mm^{-1} and 26 mm^{-1}. Computed transport extinction coefficient and scattering albedo indicate that the attenuation path is on the order of 0.0625 and 0.0385 mm for the dense and porous samples respectively. Short attenuation path lengths and scattering albedo close to unity together imply that at longer wavelengths, incident radiation gets scattered within a short distance and is ultimately reflected back, resulting in a high value of directional-hemispherical reflectance.

Size distribution of pores and grains of the dense and porous discs are used to extend the spectral range of identification using Mie scattering theory, as outlined in Section 6.3.2. Transport scattering coefficient predicted by Mie theory is shown in Fig. 6.6. Large values of scattering coefficient, on the order of 20 mm^{-1} in the spectral range 0.3 $< \lambda <$ 0.5 μm indicates that even in the visible spectrum, incident radiation is strongly scattered within a short distance of travel within the medium.

The absorption coefficient determined by Mie theory in the spectral range $\lambda <$ 0.5

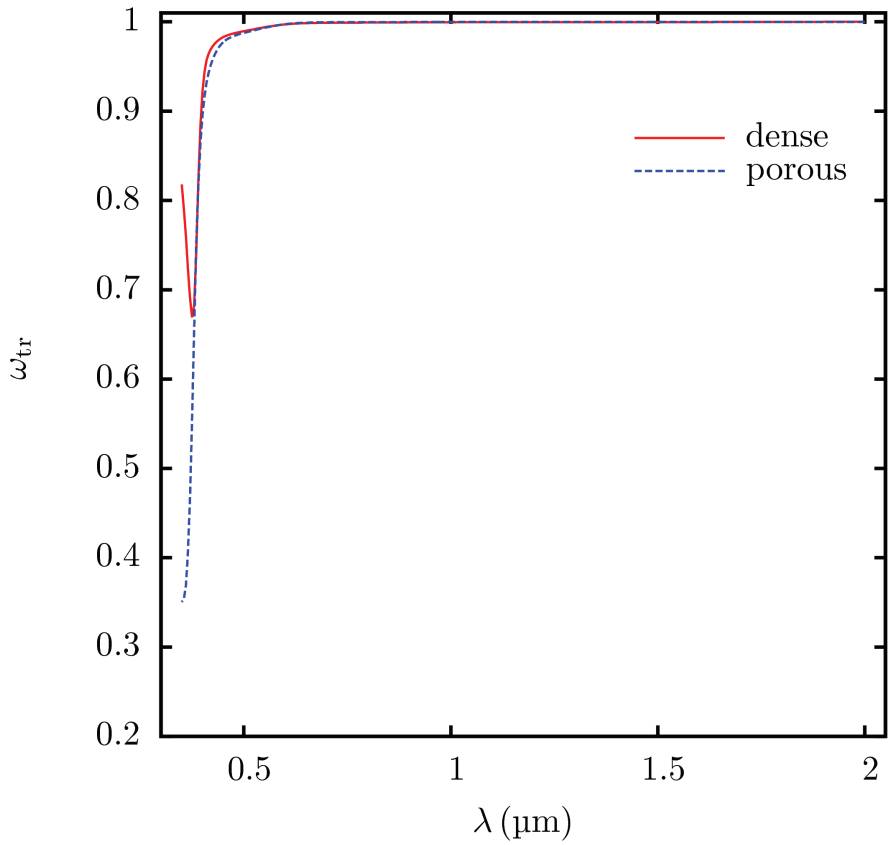

Figure 6.4: Transport scattering albedo of sintered ceria discs obtained from directional-hemispherical transmittance, and eqs. (6.12a) – (6.12e). Calculations were performed by L. Dombrovsky (Dombrovsky et al., 2012). The ceramics were of porosity $p_1 = 0.08$ (dense) and $p_2 = 0.72$ (porous).

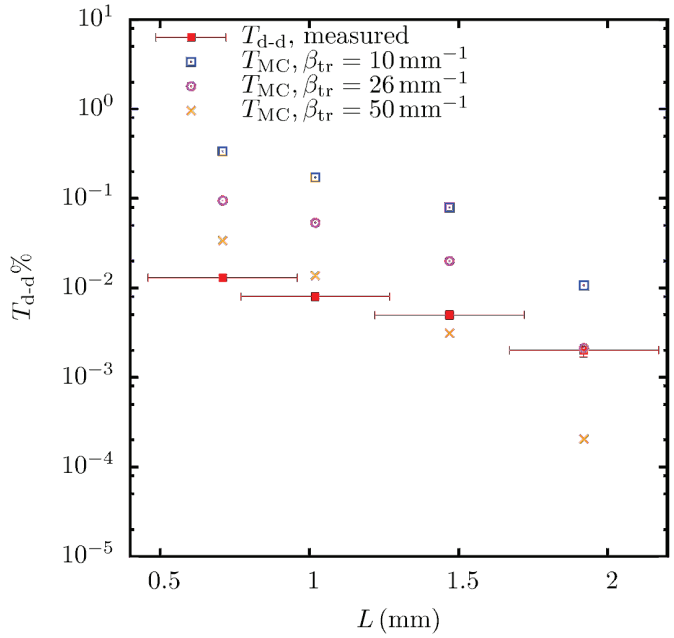

(a)

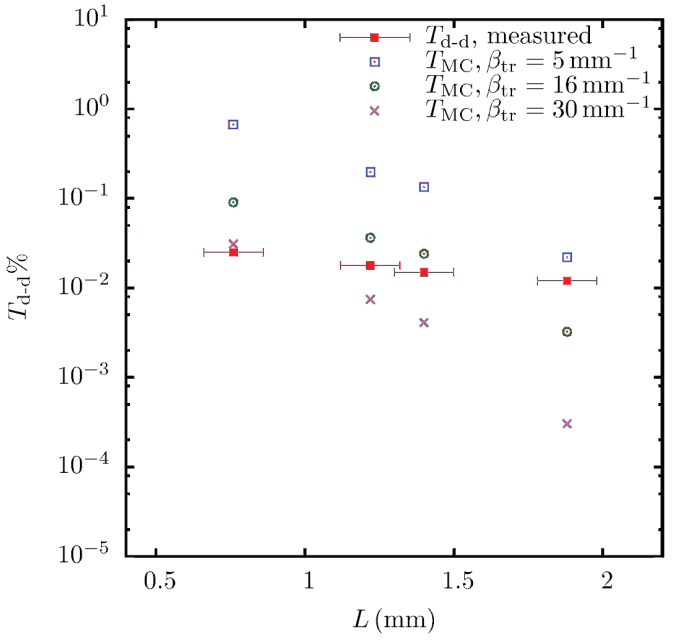

(b)

Figure 6.5: Bi-normal transmittance computed by MCRT simulations, T_{MC} for various values of β and fixed values of ω_{tr} for (a) porous samples (p = 0.72), $\omega_{\text{tr}} = 0.999$ and (b) dense samples (p = 0.08), $\omega_{\text{tr}} = 0.997$ plotted together with measured bi-normal transmittance, $T_{\text{d-d}}$.

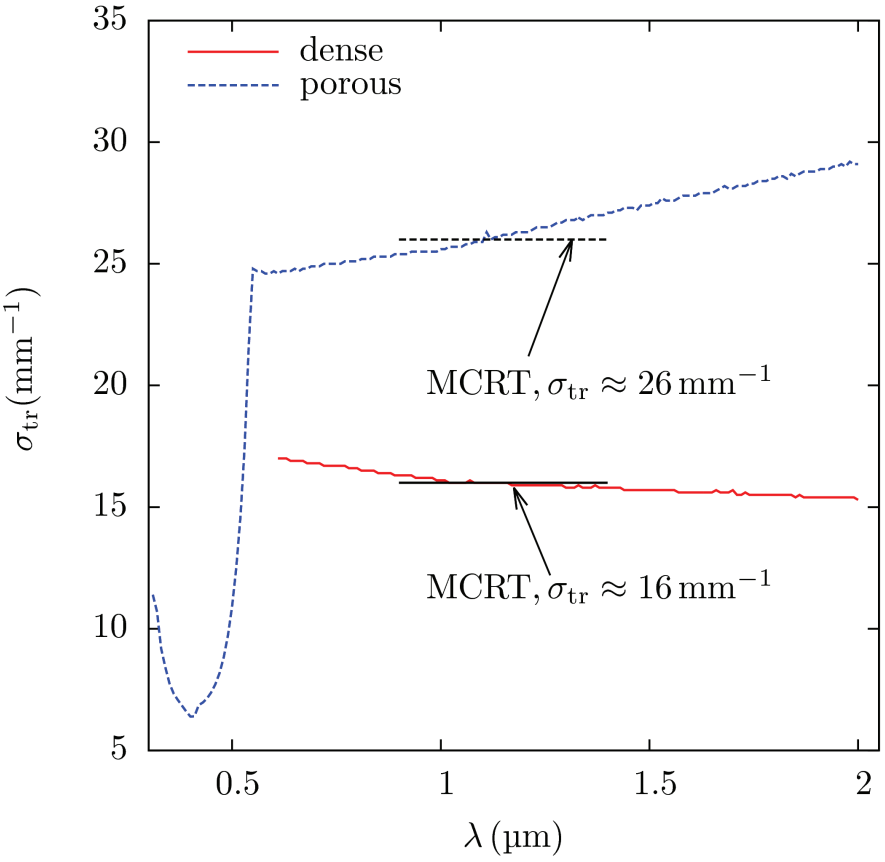

Figure 6.6: Transport scattering coefficient of sintered ceria discs obtained by Mie theory and MCRT simulations. Mie calculations were performed by L. Dombrovsky (Dombrovsky et al., 2012). The ceramics were of porosity p_1 = 0.08 (dense) and p_2 = 0.72 (porous).

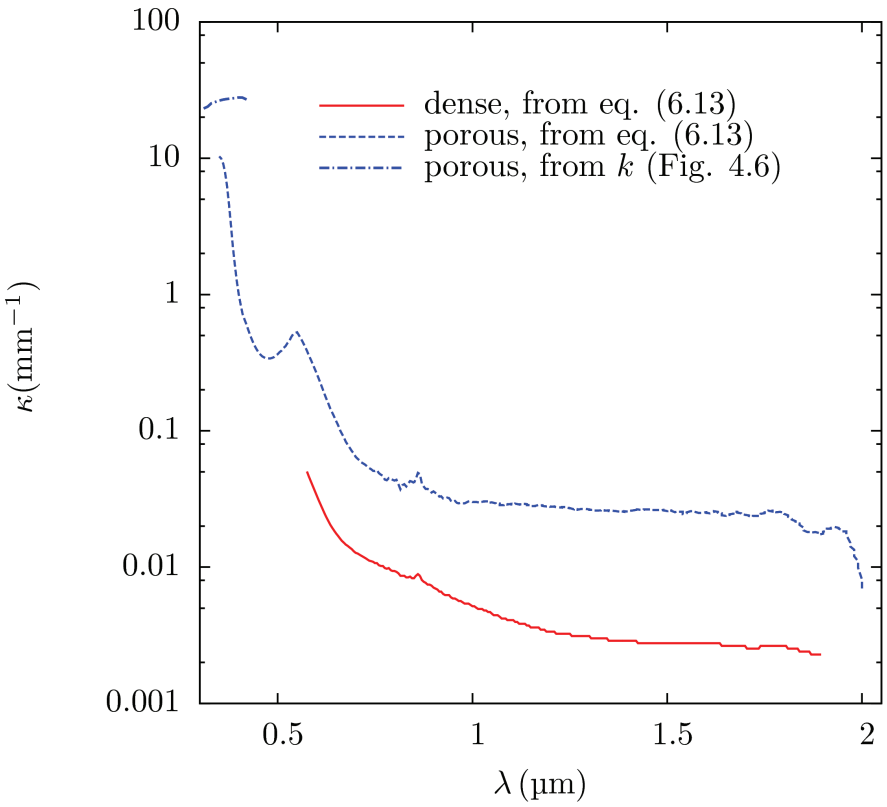

Figure 6.7: Absorption coefficient of sintered ceria discs obtained by Mie theory, and using eq. (6.13). Mie calculations were performed by L. Dombrovsky (Dombrovsky et al., 2012). The ceramics were of porosity $p_1 = 0.08$ (dense) and $p_2 = 0.72$ (porous).

μm and by eq. 6.13 in the spectral range $\lambda < 0.5$ μm is shown in Fig. 6.7. In the spectral range $\lambda > 0.5$ μm, absorption coefficient reaches small but non-zero values. Determination of absorption coefficient is critical to obtaining heat transfer rate due to absorption of infrared radiation, and consequently, temperature distribution in the reacting medium during thermochemical cycling.

6.4.2 3DOM ceria packed bed

Determination of radiative properties for 3DOM ceria packed bed was a relatively easier process than that of sintered ceria ceramics. This is because of the ability to measure both directional-hemispherical transmittance and reflectance of the samples, because of lower optical thickness of the 3DOM ceria packed bed than sintered ceria discs. Measured directional-hemispherical transmittance and reflectance, shown in Figs. 5.7 – 5.10 were directly employed to infer transport scattering coefficient and absorption coefficient using MCRT technique, described in section 6.2.2 by iteratively updating guess values of radiative properties and comparing the computed transmittance and reflectance from the simulations to measured transmittance and reflectance.

Identified transport scattering coefficient and absorption coefficient for 3DOM ceria packed bed of three thicknesses before thermochemical cycling are shown in Figs. 6.8 and 6.9 respectively. Computations at different thicknesses were performed to ensure that identified transport scattering coefficient and absorption coefficient are representative for samples of all thicknesses. From Figs. 6.8 and 6.9 it can be seen that the transport radiative properties do not show a strong dependence on thickness. Similar to the sintered ceria ceramics, high values of scattering coefficient, on the order of 70 mm^{-1} in the spectral range $0.5 < \lambda < 0.8\ \mu\mathrm{m}$ indicates that in the long-wave portion of the visible spectrum, incident radiation is strongly scattered within a short distance of travel of the incident radiation within the medium. Computed directional-hemispherical transmittance and reflectance using the final values of transport radiative properties are compared to measured transmittance and reflectance in Fig. 6.4.2 and good agreement between measurements and MCRT simulations is observed.

Transport scattering coefficient decreases with wavelength after $0.8\ \mu\mathrm{m}$, which is

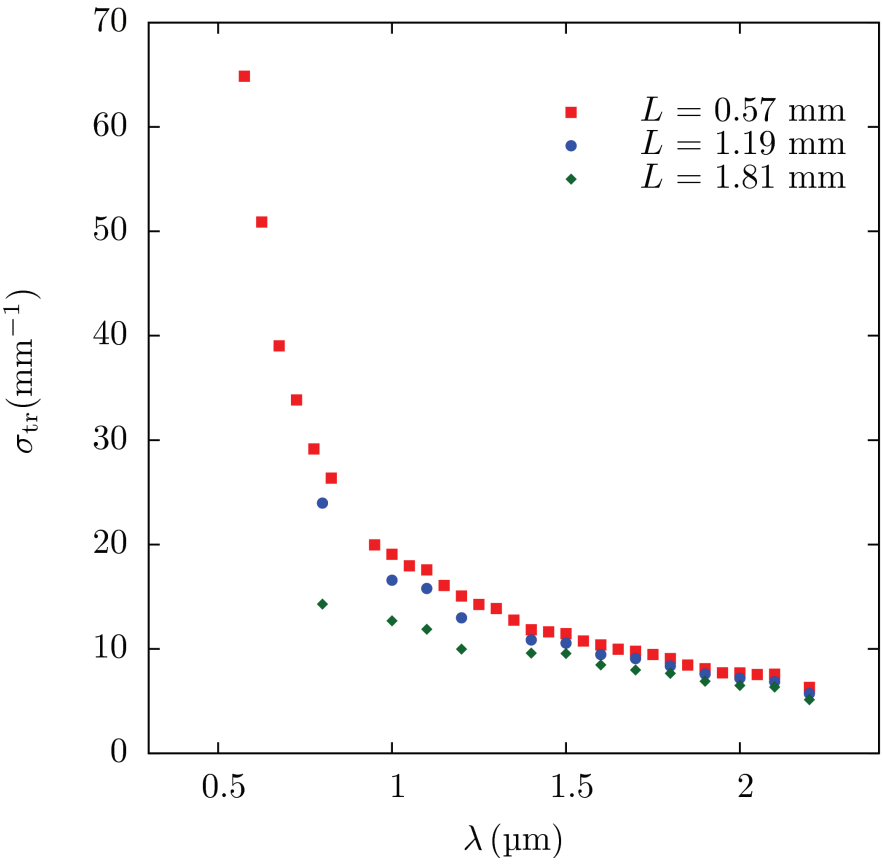

Figure 6.8: Transport scattering coefficient of 3DOM ceria packed bed before thermochemical cycling obtained by MCRT simulations.

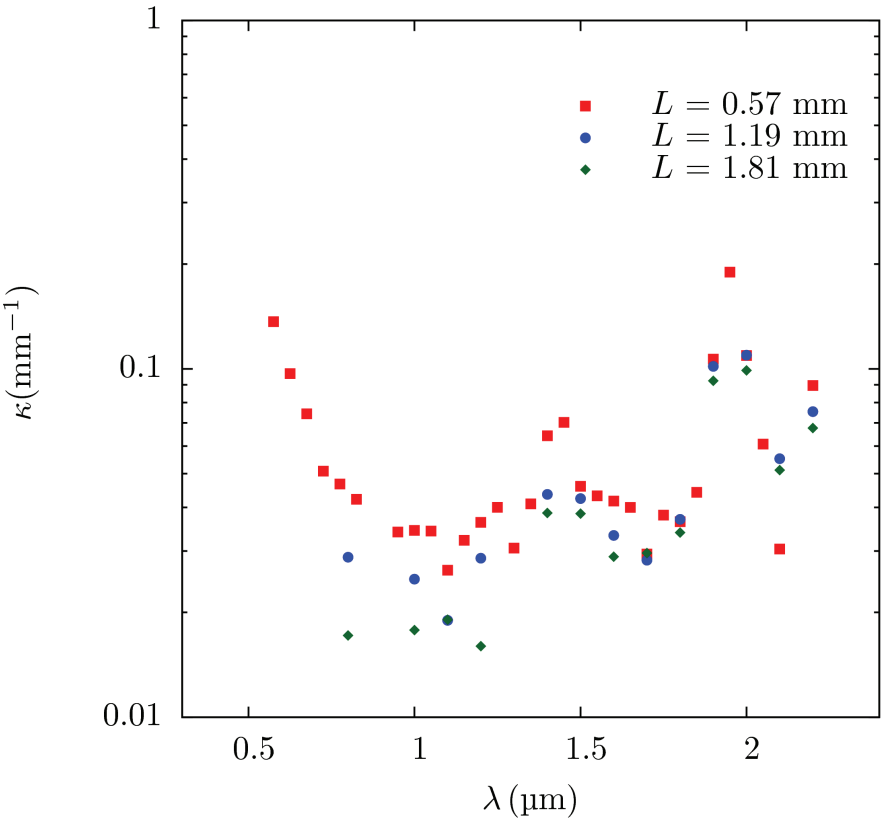

Figure 6.9: Absorption coefficient of 3DOM ceria packed bed before thermochemical cycling obtained by MCRT simulations.

typical behavior for scattering by particles or pores of size less than radiation wavelength (van de Hulst, 1981). [1] The spectral trend of transport scattering coefficient indicates that scattering is caused by morphological features of characteristic size less than 1 μm. It is hypothesized that macropores of diameter ~ 0.48 μm in the 3DOM structure are the predominant cause for scattering in these samples. Computing a size-factor, defined by eq. (2.10),:

$$x = \frac{2\pi a_p}{\lambda} \tag{6.1}$$

where a_{p} is the radius of pore or grain, the size factor at a wavelength of 0.8 μm is 1.9. A size-factor of 1 at a wavelength of 0.8 μm is obtained if $a_{\mathrm{p}} \approx 0.127$ μm, indicating that the effective cross-section for scattering is a sphere of diameter 0.25 μm.

The absorption coefficient decreases after a wavelength of 0.5 μm and remains nearly constant after this wavelength, except for peaks at 1.4 μm, and 2 μmwhich are attributable to the absorption peaks of the transparent windows made of UV-fused silica and water vapor in the pores. However, because experimental data and inferred radiative properties were for an effective medium, consisting of the windows and the powder made of 3DOM ceria with voids, inferred absorption coefficient is representative of the entire effective medium.

Transport scattering coefficient and absorption coefficient of 3DOM ceria packed bed after thermochemical cycling are shown in Figs. 6.11 and 6.12, respectively. Also shown in these figures for comparison are the identified radiative properties of 3DOM ceria packed bed of same thickness before thermochemical cycling and transport properties of sintered ceria discs. Transport scattering coefficient of 3DOM ceria packed bed increases approximately four times after thermochemical cycling and reaches values higher than that of the sintered porous ceria discs with grain sizes 6-7 μm.

[1] For the extreme case of particle or pore sizes much smaller than radiation wavelength, i.e. the

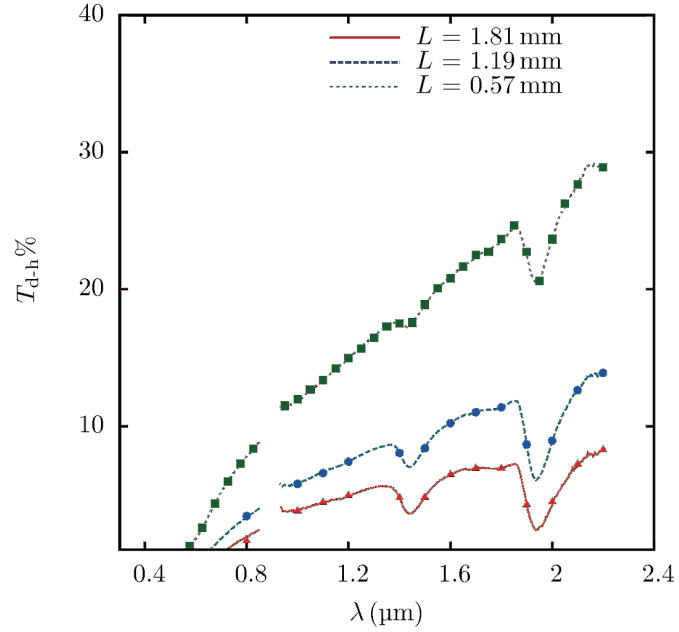

(a)

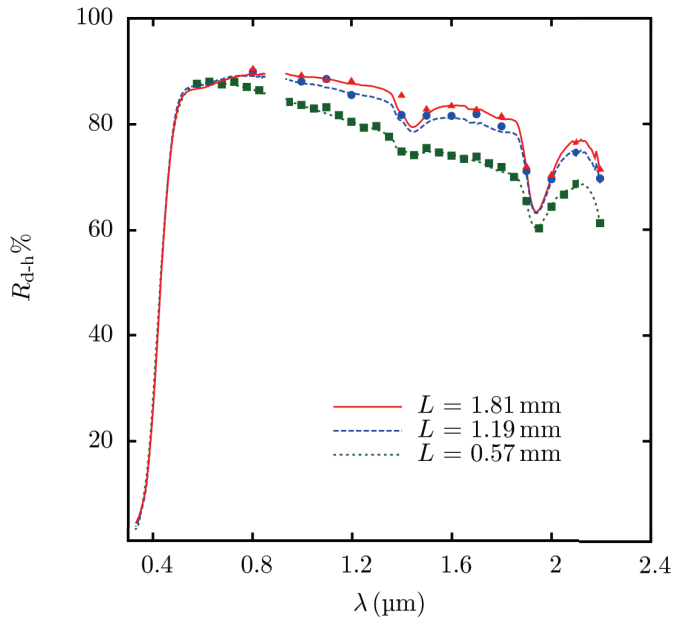

(b)

Figure 6.10: Comparison of experimental data and results of Monte-Carlo ray-tracing simulations (a) directional-hemispherical transmittance and (b) directional-hemispherical reflectance. Experimental data is represented by lines, and Monte Carlo ray-tracing simulations at selected wavelengths are indicated by points.

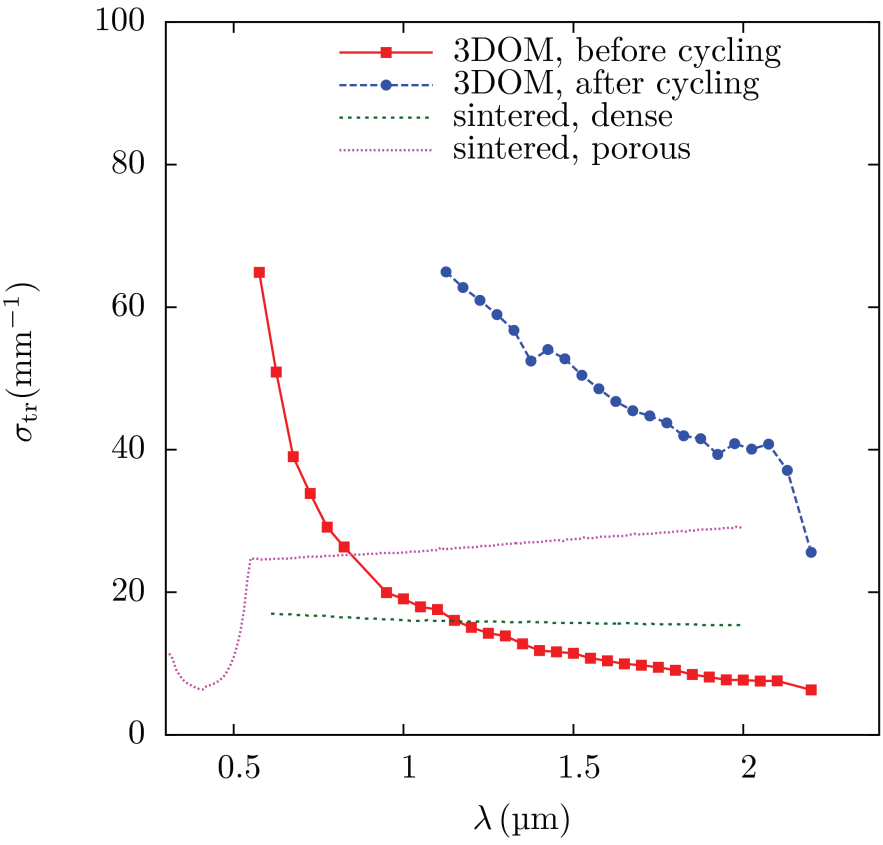

Figure 6.11: Transport scattering coefficient of 3DOM packed bed before and after thermochemical cycling. Also shown is the transport scattering coefficient of sintered ceria ceramics of porosity $p_1 = 0.08$ (dense) and $p_2 = 0.72$ (porous)

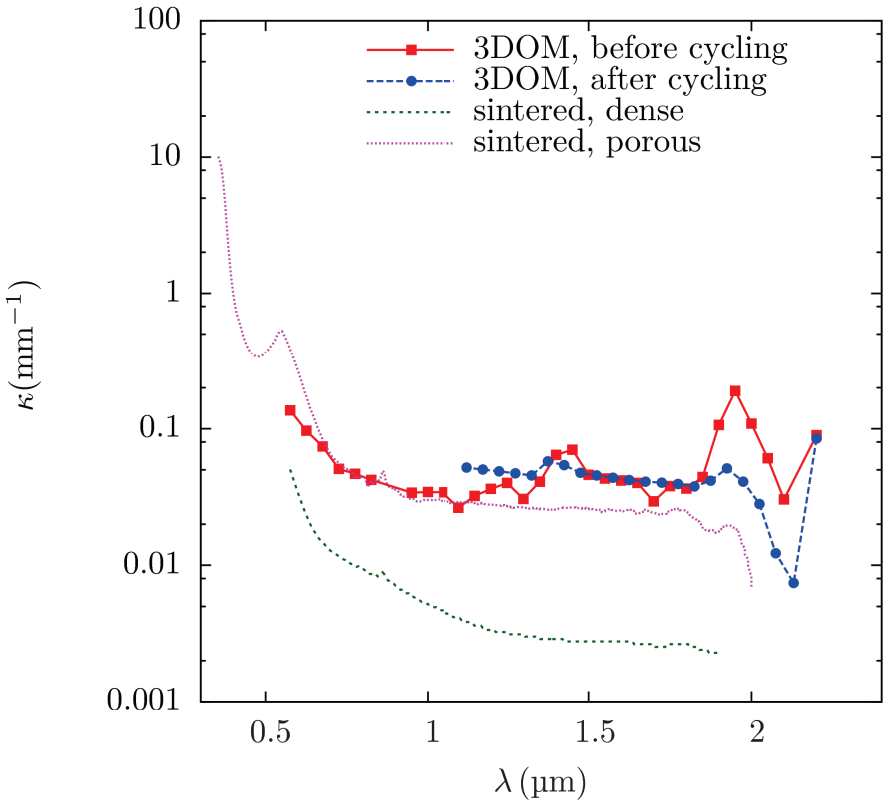

Figure 6.12: Absorption coefficient of 3DOM packed bed before and after thermochemical cycling. Also shown is the absorption coefficient of sintered ceria ceramics of porosity $p_1 = 0.08$ (dense) and $p_2 = 0.72$ (porous)

Absorption coefficient of 3DOM packed bed after thermochemical cycling is comparable to that before thermochemical cycling. Absorption of radiation is typically only dependent on the volume fraction of the bulk material (i.e. $1-p$, where p is the porosity of the medium). Porosity of the packed bed before and after thermochemical cycling was measured. Bed porosity prior to thermochemical cycling was 0.9 ± 0.05, and after thermochemical cycling was 0.83 ± 0.04, indicating that thermochemical cycling introduced only a small reduction in porosity in the material, and there is no change in absorption coefficient as a result of thermochemical cycling.

Absorption coefficient of the porous ceria cermaics of porosity 0.72 is comparable to those of the 3DOM ceria packed bed before and after thermochemical cycling. However, the absorption coefficient of the dense ceria ceramics of porosity 0.08 is lower than those of the porous ceramics, as well as the 3DOM ceria packed bed before and after thermochemical cycling. This difference is attributable to uncertainties in the identification procedure for the sintered ceria discs. An indirect multi-step approach was employed to infer the transport scattering and absorption coefficient of the sintered discs, resulting in higher uncertainty in the inferred transport radiative properties. Despite these differences, absorption coefficient of sintered ceria discs obtained indirectly is of the same order of magnitude as those of the 3DOM packed bed, which supports the use of independent scattering hypothesis and Mie theory to predict absorption coefficient of sintered ceria discs, and also suggests that the absorption coefficient is independent of morphology.

Rayleigh scattering regime, scattering coefficient decreases with wavelength, and the scattering efficiency, $Q_{\text{sca}} \sim \lambda^{-4}$.

6.5 Implications for solar thermochemical reactor design

Favorable characteristics of reacting media for solar thermochemical applications were reviewed in section 1.2. Reacting media must allow for efficient absorption of incident concentrated solar radiation and confine the emitted radiation within close visinity of the reaction site. Identifed radiative properties indicate that effective absorption of the visible solar radiation may be challenging to accomplish due to large optical thickness. This is because incident solar radiation must travel within the reacting medium in the thermochemical reactor to achieve uniform absorption of solar radiation to reach the temperatures required for driving the thermochemical reaction. A medium with high optical thickness and high scattering albedo indicates that the incident radiation travels only a short distance on the order of a few hundred microns as indicated by the attenuation path lengths identified from transport properties, before suffering multiple scattering events, ultimately getting absorbed or reflected within this short distance.

Non-uniform absorption of incident solar radiation at ambient temperature results in a steep temperature gradient along the direction of incidence. More effective absorption in the visible spectrum can also be achieved by increasing the free electron concentration in ceria or by decreasing the optical thickness of the material. Oxygen vacancies at high temperatures contribute to higher free electron concentration, as a result of which, at high temperatures, absorption coefficient is anticipated to be higher than the values obtained at ambient temperature. It is discussed in section 7.1 that multiphonon absorption results in higher absorption coefficient and emittance of ionic solids like metal oxides. As a result, even though properties of materials obtained at ambient temperature indicate weak absorption of of infrared radiation, this trend is expected to change at high temperatures encountered in solar thermochemical cycles.

Higher scattering coefficient in the infrared is desirable from thermochemical reactor design perspective, because multiple scattering events contains the radiation within the reacting medium, and also because only a small thickness of the reacting material is required, as the infrared radiation suffers shorter attenuation path lengths and ultimately gets absorbed by the reacting material. Reflected infrared radiation due to multiple scattering can also be favorably employed by suitable reactor design, which contains all the reflected radiation in a cavity.

Thermochemical characterization of various morphologies indicates that the 3DOM structure results in much higher fuel production in comparison to sintered morphologies due to higher specific surface area than the former (Venstrom et al., 2012). From a radiative transfer perspective, 3DOM structure is of comparable radiative and optical characteristics to achieve effective absorption and confinement of radiation as the sintered discs morphology, as long as the pore-morphology and size of the 3DOM structure is preserved during thermochemical cycling. A recent study has demonstrated that enhanced thermal stability with 3DOM ceria can indeed be achieved (Petkovich et al., 2011).

Inferred radiative properties suggest that for thermal transport modeling to compute heat and mass transfer rates, expressions for optically thick media, such as the Rosseland approximation can be employed (Modest, 2003). Rosseland approximation is sometimes known as the diffusion approximation, as the radiative heat flux can be expressed as:

$$\mathbf{q} = -k_{\mathrm{R}} \nabla T \tag{6.14}$$

with a radiative conductivity:

$$k_{\mathrm{R}} = \frac{16\sigma T^3}{3\beta^{\mathrm{R}}} \tag{6.15}$$

Here, σ is the Stefan-Boltzmann constant, T is the temperature, and β_{R} is the Rosseland mean extinction coefficient. Thus, the heat-flux due to radiative transfer can be computed similar to a heat conduction problem with "radiative conductivity" strongly dependent on temperature. The Rosseland mean extinction coefficient is defined as:

$$\beta^{\mathrm{R}} = \frac{4\sigma T^3}{\pi D} \tag{6.16a}$$

$$D = \int_0^\infty \frac{\mathrm{d}I_{\mathrm{b}\lambda}}{\beta_\lambda^{\mathrm{tr}} \mathrm{d}T} \mathrm{d}\lambda \tag{6.16b}$$

Where, $\beta_\lambda^{\mathrm{tr}}$ is the spectral transport extinction coefficient, $I_{\mathrm{b}\lambda}$ is the spectral intensity of a blackbody given by Planck's law and T is the temperature. Particular attention must be given to applying Rosseland approximation near boundaries, because the model has been known to result in large errors when applied at boundaries (Modest, 2003).

6.6 Summary

The focus of this chapter was on identification procedures employed to infer transport scattering and absorption coefficient of sintered ceria discs and 3DOM packed bed from experimental data reported in Chapter 5. For the sintered ceria discs, directional-hemispherical transmittance could not be reliably measured. Further, low values of index of absorption of ceria could not be determined, posing significant challenges in the identification procedure. A combination of approximate solutions, Mie theory and Monte Carlo ray-tracing simulations were employed to estimate transport radiative properties. For the 3DOM ceria packed bed, identification procedure was greatly simplified because of the ability to measure directional-hemispherical transmittance, as a result of which, Monte Carlo ray-tracing simulations were employed to determine transport radiative properties with greater accuracy. From a radiative transfer theory perspective, it was shown that independent scattering hypothesis and Mie theory could

be applied to highly disorderly media such as the sintered ceria ceramics to estimate transport radiative properties with an accuracy that is acceptable for engineering heat transfer analysis.

Transport radiative properties of sintered ceria discs indicated that ceria is highly scattering even in the visible spectrum, suggesting significantly lower penetration of solar radiation. Based on the computations of the present work, smaller grain and pore sizes than currently used in the sintered discs can facilitate longer reach of the incident solar-radiation, especially in the visible spectrum. In the near-infrared, absorption coefficient was low, and attenuation was primarily by scattering. Effective scattering of near-infrared radiation promotes confinement of radiation within the cavity of a solar thermochemical reactor, as a result of which more uniform temperatures can be achieved during the reaction.

Transport scattering coefficient was shown to depend on the material morphology, and the absorption coefficient was only dependent on the volume fraction of bulk ceria (solid volume fraction). Thermochemical cycling of 3DOM ceria packed bed resulted in sintering of walls of the 3DOM structure, resulting in a higher transport scattering coefficient. Absorption coefficient of the 3DOM ceria packed bed after thermochemical cycling was not affected, as porosity only decreased by a small fraction, further confirming that scattering coefficient is independent of porosity, and only dependent on pore size and pore structure, where as absorption coefficient was only dependent on porosity, and independent of morphology.

Thermal transport characteristics of ceria structures in thermochemical reactors can be modeled by using approximate methods suitable for optically thick materials, such as the Rosseland approximation. Identified transport radiative properties can be used to model heat and mass transfer characteristics of ceria-based thermochemical reactors.

Chapter 7

Towards high temperature radiative characterization

The goal of this chapter is to shift focus from ambient temperature radiative characterization towards high temperature radiative characterization of materials encountered in thermochemical applications in particular, and metal oxides and ceramics in general. Phenomena that occur in ionic solids such as oxides at high temperatures that are responsible for absorption and emission of thermal radiation are presented. Methodology for determination of radiative quantities such as emittance, absorption coefficient, scattering coefficient and challenges associated with the techniques are reviewed. A proposed design which facilitates measurement of normal-emittance of materials at high temperatures is described and evaluated.

7.1 Physics of interaction of radiation at high temperatures with ceramic materials

At temperatures of interest in solar thermochemical applications, as well as ceramics processing, optical and radiative properties of materials show strongly coupled interaction of incident radiation with phonons. This interaction results in strong absorption of incident radiation, manifested as an increase in absorption coefficient from its value at room temperature, and a concomitant increase in emittance. Atoms or ions in a crystalline substance, such as ceramics used in solar thermochemical applications have modes of vibrations which are described according to quantum mechanical excitations called phonons. Two adjacent atoms or ions can vibrate in phase with each other in the same direction, which is representative of zero energy phonons. When adjacent atoms or ions vibrate out of phase with each other, motion in opposite directions results in high energy phonons. Description of phonons are similar to those of wave propagation according to electromagnetic theory, and indeed, phonons are referred to as optical phonons or acoustic phonons, depending on whether atomic or ionic vibrations are out of phase or in phase. In ionic compounds such as ceramics, optical phonons have a strong internal electric field in the form of a dipole moment, because of the movement of positive and negative ions out of phase with one another. In the presence of an external electromagnetic field such as infrared radiation, there is coupling of this dipole moment with the radiation. When two or more phonons simultaneously interact with an external electromagnetic field, the resulting interaction is referred to as multi-phonon absorption, because the phonons absorb energy from the electromagnetic field when the frequency (or, implicitly, wavelength of the incident electromagnetic field) is equal to the frequency of phonon vibration. Multi-phonon absorption is typically observed in

ionic solids at wavelengths above 6 μm (Henrich and Cox, 1996). Analysis of dielectric functions of phonon excitation by infrared radiation indicates that the reflectivity of the crystal will also reach very high values. Metal oxides and ionic solids have been shown to exhibit this behavior (Palik, 1997).

As a result of multi-phonon interaction, absorption and emission of infrared radiation by ionic solids at infrared wavelengths is very strong. Two processes, known as two-phonon and three-phonon difference processes are responsible for this behavior (Stolen, 1975). In a two-phonon difference process, absorption and emission at higher energy by two phonons occur which increases linearly with temperature, and for three-phonon difference processes, background absorption by other phonons are also observable, and absorption increases as the square of temperature, T^2 (Billard et al., 1980; Cabannes and Billard, 1986). This temperature dependence is explained by the fact that vibrations in ionic crystals are thermally excited, and at low temperatures, simply, inadequate number of phonons are available for absorption.

7.2 Background and challenges

Reacting media employed in solar thermochemical reactions, such as ceria, are directly irradiated by concentrated solar energy and achieve temperatures above 1000 K. Radiative properties of materials are dependent on temperature, in addition to radiation wavelength, composition and morphology. Establishing the dependence of temperature on radiative properties for non-metals is considerably more challenging than at ambient temperature. A limited number of studies reported measurements of normal-emittance (Sarou-Kanian et al., 2005; del Campo et al., 2011; Markham et al., 1990, 1993; Rozenbaum et al., 1999) or normal-hemispherical reflectance[1] (Baillis and Sacadura, 2002;

[1] It can be seen from the preceding discussion that materials such as ceramics become opaque at high temperature, causing very little radiant energy to be transmitted

Lopes et al., 2001).

In order to quantify radiative properties as a function of temperature, radiant energy emitted or reflected by a material must be measured as a function of temperature. Heating materials such as ceramics typically involve a 10 % conversion efficiency of heat transfer rate from a heat source to sensible heat, which is observed as a temperature change in the material. Infrared furnaces have been employed with some success for temperatures below 1000 – 1500 K. (Cabannes and Billard, 1987; Mital et al., 1996). One of the limitations of employing a furnace for radiative characterization is the lack of modulation in such measurements. Modulation, in this case, refers to isolating radiant energy emitted by the material from radiant energy emitted by the heat source, i.e. walls of the furnace. Furnace walls reach temperatures which cause infrared emission, which is difficult, if not impossible to isolate from infrared emission from the material being heated.

Laser heating has been suggested as an alternative, especially for measuring radiative properties of ceramics at high temperatures (del Campo et al., 2011; Markham et al., 1990, 1993; Rozenbaum et al., 1999). High power CO_2 lasers, typically in the range 200 – 500 W are used as the source of heating. CO_2 lasers offer the advantage of lines of emission at a single wavelength typically about 10 μm, which makes it relatively easier to isolate the source of heat from the measured emittance.

7.3 Design specifications

7.3.1 Heat sources

A schematic of the experimental design for measuring normal emittance is shown in Fig. 7.1. A Synrad firestar f201 CO_2 laser (# 1) coupled with a chiller with recirculating water (# 2), capable of approximately 250 W of laser power is the source of radiation.

Output power of the laser can be controlled in steps of 1 W using a micro-controller to facilitate variable heating rates of the ceramic sample. The wavelength of emission of CO_2 laser is 10.2 – 10.7 μm and the diameter of the beam is 4.5 mm. The source beam is split into two beams with a zinc selenide plate beam splitter (# 3) of 1" diameter. Reflectance and transmittance of the zinc selenide beam splitter are both approximately 50 % in the spectral range 7 – 14 μm. Based on the transmission and reflection data, the power from the source beam is expected to be split equally between the two beams that emerge from the beam splitter. Two gold mirrors (# 4a and # 4b) of 1" diameter are used to redirect the two beams on to either side of the sample holder. Gold mirrors were chosen because of high reflectivity of 97% in the spectral range 1 – 10 μm. The ceramic sample is placed in the sample holder (# 5) and is heated on opposite faces by two beams to minimize axial temperature gradients.

For normal-emittance measurements, radiant energy emitted by the hot sample at a given wavelength and temperature is normalized by the radiant energy emitted by a blackbody at the same wavelength and temperature:

$$\epsilon(T) = \frac{I(T)}{I_b(T)} \tag{7.1}$$

Here, ϵ refers to the spectral, directional emittance, $I(T)$ refers to the emitted radiative intensity of the hot sample and I_b refers to intensity emitted a blackbody at the same temperature as the hot sample. The spectral subscript, and the dependence on direction are omitted in the nomenclature for brevity. For normal-emittance measurements, only intensity in the near-normal direction is collected.

A Newport model 67032 blackbody source with a variable aperture wheel is used to normalize the radiant energy emitted by the hot sample for the normal-emittance measurements. The blackbody source serves as a calibrated source of infrared radiation, stable to $\pm$ 0.2 K. It has a cavity designed to have an emissivity 0.99 $\pm$ 0.01

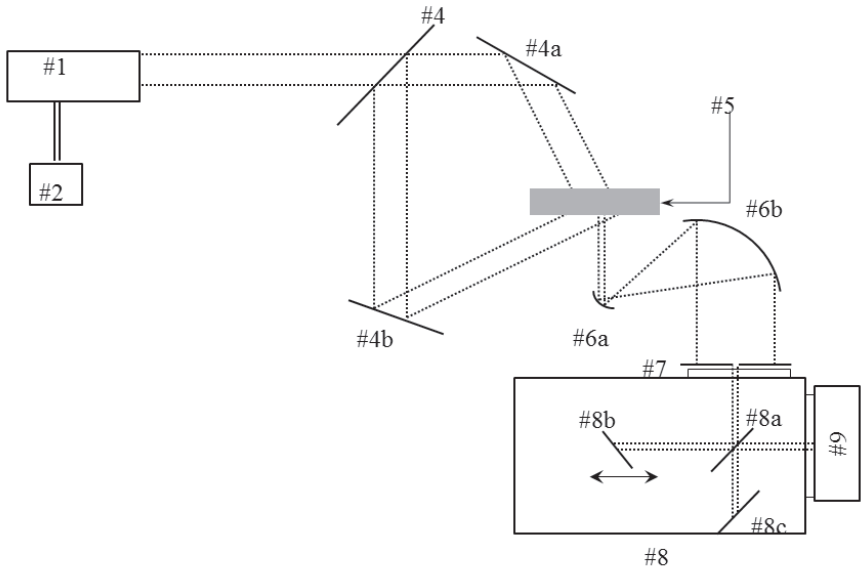

Figure 7.1: Schematic of experimental setup for measuring normal emittance of ceramic materials in the spectral range 0.7–10 μm and temperatures up to 1000 K.

% and is equipped with a resistive-heating element, and a type S thermocouple. An external micro-controller provides electric power to the resistive heating element. The blackbody source has a temperature range of 323 K to 1323 K, limiting the temperature range of normal-emittance measurements to a modest 1000 K. The blackbody cavity has a variable-diameter aperture wheel, which enables selection of the beam diameter of the infrared radiation leaving the blackbody cavity. For normal-emittance measurements, the specifications of a beam of radiant energy leaving the blackbody source must be identical to that of the sample. Parameters such as size and distance traveled by the emitted beam of radiation can be controlled in this setup to ensure accuracy of normal-emittance measurements.

7.3.2 Collection optics

A Newport MIR8025 Fourier transform infrared (FTIR) spectrometer (# 8 in Fig. 7.1) equipped with collection optics (# 6a, # 6b and # 7) and detectors (# 9) are used for measuring spectrally resolved emitted radiant energy from the hot-sample and the blackbody source. Approximately 84 % of the emitted radiant energy from a blackbody at 1000 K is in the spectral range of 2–10 μm, necessitating the use of an infrared radiometry system. The FTIR spectrometer operates on the principle of wave-interference. The FTIR spectrometer consists of interchangeable beam-splitters (8a) of either potassium bromide or calcium fluoride, sensitive in long (1.7–28 μm) and short-wave part (0.7–8.3 μm) of the infrared spectrum. Incident radiation from a source, in this case, emitted radiative energy of the hot sample or the blackbody source is split in to two beams. One beam is incident on a fixed gold mirror and the other beam on a moving gold mirror. The two beams then merge, and produce interference pattern because of phase-shifts on a silicon or InGaAs detector, sensitive the short-wave infrared spectrum (0.7–1.0 μm and 1.0–1.7 μm respectively), or liquid-nitrogen cooled mercury

cadmium telluride (MCT) detector, sensitive in the spectral range 2–17 μm. The FTIR spectrometer is equipped with data analysis software MIRMAT developed by Newport, which performs Fast Fourier Transform algorithm to extract spectral content of the interferogram. Thus, radiative energy as a function of wavelength can be measured.

In order to eliminate radiative intensity from directions other than the normal directions from reaching the detector, an optical collection system was designed by graduate student at the solar energy laboratory, Jeff Stamp. This system consists of two variable-diameter iris-diaphragms (# 7) which can be closed to limit the diameter of the emitted beam that reaches the FTIR, and two off-axis parabolic gold mirrors of effective focal lengths 25.4 mm (# 6a) and 190.5 mm (# 6b) to limit the divergence of the beam from the heated sample reaching the FTIR.

7.3.3 Sample holder

The sample holder (# 5 in Fig.7.1) is the most critical component of the normal-emittance setup. The purposes of the sample holder include:

1) providing mechanical support to a variety of sample geometries and dimensions.

2) enabling incidence of the beams from the CO_2 laser on opposite faces of the sample to minimize axial temperature gradients; optimal angle of incidence to minimize radial gradients, because angle of incidence of the beams affect the incident beam spot size on the sample.

3) insulating the hot sample from the surroundings for safety and to minimize conduction losses between the sample and the optical table.

4) maintaining the required atmosphere for preserving the composition of the ceramic sample at high temperatures. Recall that ceria has a tendency to form oxygen defects at high-temperatures. If composition of the hot sample is not preserved, measured normal-emittance cannot be considered representative of ceria of a given composition.

5) mounting and dismounting samples in the sample holder.

The sample holder was designed with these considerations and is shown in Fig. 7.2. It consists of an annular Inconel outer casing (# 1). Inconel was chosen because of its slightly lower coefficient of thermal expansion (12.6×10^{-6} m/m K) than stainless steel (17.3×10^{-6} m/m K). The casing is designed to be made of two halves to facilitate mounting and dismounting of samples and bolted together by a bolt assembly shown in Fig. 7.2c, consisting of bolts (# 1b), washers (# 1c) and a layer of insulating felt (# 1d). Axial through-holes are drilled every angular intervals in the casing to act as channels for water cooling of the entire casing. Two half-annular rings of alumina insulation (# 2) of porosity 50 % is cemented to the Inconel casing by thermally-insulating alumina cement. Note that the required atmosphere for maintaining the composition of the ceramic sample is achieved by providing a stream of low-partial pressure oxygen to maintain an oxygen-rich atmosphere to prevent reduction of the ceramic sample, or an inert gas to maintain a reducing atmosphere. To prevent oxygen or inert gas saturating the pores of the insulation, a second layer of dense insulation is affixed to the sample (# 3). The lower half of the dense insulation has a thin groove for the ceramic sample (# 4) to rest. The dimensions of the groove were chosen to minimize conduction losses due to large contact area between the supporting insulation and the hot sample. Thin spacers made with dense alumina ceramics are placed in the gap between the upper half of the insulation and the hot sample to provide additional mechanical support without incurring heat loss by conduction.

The casing and insulation layers have gas channels (# 5) cut in them to facilitate passage of oxygen or inert gas through the sample holder on to the sample, to maintain either an oxidizing, reducing or inert atmosphere to maintain composition of the

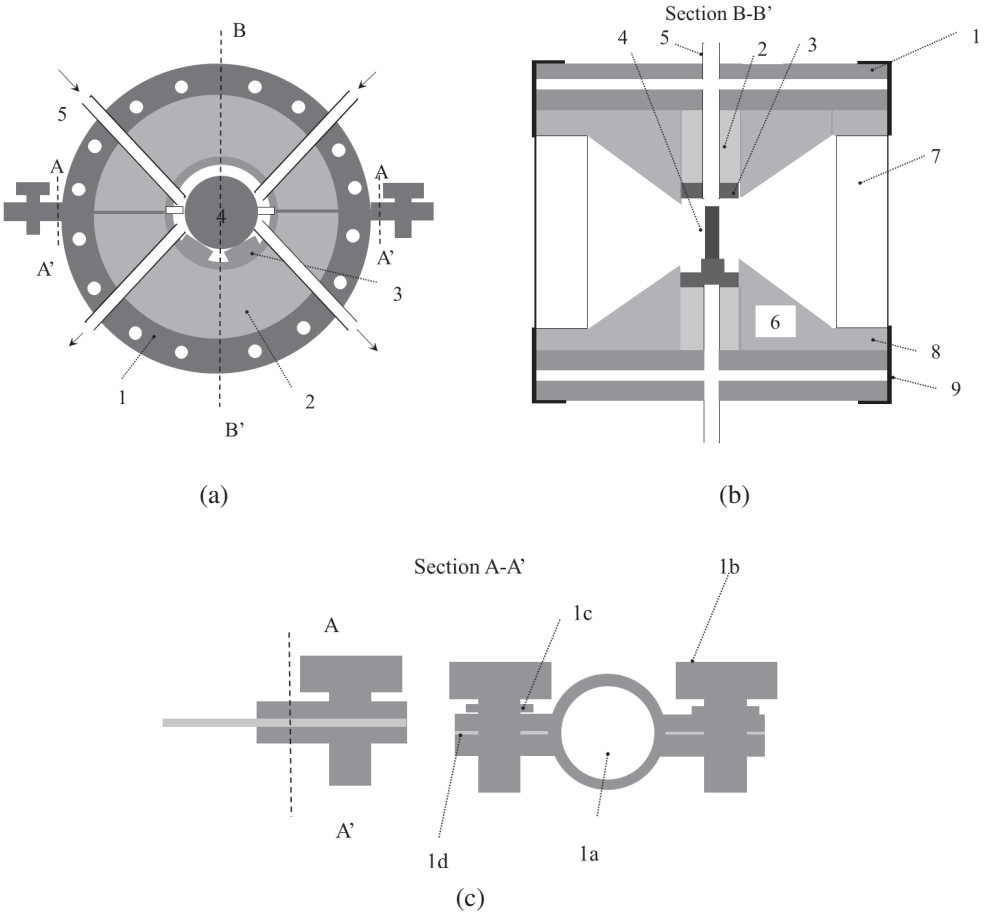

Figure 7.2: A schematic of the sample holder.

ceramic sample at high temperature. The sample temperature is measured by a thermocouple, inserted through the recess (# 1a).

Two cones of insulation made with dense ceramics (# 6) are placed on opposite faces of the sample. They improve directional characteristics of the beam emitted by the sample and collected by collection optics in the normal-emittance measurements. Two zinc selenide windows of diameter 1" coated with anti-reflection coating (# 7), with a transmittance of 98 % in the spectral range 8–14 μm are used to hermetically seal the assembly, while providing optical access to the incident laser beam and emitted radiant energy from the sample. The windows are supported by two window supports (# 8) made of Inconel and fastened to the casing of the sample holder by two end-caps (# 9).

7.4 Evaluation of design

Several aspects of the design were evaluated prior to design of the setup, such as estimating laser power required for heating the sample to 1000 K, temperature distribution in the sample holder to design the insulation and optical design to ensure optimal incidence of laser beam to minimize axial and radial temperature gradients, and ensure a small angle of collection in the near-normal direction of the radiant energy emitted by the ceramic sample. These parameters are evaluated in this section.

A simple energy balance model was developed to estimate heat losses in the measurement setup to ensure that the laser provides adequate power for heating the sample. A schematic of the energy balance is shown in Fig. 7.3. Three different loss terms are considered: (a) convective loss from the sample to its surroundings, $\dot{Q}_{\text{conv}}$; re-radiation "losses" [2] from the sample, $\dot{Q}_{\text{re-rad}}$; and (c) conduction losses between the sample and

[2] This term actually represents the amount of radiative energy leaving the sample due to emission, and is collected by the measurement system to obtain normal-emittance.

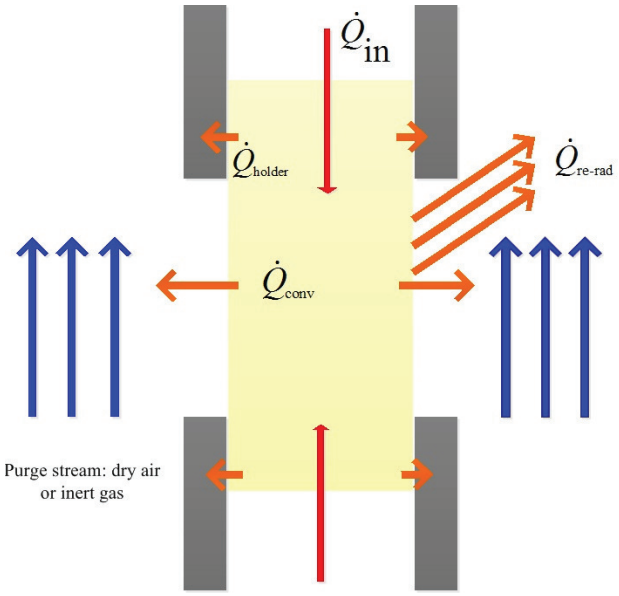

Figure 7.3: Energy balance for the heated sample showing heat loss terms

the surface of the sample holder, $\dot{Q}_{\text{holder}}$, which is modeled as axial heat conduction through a slab at a temperature equal to ambient temperature. In reality, the sample holder will be at a temperature higher than ambient temperature, but setting the holder temperature equal to T_∞ allows one to estimate the conduction loss in an extreme scenario.

The energy balance for the ceramic sample with the modeled heat loss terms becomes:

$$\dot{W}_{\text{in}} = \dot{E}_{\text{storage}} + \dot{Q}_{\text{conv}} + \dot{Q}_{\text{re-rad}} + \dot{Q}_{\text{holder}} \tag{7.2a}$$

$$\dot{E}_{\text{storage}} = \rho V c \frac{\mathrm{d}T}{\mathrm{d}t} \tag{7.2b}$$

Table 7.1: Heat transfer losses (W) and power input (W) for sample heating listed for various sample temperatures

T (K)	$\dot{Q}_{\text{conv}}$	$\dot{Q}_{\text{re-rad}}$	$\dot{Q}_{\text{holder}}$	$\dot{E}_{\text{storage}}$	$\dot{W}_{\text{in}}$
600	9.4	4.1	45	20.8	79.3
900	18.8	21.9	90	41.7	172.4
1200	28.2	69.9	135	62.5	295.7
1500	37.6	171	180	83.4	472.1
1800	47.1	355	225	104.2	731.4
2100	56.5	657.9	270	125.14	1109.6

$$\dot{Q}_{\text{conv}} = hA_{\text{s}}(T - T_{\infty}) \tag{7.2c}$$

$$\dot{Q}_{\text{re-rad}} = \epsilon_{\text{cer}} A_{\text{s}}(T^4 - T_{\infty}^4) \tag{7.2d}$$

$$\dot{Q}_{\text{cond}} = -k_{\text{holder}} \frac{\mathrm{d}T}{\mathrm{d}x} \tag{7.2e}$$

In the above equation, $\dot{W}_{\text{in}}$ refers to the power input from the laser and $\dot{E}_{\text{storage}}$ refers to rate of increase of internal energy of the sample. The sample temperature is T, density is ρ and thermal capacity is c. Parameters of the calculation are the emissivity of the ceramic sample, ϵ_{cer}, heat transfer coefficient for convective loss, h, and thermal conductivity of the sample holder k_{holder}. A worst-case calculation was performed with selected values of these parameters: emissivity of the ceramic sample, ϵ_{cer} = 0.95, heat transfer coefficient h = 50 Wm^{-2} K^{-1} representative of high-speed purge gas flow, thermal conductivity of the sample holder k_{holder} = 30 Wm^{-1} K^{-1}, which is representative of thermal conductivity of Inconel, and sample diameter of 5 mm and thickness 20 mm. Material properties were obtained for bulk ceria. Table 7.1 shows the power input from the laser required for heating for various sample temperatures, together with the various loss terms. Based on this worst-case calculation, it is expected that 200 W of laser power is sufficient to reach a sample temperature of 1000 K.

Temperature distribution in the sample holder was estimated approximately by assuming one-dimensional radial conduction heat transfer from the sample to the Inconel casing (shown in Fig. 7.2). Inner and outer diameters of the Inconel casing in the design are 2" and 3", respectively. The inner diameter of the porous insulation is 0.39", and that of the dense insulation is 0.315". Thermal conductivity of the materials were retrieved from the thermophysical properties data using Engineering Equation Solver (EES) software. Computations were carried out in EES software for a worst-case sample temperature of 2000 K, without any water cooling. A casing temperature of 620 K was obtained for a sample temperature of 2000 K, indicating that water cooling was necessary to allow safe-handling of the Inconel casing. A more accurate two-dimensional axisymmetric model was also developed using ANSYS-CFX thermal modeling software to account for re-radiation from the sample and the insulation, and allow for predicting temperature distribution for various mass flow rate of cooling water.

Optical design of the collection optics was done by Jeff Stamp, researcher at solar energy laboratory using a ray-tracing program that computes the path of rays emitted by a source (such as the heated sample), and reflected by off-axis parabolic mirrors of focal length 25.4 mm and 190.5 mm, and iris diaphragms with adjustable aperture diameters to estimate divergence of the beam entering the FTIR spectrometer and to ensure optimal incidence of the laser beam. Based on the ray-tracing calculation, the width of the sample holder was adjusted such that the incidence beam is of diameter 7 mm, and radiant energy emitted by the sample is collected from a circular area of diameter 5 mm. Based on this optical design, it is expected that the radial temperature gradients in the measurement area are minimal, and divergence of the emitted beam of radiation is less than 1 °.

7.5 Summary

An experimental facility to measure normal-emittance of metal oxide (ceramic) materials encountered in solar thermochemical reactors at high temperature was designed and evaluated. The facility consists of CO_2 laser to heat ceramic samples up to a temperature of 1000 K. Normal-emittance in the spectral range 0.7–2.0 μm can be measured using a FTIR spectrometer and collection optics. The design was evaluated to ensure optimal incidence of the laser beam to minimize axial and radial temperature gradients in the ceramic sample, adequate laser power to reach sample temperature of 1000 K, and adequate insulation between the sample and surroundings to allow safe-handling temperatures of the sample holder.

This chapter also summarizes some methods that can be used to infer absorption and emission characteristics of ionic solids such as those used in thermochemical applications. Multi-phonon interaction with infrared radiation, resulting in increased absorption and emission with temperature.

Chapter 8

Conclusions and outlook

8.1 Summary

This dissertation focused on development of methodology to infer radiative properties of porous heterogeneous materials encountered in solar thermochemical reactors, and documented transport radiative properties of porous cerium dioxide at ambient temperature. Absorption and scattering of solar radiation by heterogeneous reacting media govern heat and mass transfer phenomena in solar thermochemical reactors. The scope of the present work was radiative characterization of porous ceria as a function of wavelength and morphology, and development of experimental facility for radiative characterization of reacting media at high temperatures. Experimental setups for measuring spectral transmittance and reflectance of materials at ambient temperature were developed. A Monte Carlo ray-tracing method that infers transport scattering coefficient and absorption coefficient from measured transmittance and reflectance was also developed. An experimental facility with CO_2 laser heating coupled with a FTIR spectrometer was designed to facilitate measurement of normal-emittance at temperatures

up to 1000 K. Morphology-dependent transport radiative properties of ceria were considered for radiative characterization at ambient temperature, and a non-scattering ceria thin film of thickness 2 μm deposited on a Yttria Stabilized Zirconia substrate was also considered to infer absorption spectrum of ceria.

Ceria absorbed incident radiation strongly up to a wavelength of 0.45 μm and measured transmittance of non-scattering thin film in this spectral range was noisy because of complete attenuation of incident radiation by absorption. After a wavelength of 0.5 μm, absorption of radiation by ceria was weak, and transmittance of the thin film reached a constant mean value with oscillations imposed due to wave interference effects. Absorption characteristics of ceria are consistent with electronic absorption of short-wave electromagnetic radiation, similar to many ionic solids with comparable optical band gaps. A methodology to infer index of refraction of semi-transparent thin films was presented. This methodology can be used to measure transmittance spectra of thin films of materials with optical band gap corresponding to UV-VIS-NIR absorption of electromagnetic radiation. Analysis of wave-interference that occurs in thin films can then be employed to obtain the index of refraction.

Scattering characteristics of semi-transparent materials were found to depend strongly on pore-morphology. The three-dimensionally organized macroporous morphology facilitated longer distance of travel due to weaker scattering than randomly arranged sintered grains, even though pore and particle sizes of the two morphologies were comparable. Scattering was only weakly dependent on porosity. Absorption coefficient was not affected as a result of morphology, as revealed by absorption coefficient of three different morphologies. Studies in the literature indicate that absorption of electromagnetic radiation by optically soft materials is only dependent on porosity. In the present work, this result could not be verified because of approximate procedure involved in identification of absorption coefficient for one of the morphologies considered.

Inferred radiative properties can be used to model thermal transfer phenomena in solar thermochemical reactors to compute production of H_2 and CO for a given morphology of ceria, and in other combined heat transfer problems. Radiative characterization of two morphologies of ceria indicate that for the typical particle and pore sizes considered in thermochemical applications, strong scattering leads to large optical thickness, as a result of which, models applicable for optically thick media, such as the Rosseland approximation can be used for modeling the radiative heat flux in these combined heat transfer problems.

Large values of scattering coefficient of the ceria ceramics were obtained for typical particle and pore sizes of reacting media considered in thermochemical reactors. This indicates that incident solar radiation travels only a short-distance in the material, and effective absorption of solar radiation can be achieved by either decreasing the grain and pore-sizes to mitigate the effect of intense scattering, or by introducing free electrons in the lattice structure of ceria which absorb short-wave visible radiation effectively. An optimal reactor design with thin reacting elements of thickness on the order of few hundred microns will minimize temperature gradients and allow for uniform absorption of incident solar radiation. Effective scattering of near-infrared radiation indicates that the ceria structures considered for solar thermochemical reactors will enhance absorption and confinement of the near-infrared radiation.

8.2 Limitations and future work

While the present dissertation has fulfilled its scope and objectives, it suffers from a few limitations. Perhaps the most important limitation of the present work is that Monte Carlo ray-tracing method, applied to infer transport scattering coefficient and absorption coefficient, fails in the spectral range where incident radiation is absorbed

strongly in the medium at distances comparable to radiation wavelengths. Ray optics, which is at the foundation of the Monte Carlo ray-tracing method becomes inapplicable in this situation. Theoretical approaches, such as Mie theory also become of limited application, and inferring radiative properties in this spectral range remains a challenge.

For optically thick materials, the present study circumvented experimental difficulties associated with low transmittance, by developing an experimental setup with a higher dynamic range than commercial spectrometers. However, the identification procedure to infer radiative properties from measurements incurs a high computational cost because of long simulation times involved with Monte Carlo ray-tracing procedure. Especially for approximate engineering analysis, high computational cost due to Monte Carlo ray-tracing method is unjustified.

Lastly, the scope of the present study was limited to radiative characterization at ambient temperature and development of experimental facility for radiative characterization at high temperature. Transport radiative properties of ceria at ambient temperature are expected to change with temperature. A trend that is consistently reported in the literature is that both absorption coefficient and normal-emittance of ceramic materials increase with temperature. Further, solar thermochemical cycles occur between temperatures of 1000 to 1500 K suggesting that establishing temperature dependence of radiative properties is significant for solar thermochemical process modeling. However, the present research work was limited only to radiative characterization at ambient temperature.

From a radiative transfer standpoint, development of a hybrid Monte Carlo method that reduces the computational cost of Monte Carlo technique applied to optically thick and highly scattering dispersed materials is suggested, especially based on the experiences of the author of the present work with the Monte Carlo technique. Coupling of Monte Carlo technique with other methods can also enable identification of radiative

properties in the spectral ranges where absorption of radiation is strong and ray optics become of limited applicability.

Radiative characterization of ceria at high temperature was beyond the scope of the present work. Radiative properties of materials at high temperatures was too broad to be included as a part of the present work both from perspective of fundamental radiative transfer theory and energetic interactions that occur in materials at high temperatures, as well as from the perspective of development of numerical methods to investigate radiative properties at high temperatures. Future work on ceria based thermochemical cycles must address this limitation and establish temperature dependence of radiative properties. To this end, the design of the experimental facility to determine radiative properties of materials at high temperature is one of the contributions of this work.

One of the unexpected outcomes of the present work was the possibility of obtaining index of refraction and absorption of materials, and in particular, ceria. Transmittance of thin films can be used to determine optical constants based on analysis of wave interference pattern by observing phase difference that causes constructive and destructive interference. Radiative properties of optically soft materials ($|m-1| < 1$) such as highly-porous ceria, obtained using the methods developed as a part of the present work, can be used to infer index of absorption, especially in the spectral ranges of weak absorption.

References

(2008). *Minerals Yearbook Volume 1: Metals and Minerals*. Geological Survey.

Abanades, S. and Flamant, G. (2006). Thermochemical hydrogen production from a two-step solar-driven water-splitting cycle based on cerium oxides. *Solar Energy*, 80(12):1611–1623.

Agarwal, B. and Mengüç, M. (1991). Forward and inverse analysis of single and multiple scattering of collimated radiation in an axisymmetric system. *International Journal of Heat and Mass Transfer*, 34:633–647.

Argento, C. and Bouvard, D. (1996). A ray tracing method for evaluating the radiative heat transfer in porous media. *International Journal of Heat and Mass Transfer*, 39(15):3175–3180.

Bahador, M. and Sundn, B. (2008). Investigation on the effects of fly ash particles on the thermal radiation in biomass fired boilers. *International Journal of Heat and Mass Transfer*, 51(910):2411 – 2417.

Baillis, D., Arduini-Schuster, M., and Sacadura, J. (2002). Identification of spectral radiative properties of polyurethane foam from hemispherical and bi-directional transmittance and reflectance measurements. *Journal of Quantitative Spectroscopy and Radiative Transfer*, 73(2–5):297–306.

Baillis, D., Pilon, L., Randrianalisoa, H., Gomez, R., and Viskanta, R. (2004). Measurements of radiation characteristics of fused quartz containing bubbles. *Journal of the Optical Society of America A—Optics, Image, Science, and Vision*, 21(1):149–159.

Baillis, D. and Sacadura, J. (2000). Thermal radiation properties of dispersed media: theoretical prediction and experimental characterization. *Journal of Quantitative Spectroscopy and Radiative Transfer*, 67:327–363.

Baillis, D. and Sacadura, J.-F. (2002). Directional spectral emittance of a packed bed: Influence of the temperature gradient in the medium. *Journal of Heat Transfer*, 124(5):904–911.

Balakrishnan, G., Sundari, S., Kuppusami, P., Mohan, P., Srinivasan, M., Mohandas, E., Ganesan, V., and Sastikumar, D. (2011). A study of microstructural and optical properties of nanocrystalline ceria thin films prepared by pulsed laser deposition. *Thin Solid Films*, 519(8):2520–2526.

Barabás, M. (1987). Scattering of a plane wave by a radially stratified tilted cylinder. *Journal of the Optical Society of America A—Optics, Image, Science, and Vision*, 4(12):2240–2248.

Barreca, D., Bruno, G., Gasparotto, A., Losurdo, M., and Tondello, E. (2003). Nanostructure and optical properties of ceo¡ sub¿ 2¡/sub¿ thin films obtained by plasma-enhanced chemical vapor deposition. *Materials Science and Engineering: C*, 23(6):1013–1016.

Beder, E., Bass, C., and Shackleford, W. (1971). Transmissivity and Absorption of Fused Quartz Between 0.22 μ and 3.5 μ from Room Temperature to 1500 C. *Applied Optics*, 10(10):2263–2268.

Billard, D., Gervais, F., and Piriou, B. (1980). Far-infrared absorption in al2o3 and mgo. *International Journal of Infrared and Millimeter Waves*, 1:641–647.

Bohren, C. and Huffman, D. (1998). *Absorption and Scattering of Light by Small Particles*. Wiley-VCH.

Born, M. and Wolf, E. (1999). *Principles of optics: electromagnetic theory of propagation, interference and diffraction of light*. Cambridge University Press.

Cabannes, F. and Billard, D. (1986). Measurement of infrared absorption of some oxides in connection with the radiative transfer in porous and fibrous materials. *International Journal of Thermophysics*, 8:0067–0118.

Cabannes, F. and Billard, D. (1987). Measurement of infrared absorption of some oxides in connection with the radiative transfer in porous and fibrous materials. *International Journal of Thermophysics*, 8:97–118. 10.1007/BF00503227.

Chueh, W. and Haile, S. (2009). Ceria as a thermochemical reaction medium for selectively generating syngas or methane from h_2o and co_2. *ChemSusChem*, 2(8):735–739.

Chueh, W. and Haile, S. (2010). A thermochemical study of ceria: exploiting an old material for new modes of energy conversion and co_2 mitigation. 368(1923):3269.

Chueh, W. C., Falter, C., Abbott, M., Scipio, D., Furler, P., Haile, S. M., and Steinfeld, A. (2010). High-flux solar-driven thermochemical dissociation of co2 and h2o using nonstoichiometric ceria. *Science*, 330(6012):1797–1801.

Coquard, R. and Baillis, D. (2004). Radiative characteristics of opaque spherical particles beds: a new method of prediction. *Journal of Thermophysics and Heat Transfer*, 18(2):178–186.

Coquard, R. and Baillis, D. (2006). Radiative properties of dense fibrous medium containing fibers in the geometric limit. *Journal of Heat Transfer—Transactions of the ASME*, 128(10):1022–1030.

Coray, P., Lipiński, W., and Steinfeld, A. (2010). Experimental and Numerical Determination of Thermal Radiative Properties of ZnO Particulate Media. *Journal of Heat Transfer—Transactions of the ASME*, 132:012701.

del Campo, L., De Sousa Meneses, D., Blin, A., Rousseau, B., Vron, E., Balat-Pichelin, M., and Echegut, P. (2011). High-temperature radiative properties of an yttria-stabilized hafnia ceramic. *Journal of the American Ceramic Society*, 94(6):1859–1864.

Di Quarto, F., Sunseri, C., Piazza, S., and Romano, M. C. (1997). Semiempirical correlation between optical band gap values of oxides and the difference of electronegativity of the elements. its importance for a quantitative use of photocurrent spectroscopy in corrosion studies. *The Journal of Physical Chemistry B*, 101(14):2519–2525.

Dombrovsky, L. (2012b). The use of transport approximation and diffusion-based models in radiative transfer calculations. *Computational Thermal Sciences*, 004(4):297–315.

Dombrovsky, L. (July 17, 2012a). Note-k35nn. Email communication.

Dombrovsky, L. and Baillis, D. (2010). *Thermal Radiation in Disperse Systems: An Engineering Approach*. Begell House.

Dombrovsky, L., Lallich, S., Enguehard, F., and Baillis, D. (2010). An effect of "scattering by absorption" observed in near-infrared properties of nanoporous silica. *Journal of Applied Physics*, 107:083106–1–9.

Dombrovsky, L., Randrianalisoa, J., and Baillis, D. (2006). Modified two-flux approximation for identification of radiative properties of absorbing and scattering media from directional-hemispherical measurements. *Journal of the Optical Society of America A—Optics, Image, Science, and Vision*, 23(1):91–98.

Dombrovsky, L., Randrianalisoa, J., Baillis, D., and Pilon, L. (2005). Use of mie theory to analyze experimental data to identify infrared properties of fused quartz containing bubbles. *Applied Optics*, 44(33):7021–7031.

Dombrovsky, L., Tagne, H., Baillis, D., and Gremillard, L. (2007). Near-infrared radiative properties of porous zirconia ceramics. *Infrared Physics & Technology*, 51(1):44–53.

Dombrovsky, L. A., Ganesan, K., and Lipiński, W. (2012). Combined two-flux approximation and monte carlo model for identification of radiative properties of highly scattering dispersed materials. *Computational Thermal Sciences*, 004(4):365 – 378.

Dombrovsky, L. A., Rousseau, B., Echegut, P., Randrianalisoa, J. H., and Baillis, D. (2011). High temperature infrared properties of ysz electrolyte ceramics for sofcs: Experimental determination and theoretical modeling. *Journal of the American Ceramic Society*, 94(12):4310–4316.

Eldridge, J. and Spuckler, C. (2008). Determination of scattering and absorption coefficients for plasma-sprayed yttria-stabilized zirconia thermal barrier coatings. *Journal of the American Ceramic Society*, 91(5):1603–1611.

Fangxin, L., Chengyun, W., Qingde, S., Tianpeng, Z., and Guiwen, Z. (1997). Optical properties of nanocrystalline ceria. *Applied optics*, 36(13):2796–2798.

Farmer, J. and Howell, J. (1994). Hybrid monte carlo/diffusion methods for enhanced solution of radiative transfer in optically thick nongray media. *ASME-PUBLICATIONS-HTD*, 276:203–203.

Haussener, S., Lipiński, W., Petrasch, J., Wyss, P., and Steinfeld, A. (2009). Tomographic characterization of a semitransparent-particle packed bed and determination of its thermal radiative properties. *Journal of Heat Transfer—Transactions of the ASME*, 131(7):072701.

Hendricks, T. J. and Howell, J. R. (1996). Absorption/scattering coefficients and scattering phase functions in reticulated porous ceramics. *Journal of Heat Transfer—Transactions of the ASME*, 118(1):79–87.

Henrich, V. and Cox, P. (1996). *The surface science of metal oxides*. Cambridge University Press.

Hespel, L., Mainguy, S., and Greffet, J.-J. (2003). Radiative properties of scattering and absorbing dense media: theory and experimental study. *Journal of Quantitative Spectroscopy and Radiative Transfer*, 77:193–210.

Howell, J. (1998). The monte carlo method in radiative heat transfer. *Journal of Heat Transfer—Transactions of the ASME*, 120:547–560.

Jäger, K., Lipinski, W., Katzgraber, H., and Steinfeld, A. (2009). Determination of thermal radiative properties of packed-bed media containing a mixture of polydispersed particles. *International Journal of Thermal Sciences*, 48(8):1510–1516.

Kahnert, F. M. (2003). Numerical methods in electromagnetic scattering theory. *Journal of Quantitative Spectroscopy and Radiative Transfer*, 7980:775 – 824.

Kai, L. and D'lessio, A. (1995). Finely stratified cylinder model for radially inhomogeneous cylinders normally irradiated by electromagnetic plane waves. *Applied Optics*, 34(24):5520–5530.

Kamiuto, K. (1988). The geometrical optics approximation to the radiative properties of a large absorbing sphere. *Journal of Quantitative Spectroscopy and Radiative Transfer*, 39(6):435 – 440.

Kanakaraju, S., Mohan, S., and Sood, A. (1997). Optical and structural properties of reactive ion beam sputter deposited ceo¡ sub¿ 2¡/sub¿ films. *Thin Solid Films*, 305(1):191–195.

Keller, J. (1962). Wave propagation in random media. *Proceedings of Symposia in Applied Mathematics*, 13:227–246.

Kokhanovsky, A. (2003). Optical properties of bubbles. *Journal of Optics A: Pure and Applied Optics*, 5:47.

Köylü, U. O. and Faeth, G. M. (1993). Radiative properties of flame-generated soot. *Journal of Heat Transfer*, 115(2):409–417.

Lallich, S., Enguehard, F., and Baillis, D. (2009). Experimental Determination and Modeling of the Radiative Properties of Silica Nanoporous Matrices. *Journal of Heat Transfer*, 131:082701.

Lapp, J., Davidson, J., and Lipiński, W. (2011). Efficiency of two-step solar thermochemical non-stoichiometric redox cycles with heat recovery. *Energy*, 37:591 – 600.

Liang, Z., Chueh, W., Haile, S., Ganesan, K., and Lipiński, W. (2011). Experimental determination of transmittance of porous cerium dioxide media in the spectral range 300–1,100 nm. *Experimental Heat Transfer*, 24:285–299.

Lipiński, W., Guillot, E., Olalde, G., and Steinfeld, A. (2008). Transmittance enhancement of packed-bed particulate media. *Experimental Heat Transfer*, 21:73–82.

Lopes, R., Moura, L., Baillis, D., and Sacadura, J.-F. (2001). Directional spectral emittance of a packed bed: correlation between theoretical prediction and experimental data. *Journal of Heat Transfer—Transactions of the ASME*, 123:240–248.

Loretz, M., Coquard, R., Baillis, D., and Maire, E. (2008). Metallic foams: Radiative properties/comparison between different models. *Journal of Quantitative Spectroscopy and Radiative Transfer*, 109(1):16 – 27.

Manara, J., Arduini-Schuster, M., Rätzer-Scheibe, H., and Schulz, U. (2009). Infrared-optical properties and heat transfer coefficients of semitransparent thermal barrier coatings. *Surface and Coatings Technology*, 203(8):1059–1068.

Manara, J., Caps, R., Raether, F., and Fricke, J. (1999). Characterization of the pore structure of alumina ceramics by diffuse radiation propagation in the near infrared. *Optics Communications*, 168(1–4):237–250.

Manickavasagam, S. and Mengüç, M. (1993). Effective optical properties of pulverized coal particles determined from FT-IR spectrometer experiments. *Energy & Fuels*, 7(6):860–869.

Marabelli, F. and Wachter, P. (1987). Covalent insulator ceo2: Optical reflectivity measurements. *Phys. Rev. B*, 36:1238–1243.

Markham, J. R., Kinsella, K., Carangelo, R. M., Brouillette, C. R., Carangelo, M. D., Best, P. E., and Solomon, P. R. (1993). Bench top fourier transform infrared based instrument for simultaneously measuring surface spectral emittance and temperature. *Review of Scientific Instruments*, 64(9):2515–2522.

Markham, J. R., Solomon, P. R., and Best, P. E. (1990). An ft-ir based instrument for measuring spectral emittance of material at high temperature. *Review of Scientific Instruments*, 61(12):3700–3708.

Mengüç, M., Manickavasagam, S., and D'Sa, D. A. (1994). Determination of radiative properties of pulverized coal particles from experiments. *Fuel*, 73(4):613 – 625.

Mishchenko, M. I. (2006). Far-field approximation in electromagnetic scattering. *Journal of Quantitative Spectroscopy and Radiative Transfer*, 100(13):268 – 276.

Mishchenko, M. I., Tishkovets, V. P., Travis, L. D., Cairns, B., Dlugach, J. M., Liu, L., Rosenbush, V. K., and Kiselev, N. (2011). Electromagnetic scattering by a morphologically complex object: Fundamental concepts and common misconceptions. *Journal of Quantitative Spectroscopy and Radiative Transfer*, 112:671–692.

Mital, R., Gore, J., and Viskanta, R. (1996). Measurements of radiative properties of cellular ceramics at high temperatures. *Journal of Thermophysics and Heat Transfer*, 10(1):33–38.

Modest, M. (2003). *Radiative Heat Transfer*. Academic Press, San Diego, second edition.

Moore, T. J., Cundick, D. P., Jones, M. R., Tree, D. R., Maynes, R. D., and Baxter, L. L. (2011a). In situ measurements of the spectral emittance of coal ash deposits. *Journal of Quantitative Spectroscopy and Radiative Transfer*, 112(12):1978 – 1986.

Moore, T. J., Jones, M. R., Tree, D. R., Maynes, R. D., and Baxter, L. L. (2011b). An experimental method for making spectral emittance and surface temperature measurements of opaque surfaces. *Journal of Quantitative Spectroscopy and Radiative Transfer*, 112(7):1191 – 1196.

Nicolau, V., Raynaud, M., and Sacadura, J. (1994). Spectral radiative properties identification of fiber insulating materials. *International Journal of Heat and Mass Transfer*, 37:311–324.

Oh, T. (December 14, 2010). Email communication.

Oh, T., Tokpanov, Y., Hao, Y., Jung, W., and Haile, S. (2012). Determination of optical and microstructural parameters of ceria films. *Journal of Applied Physics*, 112:103535–1–10.

Özer, N. (2001). Optical properties and electrochromic characterization of sol-gel deposited ceria films. *Solar Energy Materials & Solar Cells*, 68:391–400.

Palik, E. (1997). *Handbook of Optical Constants of Solids, Five-Volume Set: Handbook of Thermo-Optic Coefficients of Optical Materials with Applications*. Academic Press.

Patsalas, P., Logothetidis, S., and Metaxa, C. (2002). Optical performance of nanocrystalline transparent ceria films. *Applied Physics Letters*, 81:466–468.

Penndorf, R. B. (1962). Scattering and extinction coefficients for small absorbing and nonabsorbing aerosols. *Journal of the Optical Society of America*, 52(8):896–902.

Petkovich, N., Rudisill, S., Venstrom, L., Boman, D., Davidson, J., and Stein, A. (2011). Control of heterogeneity in nanostructured ce1–x zr x o2 binary oxides for

enhanced thermal stability and water splitting activity. *The Journal of Physical Chemistry C*, 115(43):21022–21033.

Petrasch, J., Wyss, P., and Steinfeld, A. (2007). Tomography-based monte carlo determination of radiative properties of reticulate porous ceramics. *Journal of Quantitative Spectroscopy and Radiative Transfer*, 105(2):180–197.

Randrianalisoa, J. and Baillis, D. (2010). Radiative properties of densely packed spheres in semitransparent media: A new geometric optics approach. *Journal of Quantitative Spectroscopy and Radiative Transfer*, 111(10):1372 – 1388.

Reader, J., Sansonetti, C., and Bridges, J. M. (1996). Irradiances of spectral lines in mercury pencil lamps. *Applied Optics*, 35:78–83.

Rousseau, B., de Sousa Meneses, D., Echegut, P., Di Michiel, M., and Thovert, J. (2007). Prediction of the thermal radiative properties of an x-ray μ-tomographied porous silica glass. *Applied Optics*, 46(20):4266–4276.

Rozenbaum, O., Meneses, D., Auger, Y., Chermanne, S., and Echegut, P. (1999). A spectroscopic method to measure the spectral emissivity of semi-transparent materials up to high temperature. *Review of Scientific instruments*, 70:4020.

S. Jeon, S.N. Park, Y. S. Y. J. H. C. P. and Lee, G. (2010). Simultaneous measurement of emittance, transmittance, and reflectance of semitransparent materials at elevated temperature. *Optics Letters*, 35(23):4015–4017.

Sacadura, J. (2011). Thermal radiative properties of complex media: Theoretical prediction versus experimental identification. *Heat Transfer Engineering*, 32(9):754–770.

Sarou-Kanian, V., Rifflet, J., and Millot, F. (2005). Ir radiative properties of solid and liquid alumina: Effects of temperature and gaseous environment. *International Journal of Thermophysics*, 26:1263–1275. 10.1007/s10765-005-6725-5.

Siegel, R. and Howell, J. (2003). *Thermal Radiation Heat Transfer*. Taylor and Francis, New York, fourth edition.

Singh, B. and Kaviany, M. (1992). Modelling radiative heat transfer in packed beds. *International Journal of Heat and Mass Transfer*, 35(6):1397–1405.

Stein, A., Li, F., and Denny, N. (2007). Morphological control in colloidal crystal templating of inverse opals, hierarchical structures, and shaped particles. *Chemistry of Materials*, 20(3):649–666.

Steinfeld, A. (2005). Solar thermochemical production of hydrogen—-a review. *Solar Energy*, 78(5):603–615.

Stolen, R. H. (1975). Temperature dependence of far-infrared absorption in gaas. *Phys. Rev. B*, 11:767–770.

Subramaniam, S. and Mengüç, M. (1991). Solution of the inverse radiation problem for inhomogeneous and anisotropically scattering media using a Monte Carlo technique. *International journal of heat and mass transfer*, 34(1):253–266.

Sun, C., Li, H., and Chen, L. (2012). Nanostructured ceria-based materials: Synthesis, properties, and applications. *Energy & Environmental Science*, 5:8475–8505.

Sun, L.-L., Cheng, Y., and Ji, G.-F. (2010). Elastic and optical properties of ceo_2 via first-principles calculations. *Journal of Atomic and Molecular Sciences*, 1:143–151.

Tancrez, M. and Taine, J. (2004). Direct identification of absorption and scattering coefficients and phase function of a porous medium by a Monte Carlo technique. *International Journal of Heat and Mass Transfer*, 47(2):373–383.

Twomey, S. and Bohren, C. F. (1980). Simple approximations for calculations of absorption in clouds. *Journal of the Atmospheric Sciences*, 37(2):2086–2095.

Uzunoglu, N. K., Alexopoulos, N. G., and Fikioris, J. G. (1978). Scattering from thin and finite dielectric fibers. *Journal of the Optical Society of America*, 68(2):194–197.

van de Hulst, H. (1981). *Light Scattering by Small Particles*. Dover, New York, first edition.

Venstrom, L., Petkovich, N., Rudisill, S., Stein, A., and Davidson, J. (2012). The effects of morphology on the oxidation of ceria by water and carbon dioxide. *Journal of solar energy engineering*, 134(1).

Waterman, P. C. and Pedersen, J. C. (1998). Scattering by finite wires of arbitrary ϵ, μ, and σ. *Journal of the Optical Society of America A—Optics, Image, Science, and Vision*, 15(1):174–184.

Wu, L., Yang, H., Li, X., Yang, B., and Li, G. (2007). Scattering by large bubbles: Comparisons between geometrical-optics theory and debye series. *Journal of Quantitative Spectroscopy and Radiative Transfer*, 108(1):54 – 64.

Yang, P., Gao, B., Baum, B., Hu, Y., Wiscombe, W., S.Tsay, Winker, D., and Nasiri, S. (2001). Radiative properties of cirrus clouds in the infrared (813 m) spectral region. *Journal of Quantitative Spectroscopy and Radiative Transfer*, 70(46):473 – 504.

Yang, P. and Liou, K. (2009). An exact geometric-optics approach for computing the optical properties of large absorbing particles. *Journal of Quantitative Spectroscopy and Radiative Transfer*, 110(13):1162 – 1177.

Zhang, Z., Yang, P., Kattawar, G. W., Tsay, S., Baum, B. A., Hu, Y., Heymsfield, A. J., and Reichardt, J. (2004). Geometrical-optics solution to light scattering by droxtal ice crystals. *Appl. Opt.*, 43(12):2490–2499.

Appendix A

UV-VIS-NIR setup: component specification and calibration

A.1 Specifications of UV-VIS-NIR setup for bi-normal transmittance measurements

This section of the appendix deals with description and specifications of the components of the UV-VIS-NIR setup used for bi-normal transmittance measurements. Calibration data that shows the spectral accuracy of the setup as well as the linearity and dynamic range of measurements are listed in this appendix.

A.1.1 Xe arc lamp

A 300 W Newport ozone-free xenon arc lamp (model: 6258) was used as the source of radiation. This lamp has a nearly constant irradiance in the UV-VIS-NIR spectrum with a few sharp spectral excitation lines in the spectral range 0.8–1.1 μm. Spectral irradiance of the lamp at 0.5 m in units of mW m^{-2} nm $^{-1}$ is shown in Fig. A.1. This

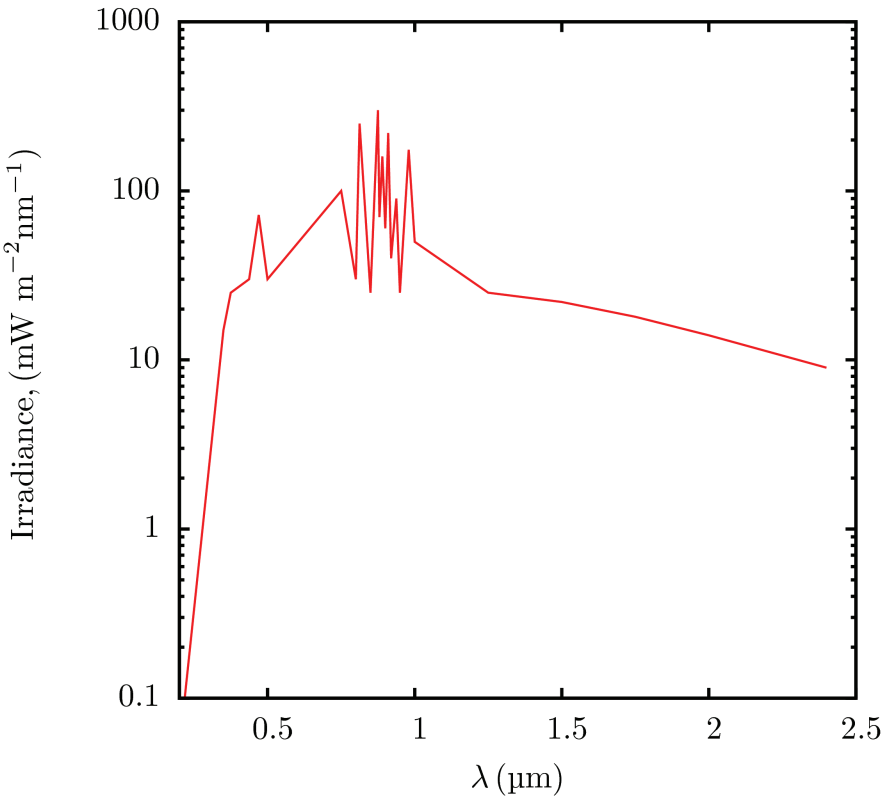

Figure A.1: Irradiance of xenon arc lamp at 0.5 m in the spectral range of 0.2–2.5 μm

lamp was chosen as the source of radiation in the bi-normal measurements because of its near-constant irradiance. The lamp has an approximate flux of 7000 lumens, and an arc size of 0.7 mm x 2.4 mm.

A.1.2 Monochromator

Two Newport MS 257 1/4 m monochromators are available for use in either subtractive double or single configuration to produce narrow bands of nearly mono-chromatic radiation. The monochromators consist of an input port of aperture diameter corresponding to F/Number 3.9. The input focal length of the monochromator is 220 mm and the exit

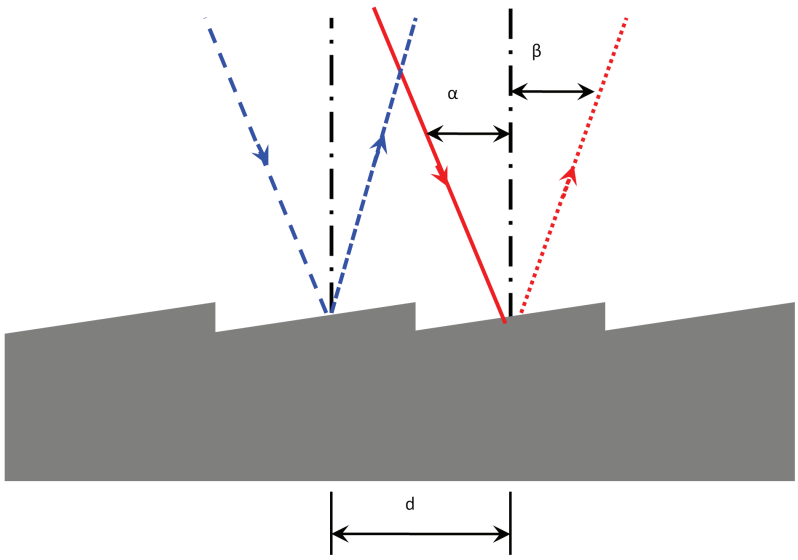

Figure A.2: Principle of diffraction gratings

focal length is 257.4 mm. The monochromators work on the principle of diffraction (see Fig. A.2). When a two parallel rays from a plane wavefront of light is incident on a narrow groove with a specified groove spacing, *d*, constructive interference occurs when the path difference between the two rays is equal to an integer, *m* of a wavelength λ:

$$m\lambda = d(\sin\alpha + \sin\beta) \tag{A.1}$$

For the case of $m = 0$, one can obtain the law of reflection, with $\alpha = -\beta$, i.e. angle of incidence equals angle of reflection. Thus, for a given wavelength, $|m\lambda|/d < 2$ corresponds to propagating diffracted wavefronts. When a polychromatic beam of light (composed of many wavelength) is incident on a diffraction grating, each wavelength that satisfies the grating equation is propagated.

Motorized slits control the spectral resolution of the monochromator. Spectral resolution characterizes the ability of a monochromator to resolve two wavelengths, λ_1 and $\lambda_2 = \lambda_1 + D$. The minimum wavelength difference D is referred to as limit of resolution or resolution between two wavelengths. Spectral resolution depends on the instrument's bandpass. Bandpass refers to the wavelength interval of light that passes through the exit slit of the monochromator. It is the difference in wavelengths between the points of half-maximum intensity on either side of an intensity maximum, for a given wavelength and slit width. Fig. A.3 illustrates the definition of bandpass of a spectroscopic instrument. The slit width of a spectroscopic instrument is the physical width of the slit. For the the MS 257, slit width can be adjusted between 4 μm (fully closed slits) to 2 mm (fully open slits) and incremented in steps of 2 μm. Band pass of an instrument can be calculated as:

$$b = ws_{\text{l}} \tag{A.2}$$

Here, w is the width of the slits in mm, and s_{l} refers to the reciprocal linear dispersion of the monochromator. Linear dispersion is a measure of separation between diffracted light of different wavelengths, and is in units of mm (of separation)/nm (wavelength). The measure of light intensity diffracted from a grating in a certain order is called its efficiency. The efficiency can be optimized by changing the form and depth of the grooves. The wavelength at which the efficiency of a grating is at its maximum is referred to as "blaze wavelength", λ_{blaze}.

Table A.1 is a summary of reciprocal dispersion, bandpass, line density (reciprocal of groove spacing of diffraction gratings, $1/d$) and blaze wavelength is listed for the four gratings used in the bi-normal transmittance measurements. Figure A.1.2 is a plot that shows the efficiency of the gratings used for bi-normal measurements.

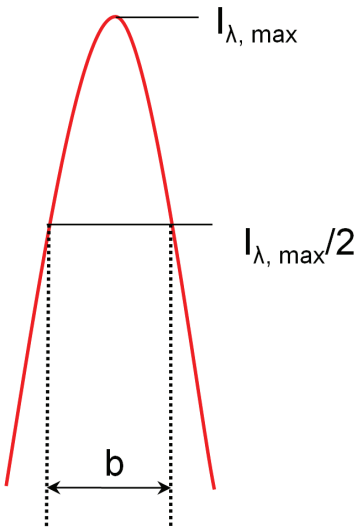

Figure A.3: Bandpass of a spectroscopic instrument for a given wavelength

A.1.3 Optical filters

Grating equation, eq. (A.1) shows the condition for which constructive interference, and consequently, propagation of waves occur. Setting $m = 1$, for a given wavelength, the propagated rays are known as first-order diffracted rays. Additionally, for $m = 2$, wavelengths that are half the wavelengths of the first-order diffraction will also satisfy the grating equation, and will be propagated with the first-order diffracted wavefront. For $m = 3$, known as third-order diffraction, $\lambda/3$ will also satisfy the grating equation where λ is the wavelength for first-order diffraction. Hence, a truly monochromatic band of radiation can be obtained only when the monochromators with gratings are accompanied by cut-on optical filters.

In order to eliminate higher-order diffraction peaks, the filter must have a cut-on

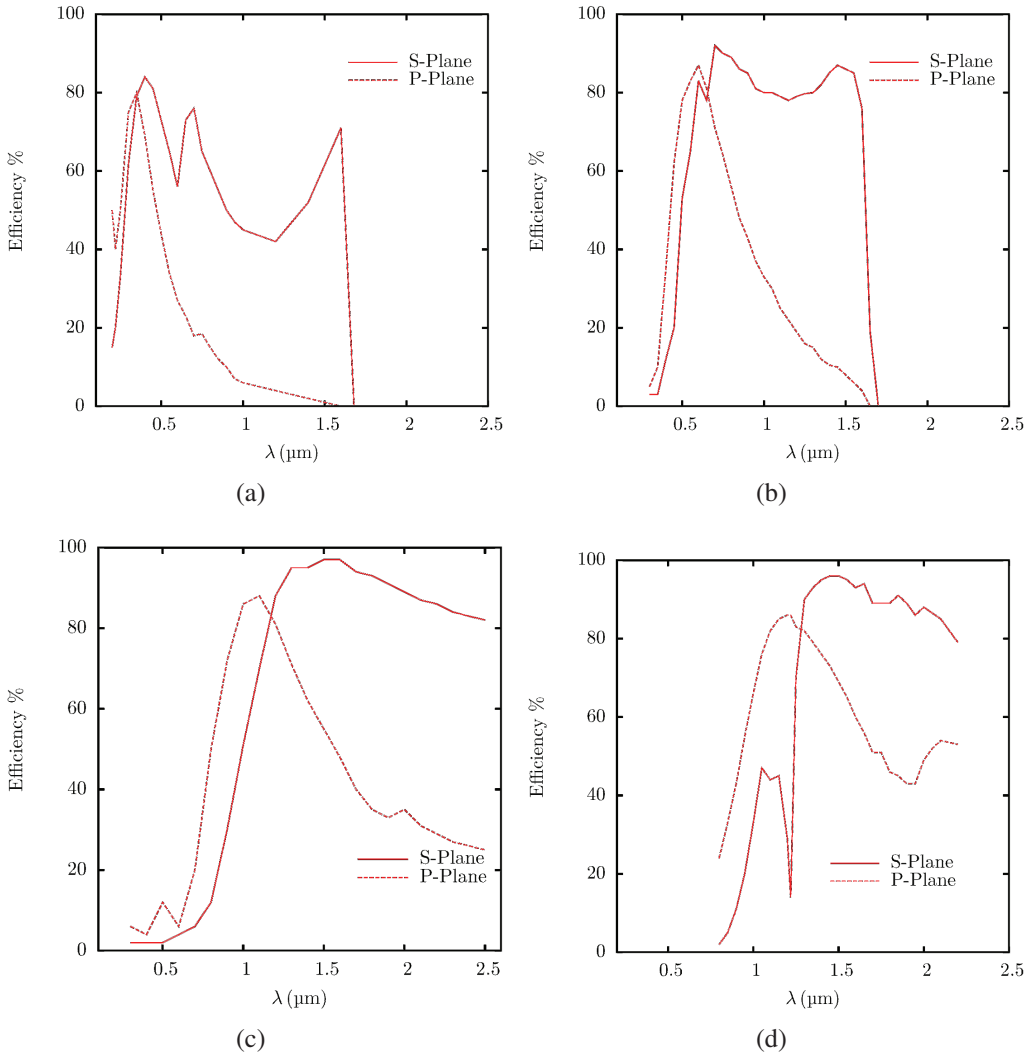

Figure A.4: Efficiency of gratings used in UV-VIS-NIR setup (a) G1 (b) G2 (c) G3 (d) G4. Data obtained from Newport Corporation.

Table A.1: Grating specifications

Position	Model	1/d (mm^{-1})	λ_{blaze} (μm)	Peak efficiency (%)	s (nm/mm)
G1	77742	1200	0.35	80	3.2
G2	77752	1200	0.75	80	3.1
G3	77767	600	1.25	85	6.4
G4	77768	600	1.6	90	6.2

wavelength, $\lambda_c > \lambda/2$, where λ is the wavelength of the first-order diffraction (desired wavelength). Note that a filter that eliminates second-order wavelength will also eliminate third and higher-order wavelength, because $\lambda/2 > \lambda/3$ and so on. Typically, filters do not have a sharply defined transmission spectra, so that wavelengths smaller than the cut-on wavelength are completely eliminated and wavelengths greater than or equal to the cut-on wavelength are completely transmitted. Thus, following condition is employed while selecting the filters:

$$\lambda_c > \lambda_{min} > \lambda/2 \tag{A.3}$$

Here, λ_c is the cut-on wavelength of the filter, λ_{min} is the wavelength of the filter corresponding to its minimum transmittance and λ is the wavelength of first-order diffraction. The filters transmit radiation with wavelengths above the cut-on wavelength, λ_c. Figure A.1.2 shows the the transmittance of filters used in the bi-normal transmittance setup. Table A.2 lists the cut-on wavelength and the wavelength range of optimal transmission for the filters.

Grating and filter combinations are chosen so that only first-order diffraction with maximum transmission efficiency is obtained. Table A.3 lists the filter and grating selection criteria for different parts of the spectrum. The filter and grating numbers correspond to the 'Position' column on tables A.2 and A.3.

Table A.2: Filter specifications

Position	Model	Cut-On Wavelength (μm)	Spectral range (μm)
F1	(no filter)	-	-
F2	51250	0.309	0.325–2.7
F3	51310	0.57	0.58–2.75
F4	51352	0.83	0.85–2.75

Table A.3: Filter and grating selection criteria

Spectral range (μm)	Filter	Grating
0.35–0.5	F2	G1
0.5–0.6	F2	G2
0.6–1.0	F3	G2
1.0–1.4	F4	G3
1.4–1.7	F4	G4

A.2 Calibration of the bi-normal transmittance setup

Two types of calibration are performed with the bi-normal transmittance setup to verify the spectral accuracy of measurements, and linearity and dynamic range. The objectives of the calibration procedure are to ensure that:

1) Measurement system is capable of producing narrow bands of nearly monochromatic radiation, with a spectral accuracy of at least 10 nm.

2) Detectors used in the measurement system respond linearly with radiative energy incident on the detectors.

3) Dynamic range of the measurement system is satisfactory. Transmittance measurements are conducted by placing an attenuating radiatively participating medium, and the setup must measure the radiative energy transmitted by the medium, which is

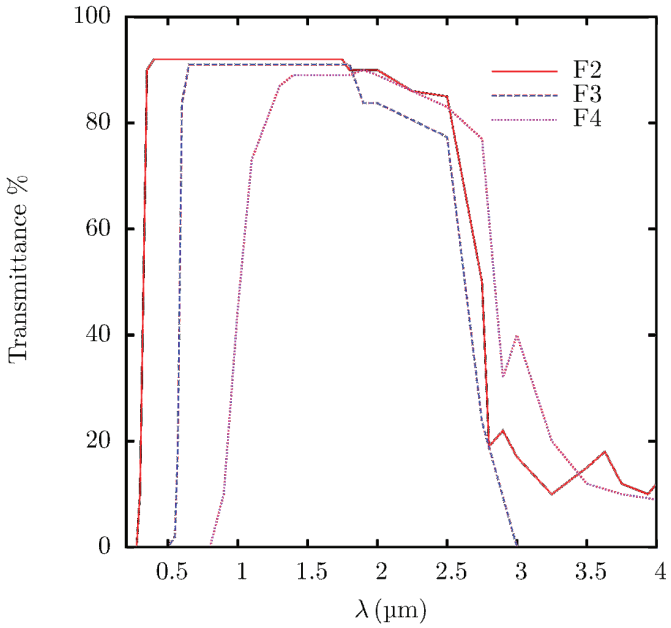

Figure A.5: Filter transmittance for optical filters used in the bi-normal transmittance setup. The filter numbers in the legend correspond to cut-on wavelengths and models listed in table A.2. Data obtained from Newport Corporation.

typically a few orders of magnitude lower than incident radiative energy.

Spectral accuracy of measurements is verified by calibrating the experimental setup with a pencil ray lamp containing a mixture of Hg-Ar. This lamp has sharp lines of excitation in the UV-VIS spectrum that has been reported in the literature (Reader et al., 1996). Table A.4 lists the spectral lines of the Hg-Ar pencil ray lamp measured by the bi-normal transmittance setup in subtractive-double and single configuration (see Figs. 3.1 and 3.2) and compares it to the spectral irradiance, G_λ measured at a distance of 250 mm from the lamp and reported in (Reader et al., 1996). Note that only the wavelengths at which peaks are present are compared between the present calibration and the data from Reader et al., and not the actual magnitudes of the peaks because of different quantities that are being measured (i.e, irradiance and radiative power) by Reader et al.

Table A.4: Spectrum of Hg-Ar lamp measured by Single and Subtractive-Double configuration compared to spectral irradiance (G_λ) data from Reader et al. (Reader et al., 1996).

$\lambda(\mu m)$	Double: $Q_d^0(\mu V)$	Single: $Q_d^0(\mu V)$	$\lambda(\mu m)$	G_λ ($\mu W/cm^2$)
0.25	17.8	523.3	0.2536521	74
0.26	12.7	115.6	0.2967283	0.651
0.31	3.2	25.39	0.3125674	0.714
0.37	3.51	11.08	0.3650158	1.35
-	-	-	0.404656	1.12
0.44	10.2	30.42	0.435833	2.55
0.55	0.163	122.9	0.546075	2.56
0.56	0.22	12.34	0.576910	0.28
0.58	0.149	34.45	0.579067	0.3

and in the present study.

Subtractive-double setup is typically known to resolve adjacent spectral lines better than the single setup. However, for the accuracy considerations of the present work, the single setup was found to be adequate as both setups had a spectral bandpass (defined by eq. A.2) of 6.4 nm in the spectral range 0.3–1.0 μm and 12 nm in the spectral range 1.0–1.7 μm. One of the features of the subtractive-double configuration is that rays undergo multiple reflection on focusing mirrors. While the single configuration also has focusing mirrors, rays in subtractive-double undergo twice the number of reflections as those in single configuration. As a result of this phenomenon, signal output from the double configuration is orders of magnitude weaker than the single configuration, especially in the spectral range of 1.0–1.7 μm. Thus, single configuration is chosen for all bi-normal transmittance measurements except those with the sintered ceria discs in the spectral range 0.3– 0.9 μm. No observable differences were found for that particular measurement set.

Linearity and dynamic range are verified by measuring the transmittance of metallic

neutral density filters with known optical densities. These filters are absorbing filters, i.e. they attenuate the incoming radiation by absorption. The transmitted fraction of the incident radiation is related to the optical density of a neutral density filter as:

$$OD = -\log_{10} T \tag{A.4}$$

Where T refers to its transmittance. Transmittance of neutral density filters are typically constant in the spectral range of responsiveness of the neutral density filter. Thus, by measuring transmittance of the neutral density filters using the bi-normal transmittance setup and comparing it to its known value of transmittance, the response of detectors and the dynamic range of the setup can be verified. This is because the neutral density filters are capable of three or four orders of attenuation of the incident radiation. Figure A.6 shows the transmittance of neutral density filters measured by the bi-normal transmittance setup.

Figure A.6 confirms that both detectors in the bi-normal transmittance setup respond linearly to changes in incident radiative energy. Transmittance of the neutral density filter measured by the bi-normal transmittance setup agree to within $\pm$ 5 % of their expected transmittance, calculated from eq. A.4.

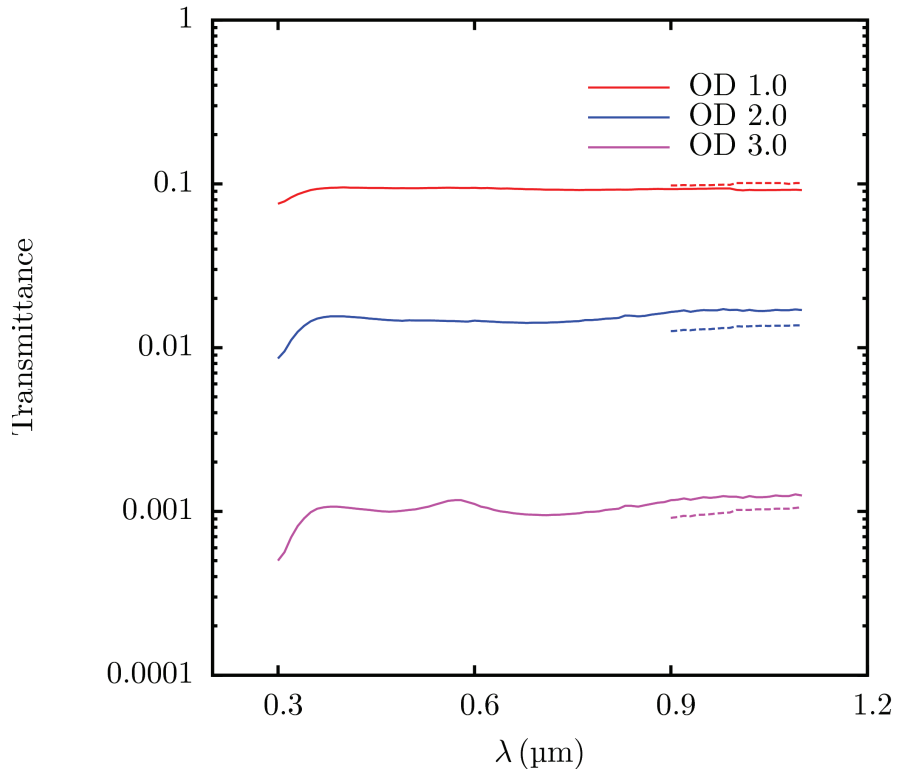

Figure A.6: Transmittance of metallic neutral density filters used in the bi-normal transmittance setup of optical density 1.0, 2.0 and 3.0. Solid curves indicate transmittance measured by silicon detector, and dashed curves indicate transmittance measured by germanium detector.

Appendix B

Approximate identification procedure from bi-normal transmittance

An approximate identification procedure was developed to infer radiative properties from measured bi-normal transmittance by Liang et al. (Liang et al., 2011), using two source functions proposed in (Lipiński et al., 2008). Consider a cylindrical sample with its two circular disc boundaries A_1 and A_2, respectively, filled with a two-phase medium consisting of a semi-transparent phase with the refractive index $n \neq 1$ and a transparent phase with the refractive index $n = 1$, respectively, surrounded by a non-participating medium with the refractive index $n = 1$. The irradiated boundary A_1 is exposed to an external intensity $I_{\text{in},}$. The boundary condition for RTE, eq. 2.1 at the boundary A_1 $\hat{\mathbf{s}} \cdot \hat{\mathbf{n}} > 0$ is:

$$I\left(\mathbf{r}_1, \hat{\mathbf{s}}\right) = \int\limits_{\Omega_\text{i}\,:\,\hat{\mathbf{s}}_\text{i}\cdot\hat{\mathbf{n}}>0} \tau''\left(\mathbf{r}_1, \hat{\mathbf{s}}_\text{i}, \hat{\mathbf{s}}\right) I_{\text{in},}\left(\mathbf{r}_1, \hat{\mathbf{s}}_\text{i}\right) \hat{\mathbf{s}}_\text{i} \cdot \hat{\mathbf{n}}\, \mathrm{d}\,\Omega_\text{i} - \int\limits_{\Omega_\text{i}\,:\,\hat{\mathbf{s}}_\text{i}\cdot\hat{\mathbf{n}}<0} \rho''\left(\mathbf{r}_1, \hat{\mathbf{s}}_\text{i}, \hat{\mathbf{s}}\right) I\left(\mathbf{r}_1, \hat{\mathbf{s}}_\text{i}\right) \hat{\mathbf{s}}_\text{i} \cdot \hat{\mathbf{n}}\, \mathrm{d}\,\Omega_\text{i} \tag{B.1}$$

where τ'' and ρ'' are the spectral bi-directional transmission and reflection functions of the interface between the two-phase medium and the surrounding medium, respectively; $\hat{\mathbf{n}}$ is the inner unit normal vector, i.e. $\hat{\mathbf{n}}$ points from the boundary into the two-phase medium. For a medium with high volume fraction of the phase with the refractive index $n \neq 1$, radiative interactions at the medium boundary cannot be neglected. The spectral radiative power of the external beam incident on the sample surface is:

$$\dot{Q}_{\text{in},} = \int_{A_1} \dot{q}_{\text{in},}\, \mathrm{d}\, A = \int_{A_1} \int_{\Omega=0}^{\Omega(\theta_1)} I_{\text{in},}\left(\mathbf{r}, \hat{\mathbf{s}}\right) \left|\hat{\mathbf{s}} \cdot \hat{\mathbf{n}}\right| \mathrm{d}\, \Omega\ \mathrm{d}\, A \tag{B.2}$$

where θ_1 is the divergence angle of the incident external radiation. Radiation leaving the sample at the boundary A_2 produces an intensity distribution $I_{\text{out},}\left(\mathbf{r}, \hat{\mathbf{s}}\right)$ outside the medium. The spectral radiative power acquired by a detector via collecting optics with the acceptance angle θ_2 and placed directly behind the boundary A_2 is given by:

$$\begin{aligned} \dot{Q}_{\mathrm{d}} &= C_{\text{coll}} \dot{Q}_{\text{out}} = C_{\text{coll}} \int_{A_2} \dot{q}_{\text{out}}\, \mathrm{d}\, A \\ &= C_{\text{coll}} \int_{A_2} \int_{\Omega=0}^{\Omega(\theta_2)} I_{\text{out}}\left(\mathbf{r}, \hat{\mathbf{s}}\right)\ \left|\hat{\mathbf{s}} \cdot \hat{\mathbf{n}}\right|\ \mathrm{d}\, \Omega\, \mathrm{d}\, A \end{aligned} \tag{B.3}$$

where $\dot{Q}_{\text{in}}$ is the spectral radiative power exiting the sample at A_2 and $C_{\text{coll}\lambda}$ is a constant taking into account losses in the collecting optics, $0 \leq C_{\text{coll}\lambda} \leq 1$. Here, the spectral overall transmittance of the sample is defined as:

$$T_{\text{d-d}} \overset{\text{def}}{=} \frac{\dot{Q}_{\text{out}}}{\dot{Q}_{\text{in}}} \tag{B.4}$$

$T_{\text{d-d}}$ is then approximated using the measured quantities:

$$T_{\text{d-d}} \approx \frac{\dot{Q}_{\mathrm{d}}}{\dot{Q}_{\mathrm{d}}^{0}} \tag{B.5}$$

where the radiative power $\dot{Q}_{\mathrm{d}}^{0}$ is measured in the same way as $\dot{Q}_{\mathrm{d}}$ but without any medium present between A_1 and A_2.

Formal solution to the RTE with the above boundary conditions would require the knowledge of medium properties, namely absorption and scattering coefficient, and the scattering phase function. The solution can be expressed as:

$$I\left(\mathbf{r}_2,\hat{\mathbf{s}}\right) = I\left(\mathbf{r}_1,\hat{\mathbf{s}}\right)\exp(-\beta|\mathbf{r}_2-\mathbf{r}_1|) + \int_{\mathbf{r}_1}^{\mathbf{r}_2} S\left(\mathbf{r},\hat{\mathbf{s}}\right)\exp(-\beta|\mathbf{r}_2-\mathbf{r}_1|)\beta\mathrm{d}\mathbf{r}^{*} \tag{B.6}$$

Equations (B.3)–(B.6) can now be combined, so that:

$$T_{\text{d-d}} = C_{\text{int}}\exp(-\beta L) + C_{\text{int}}\int_{0}^{L}\frac{S\left(s^{*},\hat{\mathbf{s}}\right)}{I\left(0,\hat{\mathbf{s}}\right)}\exp(-\beta\left(L-s^{*}\right))\beta\mathrm{d}s^{*} \tag{B.7}$$

Two approximate radiative source functions were proposed in (Lipiński et al., 2008):

$$\frac{S\left(s,\hat{\mathbf{s}}\right)}{I\left(0,\hat{\mathbf{s}}\right)} = \frac{B_2}{B_1}\exp(-B_3,s), \qquad B_1=\beta \tag{B.8a}$$

$$\frac{S\left(s,\hat{\mathbf{s}}\right)}{I\left(0,\hat{\mathbf{s}}\right)} = 0, \qquad B_4=\beta, \tag{B.8b}$$

enabling the spectral overall transmittance of disperse media to be represented as:

$$f = C_{\text{int}}\exp(-B_1L)\left(1-\frac{B_2}{B_1-B_3}\right) + C_{\text{int}}\frac{B_2}{B_1-B_3}\exp(-B_3L) \tag{B.9a}$$

$$g = C_{\text{int}}\exp(-B_4L) \tag{B.9b}$$

The function f will fit the overall transmittance when augmentation of intensity due to scattering occurs. Equation (B.9b), by contrast, can be recognized as Bouguer's law, and is valid when incoming scattering along a given direction does not contribute

to radiative intensity. The constant C_{int} is approximated based on geometry, optical properties and porosity as:

$$C_{\text{int}} \approx [\tau + (1-\tau)p]^2 \sin^2 \theta_2 \tag{B.10}$$

The constant C_{int} accounts for losses at the boundaries. It is an estimate made from the acceptance angle, θ_2, the porosity and the directional-hemispherical transmissivity τ. The directional-hemispherical transmissivity τ is obtained using Fresnel's equation for normally incident unpolarized radiation:

$$\tau \approx 1 - \frac{(n-1)^2 + k^2}{(n+1)^2 + k^2} \tag{B.11}$$

n and k are the real and imaginary parts of the complex refractive index of the medium.

By fitting the functions f and g to the measured overall transmittance, the extinction coefficient β can be estimated from the fit parameters B_1 or B_4. Fitting can be performed iteratively using the Levenberg-Marquard fitting algorithm. Original version of the source code was written by Liang (Liang et al., 2011) [1] .

Extinction coefficient, β can be estimated according to eqs. (B.9a) and (B.9b) from the fitting function. The fit coefficients B_2 and B_3 are indicative of attenuation due to scattering, as it can be seen that by setting $B_2 = 0$, the function f resembles function g (Bouguer's law applicable to non-scattering media). Results of fitting are available in the disc accompanying this thesis.

The source function eq.(B.8a) assumes that attenuation due to incoming scattering results in the incoming radiation being extinguished exponentially in the medium. One of the short-comings of this approximate analytical solution is that the source functions have no verifiable physical basis. Further, the number of fitting coefficients fitted to known value of transmittance suggests that the solution may not be a converged solution

[1] The fitting procedure assumes a guess value for the fit coefficients B_1 to B_4. The fitting functions f and g are computed and the procedure is repeated until the χ^2 objective function reaches a minimum.

to the inverse radiative transfer problem. However, it can be treated as a good initial guess-value for computationally expensive iterative solution techniques such as Monte Carlo ray-tracing method.

Appendix C

Monte Carlo ray-tracing routine

C.1 Sintered ceria discs

A flowchart of the MCRT simulations for sintered ceria discs is shown in Fig. C.1. A random number, R_ρ is generated. Interface reflectivity of ceria is determined according to eq. (6.6). If $R_\rho > \rho$, rays cross the boundary of the medium. Otherwise they are lost.

The position r_0 for rays within a circular aperture on the irradiated (left) boundary is given by:

$$\phi = 2\pi R_\phi \tag{C.1a}$$

$$r = r_1\sqrt{R_\mathrm{r}} \tag{C.1b}$$

$$\mathbf{r_0} = (r\cos\phi, r\sin\phi, 0) \tag{C.1c}$$

The direction of the ray is given by:

$$\phi = 2\pi R_\phi \tag{C.2a}$$

$$\theta = \sin^{-1}\left(\sqrt{R_\theta})\sin\alpha\right) \tag{C.2b}$$

$$\hat{\mathbf{s}} = \sin\theta\cos\phi\hat{\mathbf{t}}_\mathbf{1} + \sin\theta\sin\phi\hat{\mathbf{t}}_\mathbf{2} + \cos\theta\hat{\mathbf{n}} \tag{C.2c}$$

Here α in the cone angle of incidence in the bi-normal transmittance. For the simulations reported in this thesis, the cone angle of incidence is assumed to be zero. Attenuation path length s is determined by:

$$s = \frac{-1}{\beta} \ln(R_\beta) \tag{C.3}$$

The routine *int line cylinder* in the library *fsl* is called to compute the intersection point of the ray with the cylindrical computational domain. Note that the diameter and thickness of the sintered samples define the dimensions of the computational domain. *int line cylinder* returns intersection points ordered such that the nearest intersection point of the line with the cylinder is stored in the vector r_w *(2)*, where r_w is a 2×3 matrix. If the following condition is satisfied, the ray intersects with the cylinder at a point located within the medium. If the following condition is not satisfied, the ray intersects at a point that lies on the boundary of the medium.

$$s \leq |r_w(2) - r_0| \tag{C.4}$$

Another random number, R_ω is generated at this location. If $R_\omega \leq \omega_{\text{tr}}$, then the ray is scattered; otherwise it is absorbed. At the location of attenuation, if the ray is scattered, the position of the ray is updated as:

$$\mathbf{r_0} = \mathbf{r_0} + s\hat{\mathbf{s}} \tag{C.5}$$

At the location of attenuation, a new path length and direction are generated according to eqs. (C.3) and (6.8c). The routine *int line cylinder* is called again to determine new intersection points. If the ray is absorbed, ray history is terminated and a new ray is generated.

If a ray encounters a boundary, total internal reflection occurs if a random number $R_\rho \leq \rho$, the angle-averaged reflectivity of the interface. If total-internal reflection

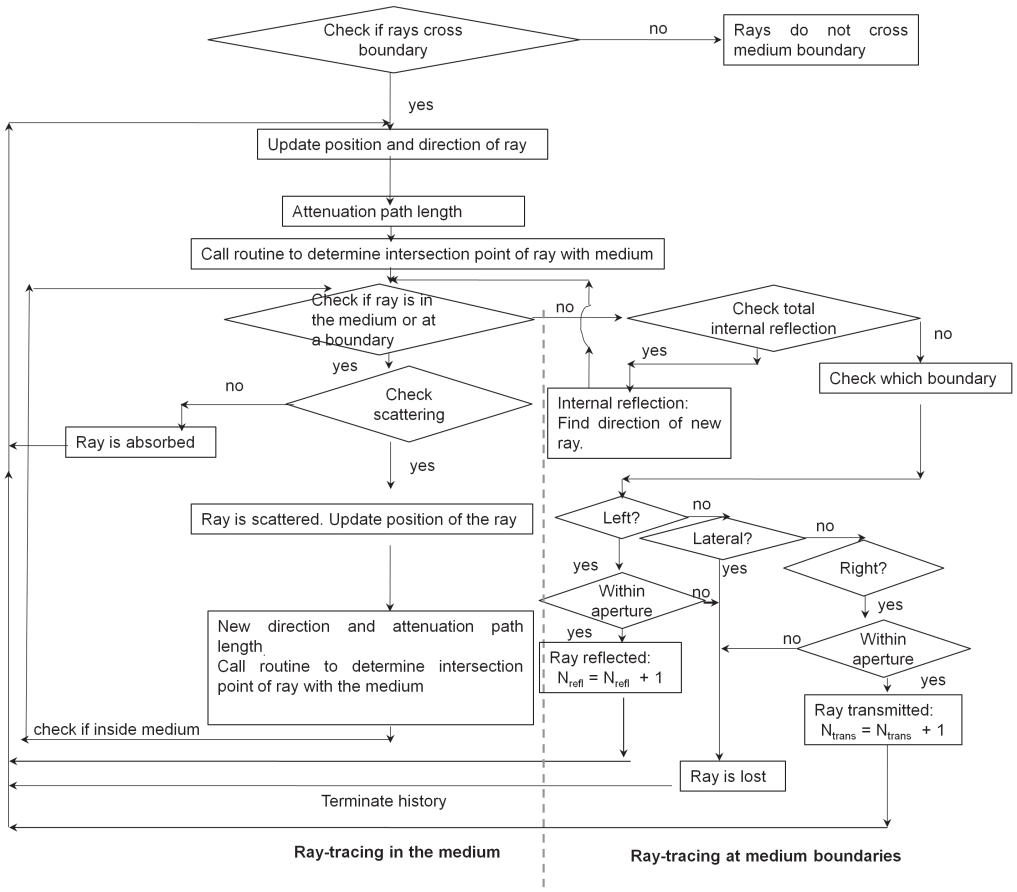

Figure C.1: Flowchart of Monte Carlo ray-tracing for the sintered ceria discs.

occurs, the direction of reflection is obtained by:

$$\phi = 2\pi R_\phi \tag{C.6a}$$

$$\theta = \sin^{-1}\left(\sqrt{R_\theta}\right) \tag{C.6b}$$

$$\hat{\mathbf{s}} = \sin\theta\cos\phi\hat{\mathbf{t}}_\mathbf{1} + \sin\theta\sin\phi\hat{\mathbf{t}}_\mathbf{2} + \cos\theta\hat{\mathbf{n}} \tag{C.6c}$$

Here, $\hat{\mathbf{t}}_\mathbf{1}$, $\hat{\mathbf{t}}_\mathbf{2}$ and $\hat{\mathbf{n}}$ form a right-handed system, such that $\hat{\mathbf{t}}_\mathbf{1}$ is parallel to the normal vector at the boundary. The normal vector is (0, 0, 1) for the irradiated boundary and (0, 0, -1) for the non-irradiated boundary. For the lateral boundary of the cylinder, the normal vector is given by:

$$\hat{\mathbf{n_3}} = \left(\frac{r_w(2,1)}{\sqrt{r_w(2,1)^2 + r_w(2,2)^2, r_w(2,3)^2}}, \frac{r_w(2,2)}{\sqrt{r_w(2,1)^2 + r_w(2,2)^2, r_w(2,3)^2}}, 0\right) \tag{C.7}$$

The attenuation path length at the location of total internal reflection is:

$$s = s - \sqrt{\Sigma(r_w(2) - r_0)^2} \tag{C.8}$$

The new position of the ray is simply the intersection point.

If the ray does not suffer total internal reflection, then the intersection surface is examined to determine whether the intersection point lies on the irradiated (left) boundary, non-irradiated (right) boundary, or on the lateral boundaries. If it lies on either the left or right boundaries and within an aperture corresponding to the diameter of the reflectance port of the integrating sphere (left boundary) or diameter of the iris diaphragm used in the bi-normal transmittance measurements (right boundary), it is treated as a reflected or a transmitted ray respectively. Otherwise the ray is treated as a lost ray. For the ray that is transmitted, a sub-routine that determines the frequency distribution of

rays in angular bins is called. The ray histories are terminated at this point, and a new ray is generated.

Bi-normal transmittance and normal-hemispherical reflectance is computed as:

$$T_{\text{MC}} = \frac{N_{\Omega}}{N_{\text{rays}}} \tag{C.9a}$$

$$R_{\text{MC}} = \frac{N_{\text{refl}}}{N_{\text{rays}}} \tag{C.9b}$$

where N_{Ω} refers to the number of rays transmitted that lie in the angular interval corresponding to the cone angle of the acceptance of the detector in the bi-normal transmittance setup, N_{refl} refers to the number of rays leaving the medium at the irradiated (left) boundary and N_{rays} refers to the number of rays launched. For the results reported in Chapter 6, the acceptance angle of the detector is estimated to be 6 °.

For the porous ceramics, interface reflectivity of ceria is set to zero, because of the high porosity of the medium. Iterations are manually repeated by adjusting β_{tr} and ω_{tr}, till a good match between the computed transmittance and reflectance and measured bi-normal transmittance and reflectance is obtained.

C.2 3DOM packed bed

Two major differences exist in the computational domain for the MCRT simulations of the sintered ceria ceramics and the 3DOM packed bed. For the 3DOM packed bed, the computational domain was a cuboid. The second difference was that the 3DOM ceria powder was sandwiched between two UV-fused silica windows. Figs. C.2 and C.3 are flowcharts that illustrate ray-tracing simulations for the packed bed and in the windows. The statistical relations for ray-tracing remain identical to that of the sintered ceria discs.

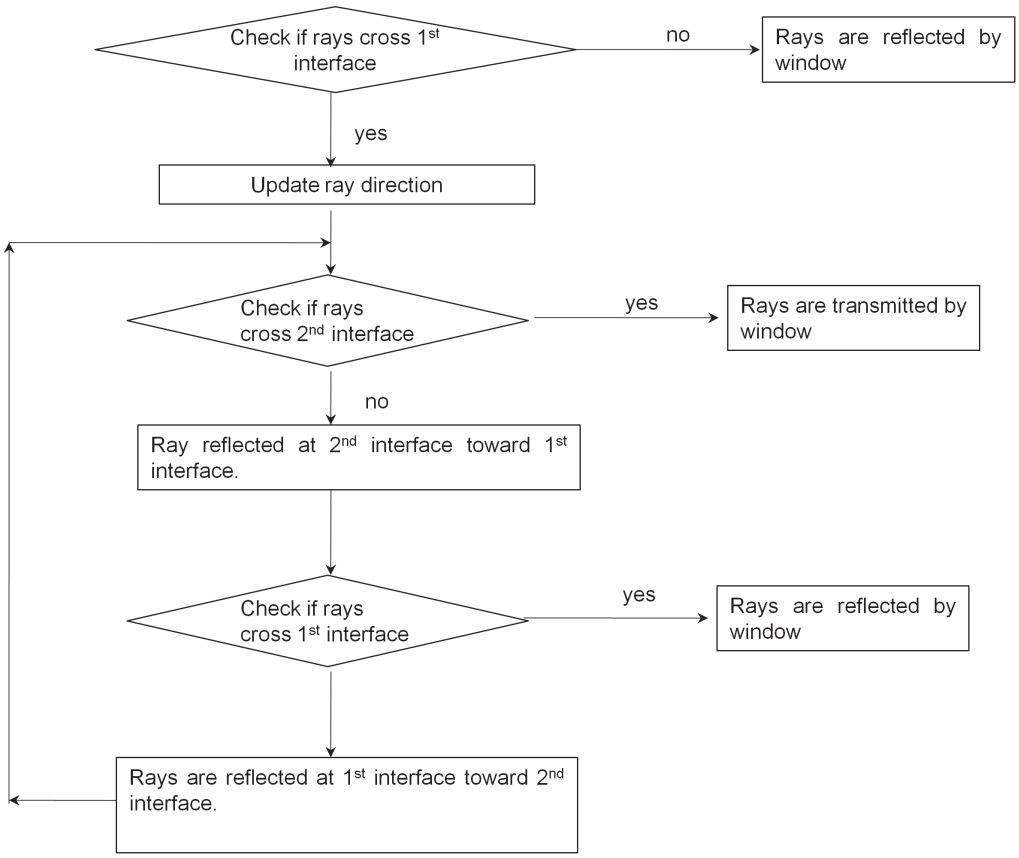

Figure C.2: Flowchart of Monte Carlo ray-tracing for the 3DOM packed bed.

Figure C.3: Flowchart of ray-tracing through a transparent window.

A random number, R_ρ is generated. Interface reflectivity of the window is determined according Fresnel equations using the routine *fresnel* in the library *tsl*. $R_\rho > \rho_{\text{window}}$, rays cross the window and are counted as rays reflected by the window. Once the rays enter the window, another random number is generated to check if rays cross the second interface. If rays cross the second interface of the window, they are treated as rays transmitted by the window. Otherwise, the rays are reflected back towards the first window. Ray-tracing is repeated till rays leave the window via either interface. Absorption in the window is assumed to be non-negligible. The window subroutine was validated by using theoretical expressions for transmittance through a slab with multiple reflections (Modest, 2003).

Appendix D

Uncertainty analysis for transmittance and reflectance measurements

Statistical uncertainty in any measured quantity, U can be expressed as:

$$\Delta U = \frac{t_{\alpha,\nu}\sigma_{N-1}}{\sqrt{N}} \tag{D.1}$$

Here, ΔU is the uncertainty in measurement of any variable U, $t_{\alpha,\nu}$ is the two-tailed Student's t-distribution, σ_{n-1} is the standard deviation in variable U over N samples (i.e. number of experimental trials). Uncertainty in transmittance and reflectance measurements were estimated at 95 % confidence intervals.

For the experimental results reported in Chapter 5, statistical uncertainty is quantified as a percentage of the arithmetic-mean value $\bar{U}$ of the measured quantity U:

$$\Delta U\% = \frac{\Delta U}{\bar{U}} \times 100 \tag{D.2}$$

Figure D.1 and D.2 show the percentage statistical uncertainty in bi-normal transmittance of the dense and porous sintered ceria ceramics respectively at different wavelengths. Experimental uncertainty is high up to a wavelength of 0.5 μm. This is because at these wavelengths, the signal reaching the detector from the ceria ceramics is

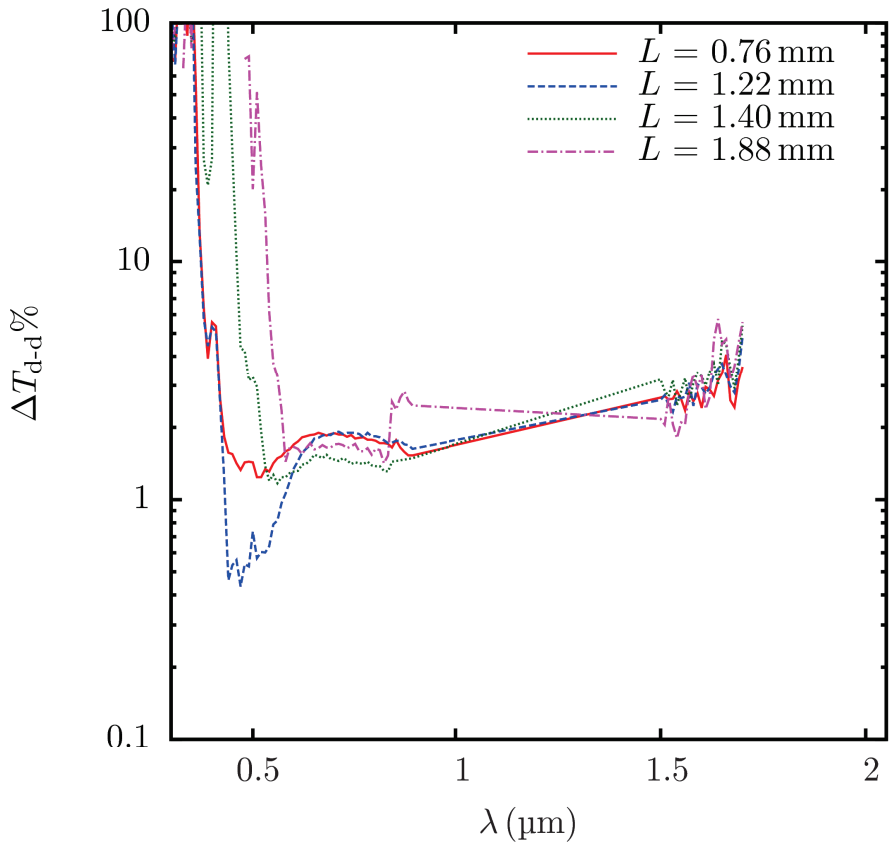

Figure D.1: Percentage statistical uncertainty in bi-normal transmittance measurement of the sintered dense ceramics.

extremely low due to strong absorption in the medium. After 0.5 µm, in the spectral range of semi-transparency, statistical uncertainty in bi-normal transmittance is of the order 5 % for all samples. Figure D.3 shows the statistical uncertainty in bi-normal transmittance of the 3DOM packed bed. The statistical uncertainty is comparable to that of the sintered ceria ceramics, and is high for the sample of thickness 1.19 mm.

Statistical uncertainty in normal-hemispherical measurements for the 3DOM packed bed is shown in Figs. D.4 and D.5 respectively. Due to low directional-hemispherical

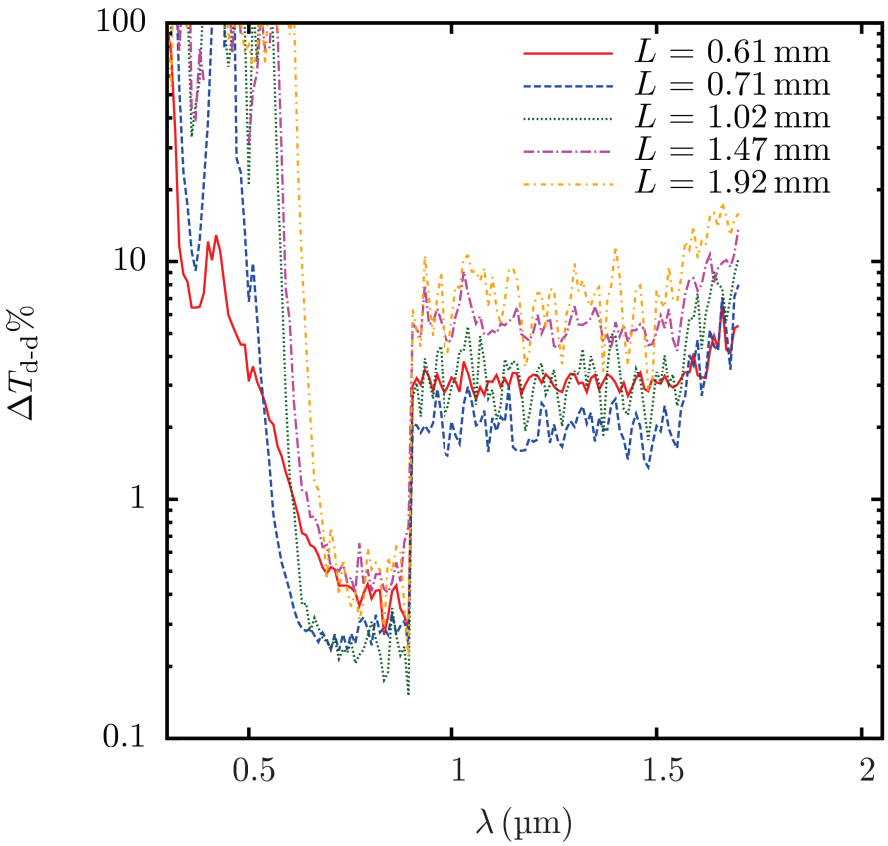

Figure D.2: Percentage statistical uncertainty in bi-normal transmittance measurement of the sintered porous ceramics.

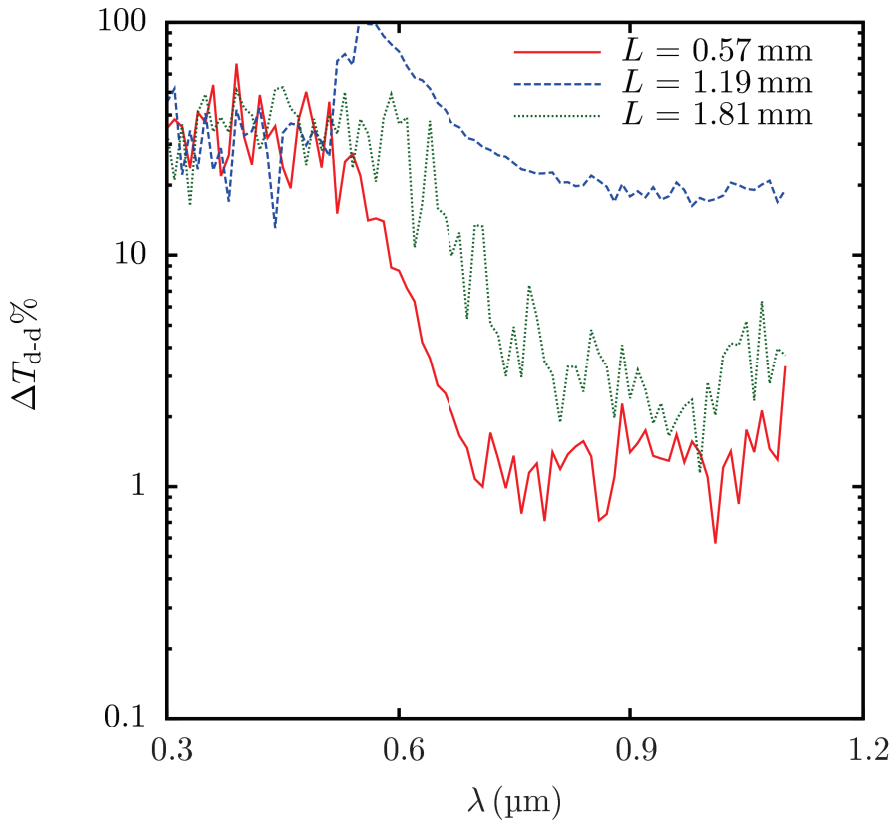

Figure D.3: Percentage statistical uncertainty in bi-normal transmittance measurement of the 3DOM packed bed.

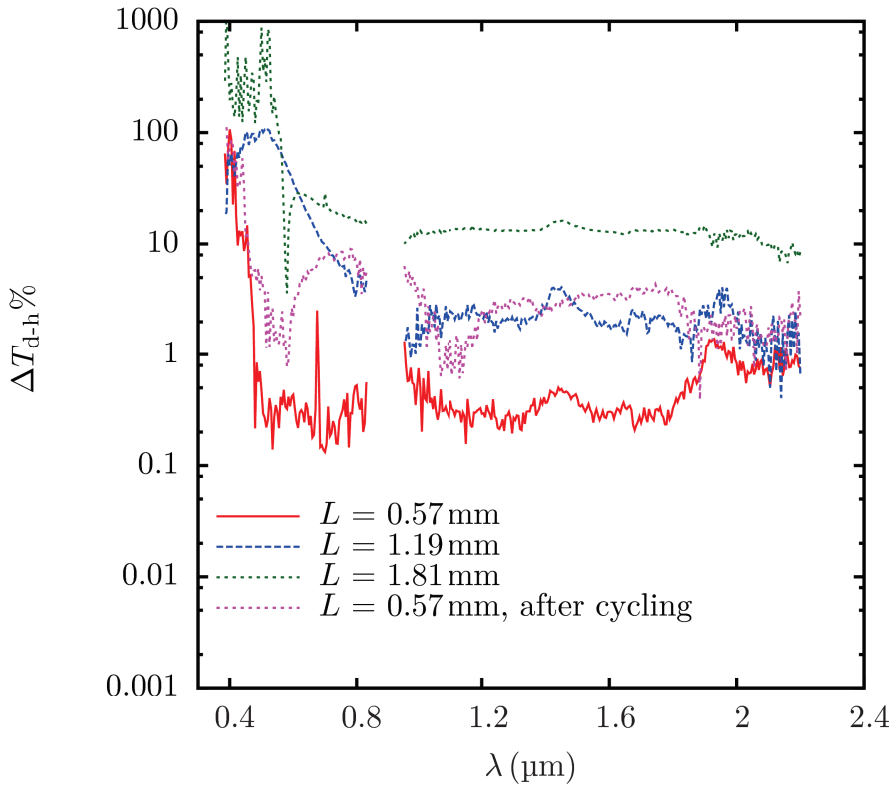

Figure D.4: Percentage statistical uncertainty in normal-hemispherical transmittance measurement of the 3DOM ceria packed bed.

transmittance in the spectral range of strong absorption, the uncertainty in directional-hemispherical transmittance is high up to a wavelength of 0.6 µm. After this wavelength, statistical uncertainty directional-hemispherical transmittance is 5 % for samples of thickness 0.57 mm and 1.19 mm, and approximately 10 % for the thickest sample (of thickness 1.81 mm) due to its high optical thickness. Statistical uncertainty in directional-hemispherical reflectance is of approximately 1 % in the entire spectral range of measurements.

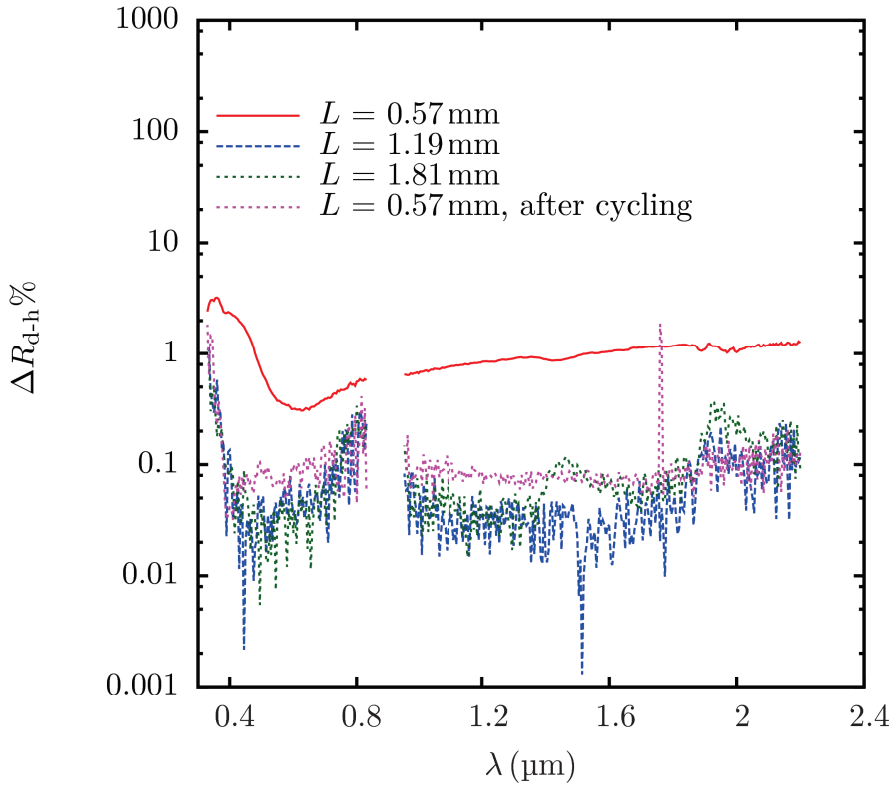

Figure D.5: Percentage statistical uncertainty in normal-hemispherical transmittance measurement of the 3DOM ceria packed bed.